UNIVERSITY OF KWAZULU-NATAL

# GRAVITATIONAL LENSING OF THE COSMIC MICROWAVE BACKGROUND: TECHNIQUES AND APPLICATIONS

by

HEATHER PRINCE

Submitted in fulfillment of the academic requirements
for the degree of Master of Science,
in the School of Mathematics, Statistics and Computer Science,
University of KwaZulu-Natal

Durban
February 2016

As the candidate's supervisor I have approved this thesis for submission.

Signed: _____ Name: _____ Date: _____

*For my father, Colin Prince,*

*who unconditionally supports me in everything I do,*

*and who has inspired my love of science.*

# Abstract

We have entered an era of precision cosmology, in which the parameters of the standard cosmological model have been well constrained by observations. The cosmic microwave background (CMB) has played a vital role in providing these constraints, because the primordial CMB is sensitive to many of the cosmological parameters. The observed CMB is modified by secondary effects caused by photon interactions after the surface of last scattering. One such effect is gravitational lensing, the deflection of photons due to the matter that they pass. Gravitational lensing can be used to probe the total matter distribution, which is dominated by dark matter. CMB lensing also provides complementary cosmological information to that obtained from the CMB power spectrum, and can be used to break parameter degeneracies and improve constraints on dark energy and neutrino masses.

We explore methods of reconstructing the lensing field from lensed CMB temperature and polarisation maps in real space, as an alternative to the harmonic space estimators currently in use, by extending an existing temperature real space estimator to CMB polarisation. Real space estimators have the advantage of being local in nature and they are thus equipped to deal with the nonuniform sky coverage, galactic cuts and point source excisions found in experimental data. We characterise some of the properties and limitations of these estimators and test them on simulated maps, finding that the reconstructions are accurate for large-scale lensing fields, and

that the polarisation reconstructions improve on those from CMB temperature maps.

Neutral hydrogen (HI) intensity mapping is expected to be a powerful probe of large scale structure and cosmology, and a number of current and planned experiments will be performing large intensity mapping surveys. HI is a biased tracer of the dark matter distribution, therefore HI observations will be correlated with CMB lensing reconstructions. We investigate the potential for measuring this cross-correlation using CMB lensing reconstructed from Advanced ACTPol observations and HI intensity mapping data from the Hydrogen Intensity and Real-time Analysis eXperiment (HIRAX). We find that the CMB lensing-HI cross-correlation will be detectable with a total signal to noise ratio of between 20 and 50 in each of four bins in the HIRAX frequency range, which will allow us to constrain the HI bias on various scales over a wide redshift range ($z$ = 0.8 to 2.5).

# Acknowledgments

Firstly, I am grateful to my supervisor, Prof Kavilan Moodley, for his wisdom, guidance and patience over the past few years, for encouraging me to achieve things I didn't think were possible, and for affording me the opportunity to travel to various conferences, workshops and research visits. It has been a privilege to learn from such an outstanding mentor.

I would like to thank Prof Martin Bucher for his insightful ideas, and for the many discussions we had in which I had difficulty keeping up, but learnt a great deal. I am grateful to Dr Aurélie Pénin for her constant willingness to explain a concept or pass on some of her coding experience.

I wish to thank all the members of the Astrophysics and Cosmology Research Unit at UKZN from whose encouragement and insights I have benefited, especially Prof Jon Sievers and Dr Cynthia Chiang who kept me on my toes with all the order-of-magnitude problems. I am also very grateful to Prof David Spergel for his sound advice, and to the Princeton Department of Astrophysical Sciences for hosting me for a research visit.

I am indebted to the Square Kilometer Array South Africa, who provided me with funding for the duration of my degree and created a wonderful environment of discussion and collaboration at their annual bursary conferences.

I had the pleasure of learning undergraduate physics from passionate and brilliant lecturers, and I am very grateful to Dr Jennifer Williams, Dr Ray Haggard and Dr David Roux for

encouraging my interest in physics and academia.

I would also like to thank my mother for patiently answering my interminable questions as a child and for her encouragement in my studies, and my father for helping me with fun experiments when I was younger, always encouraging scientific enquiry, and supporting me both financially and emotionally in my studies. I am thankful for my sisters, for continuing to ask about my research in spite of my esoteric replies and for fun thesis-writing breaks that kept me going.

Last but certainly not least, I am grateful to my husband, Andy Kruger, for his constant support, encouragement and unwavering belief in me, and for bringing balance and perspective to my life.

# Preface

The work described in this dissertation was carried out in the School of Mathematics, Statistics and Computer Science at the University of KwaZulu-Natal from January 2014 to December 2015. This dissertation was completed under the supervision of Prof Kavilan Moodley.

This study represents original work by the author and has not been submitted in any form for any degree or diploma to any other tertiary institution. Where use was made of the work of others it has been duly acknowledged in the text.

# Declaration of Non-Plagiarism

I, **Heather Prince** declare that

1. The research reported in this thesis, except where otherwise indicated, is my original research.
2. This thesis has not been submitted for any degree or examination at any other university.
3. This thesis does not contain other persons' data, pictures, graphs or other information, unless specifically acknowledged as being sourced from other persons.
4. This thesis does not contain other persons' writing, unless specifically acknowledged as being sourced from other researchers. Where other written sources have been quoted, then:
   (a) Their words have been re-written but the general information attributed to them has been referenced.
   (b) Where their exact words have been used, then their writing has been placed in italics and inside quotation marks, and referenced.
5. This thesis does not contain text, graphics or tables copied and pasted from the Internet, unless specifically acknowledged, and the source being detailed in the thesis and in the References sections.

Signed in Westville, KwaZulu-Natal: _____ Date: _____

# Declaration

Two publications based on the results presented in this thesis are in preparation.

**Chapter 3**

Prince, H., Moodley, K., Ridl, J., Bucher, M. *Real space lensing reconstruction using cosmic microwave background polarisation*, in preparation, 2016.

I derived the polarisation estimators presented in this chapter under the supervision of Prof K Moodley and based on the temperature estimators presented in Bucher et al. (2012). I derived the expression for the multiplicative bias and developed the code to obtain the results in that section. I modified the lensing simulation and reconstruction code developed by M Bucher, J Ridl and K Moodley.

**Chapter 4**

Prince, H., Pénin, A., Moodley, K. *Cross-correlation of CMB lensing with post-reionisation HI intensity mapping surveys*, in preparation, 2016.

I derived the expressions for the cross-correlation signal and noise in consultation with Prof K Moodley and Dr A Pénin. I developed the code to obtain the noise results. A Pénin developed the code to obtain the multi-frequency angular power spectrum results in this chapter, and I modified this code to obtained the binned spectra.

# Contents

**Abstract** **i**

**Acknowledgments** **iii**

**Preface** **v**

**Declaration of Non Plagiarism** **vi**

**Declaration** **vii**

**1 Introduction** **1**

**2 Cosmological Background** **9**

2.1 Standard Cosmological Model . . . . . 9

2.1.1 Cosmological Principle . . . . . 9

2.1.2 General Relativity . . . . . 10

2.1.3 Equation of State and Density Parameters . . . . . 12

2.1.4 Evolution of the Scale Factor and Hubble Parameter . . . . . 14

2.1.5 Redshift . . . . . 15

2.1.6 Distances . . . 15
2.2 Perturbation Theory and Large-Scale Structure Formation . . . 18
2.2.1 Perturbed Einstein Equations . . . 18
2.2.2 Gauge Transformations . . . 21
2.2.3 Equations Governing the Evolution of Perturbations . . . 23
2.2.4 Evolution of the Power Spectrum . . . 26
2.3 Inflation . . . 29
2.4 The Cosmic Microwave Background . . . 31
2.4.1 Statistics of CMB Temperature Anisotropies . . . 31
2.4.2 Physics of CMB Temperature Anisotropies . . . 32
2.4.3 CMB Polarisation . . . 34
2.5 Weak Gravitational Lensing of the Cosmic Microwave Background . . . 35
2.5.1 Deflection Angle . . . 36
2.5.2 Lensing Potential . . . 37
2.5.3 Magnification Matrix . . . 39
2.5.4 Lensed CMB Power Spectra . . . 41

**3 Real Space Estimators for CMB Lensing Reconstruction 44**
3.1 Temperature and Polarisation Estimators . . . 45
3.1.1 Derivation from Lensed Power Spectra . . . 46
3.1.2 Real Space Estimators as a limit of Harmonic Space Estimators . . . 53
3.1.3 Derivation from Lensed Correlation Functions . . . 56
3.2 Features of Real Space Estimators . . . 62
3.2.1 Cumulative Information . . . 62
3.2.2 Reconstruction Kernels . . . 64
3.2.3 Multiplicative Bias . . . 67
3.3 Simulated CMB Lensing Map Reconstructions . . . 70
3.3.1 Lensing Reconstruction Applications . . . 77

**4 Cross-Correlation of CMB Lensing with HI Intensity Mapping** **80**

4.1 Neutral Hydrogen . . . 81

4.1.1 HI Lines . . . 82

4.1.2 Intensity Mapping . . . 83

4.1.3 HI Intensity Mapping Signal . . . 83

4.1.4 HI Power Spectrum . . . 86

4.1.5 Thermal Noise from HI Intensity Mapping . . . 89

4.1.6 Foregrounds . . . 92

4.1.7 HI Signal to Noise . . . 94

4.2 CMB Lensing Convergence . . . 96

4.2.1 Lensing Signal . . . 96

4.2.2 Lensing Reconstruction Noise . . . 97

4.3 Cross-Correlation of CMB Lensing with HI Intensity Mapping . . . 99

4.3.1 Cross-Correlation Angular Power Spectrum . . . 100

4.3.2 Cross-Correlation Noise . . . 101

4.3.3 Cross-Correlation Signal to Noise . . . 105

4.3.4 Constraints from the Lensing-HI Cross-Correlation . . . 106

**5 Conclusion** **107**

**6 Bibliography** **110**

# CHAPTER 1

# Introduction

*In the beginning there was nothing, which exploded.*

– Terry Pratchett

Time began 13.8 billion years ago with the Big Bang, when the universe started to expand from an initial singularity (Planck Collaboration et al., 2015c). A period of rapid inflation followed, during which the universe expanded by approximately 60 e-foldings, increasing in size by a factor of $10^{26}$ in a very short time period (Guth, 1981; Guth and Weinberg, 1983). Inflation stretched the initial quantum fluctuations into small inhomogeneities in the matter density, which seeded the large-scale structure we see today (Padmanabhan, 1993; Peebles and Yu, 1970). After inflation, expansion continued at a much slower rate. The universe cooled with its expansion, allowing subatomic particles to form protons and neutrons, and later allowing light nuclei to form in a process known as Big Bang nucleosynthesis (Alpher et al., 1948; Gamow, 1948). The hot temperatures at early times meant that high-energy photons would immediately ionise any neutral atoms as they formed. The photons, electrons and protons were tightly coupled into a photon-baryon fluid by Compton scattering of photons off electrons and Coulomb interactions

between electrons and protons. Photons could only travel very short distances before scattering off an electron: the universe was opaque.

Around 380 000 years after the Big Bang, the universe had cooled sufficiently to usher in a period of recombination: electrons and protons combined to form neutral hydrogen (Peebles, 1968; Zeldovich et al., 1968). This reduction in free electrons resulted in photons decoupling from matter and traveling freely with few interactions. These photons pervade the universe, and are known as the cosmic microwave background (CMB), because their energies fall in the microwave part of the electromagnetic spectrum when they reach us. The CMB cooled as the universe expanded, and its temperature dropped from $T = 3000$K at recombination to $T = 2.725$K today (Mather et al., 1992). The fluctuations in the early universe reveal themselves as anisotropies in the CMB, or slightly hotter and colder regions with $\delta T/T \approx 10^{-5}$ (Smoot et al., 1992). The CMB is also partially linearly polarised due to Thomson scattering in the presence of a quadrupole anisotropy at the last scattering surface (Hu and White, 1997). The CMB provides a snapshot of the universe relatively soon after the Big Bang, giving us valuable insight into the early universe and allowing us to constrain the cosmological parameters (Planck Collaboration et al., 2015c).

The fluctuations that are seen in the CMB are caused by perturbations to the otherwise uniform matter distribution in the universe at early times: there were regions that were slightly more dense than the average as well as regions that were slightly less dense. Overdense regions attracted more matter, and so the slight primordial overdensities gradually grew, under the influence of gravity, into the large-scale structures we see today (Peebles and Yu, 1970; Peebles, 1982).

The first stars formed a few hundred million years after the Big Bang, putting an end to the dark ages and heralding the cosmic dawn (McKee and Ostriker, 2007; Zinnecker and Yorke, 2007; Bromm and Larson, 2004). These stars lit up the sky with UV radiation, which began a period of reionisation, during which most of the neutral hydrogen (HI) was converted to ionised hydrogen (HII) (Barkana and Loeb, 2001). After reionisation, the fraction of hydrogen that remains in neutral form is found only in dense regions of galaxies and the intergalactic medium (Wyithe and Loeb, 2008; Bagla et al., 2010).

Early astronomers expected the universe to be made up of ordinary baryonic matter and radiation. However, the velocity dispersion of galaxies in the Coma cluster indicated that far more mass was present than could be accounted for by stars, gas and dust (Zwicky, 1933, 1937), leading to the conclusion that most of the mass in the universe must come from another type of matter. Other observations support this conclusion, including the observed shapes of galaxies (Ostriker and Peebles, 1973), rotation curves of galaxies (Rubin and Ford, 1970), gravitational lensing measurements (Clowe et al., 2006), and constraints on the total and baryonic matter density from the CMB (Spergel et al., 2003). This mysterious component of the universe seems to only interact gravitationally, and does not emit or absorb radiation, leading to the term 'dark matter'. Recent constraints from CMB observations suggest that dark matter makes up 25.8% of the mass-energy content of the universe, while baryonic matter makes up only 4.8% (Planck Collaboration et al., 2015c). Most of the mass in the universe is therefore in the form of dark matter.

Another unexpected turn in the course of cosmology was the discovery that the universe is undergoing accelerated expansion. Hubble (1929) was the first to observe that the universe was expanding, but it was believed that the expansion was slowing, and the universe might eventually begin to collapse back in on itself. Observations of Type Ia supernovae showed that the expansion of the universe was in fact accelerating, suggesting the presence of dark energy to fuel this accelerated expansion (Riess et al., 1998; Perlmutter et al., 1999). One candidate for dark energy is a cosmological constant, a vacuum energy whose energy density remains constant as the universe expands, often visualised as a sort of 'negative pressure'. Dark energy constitutes 69.4% of the universe's energy content at present (Planck Collaboration et al., 2015c).

We therefore appear to live in a universe dominated by the largely unexplained quantities of dark matter and dark energy. It seems our universe can nevertheless be well characterised by only six cosmological parameters which describe the contents and history of the universe. These are the parameters of the standard $\Lambda$CDM model of the universe, where $\Lambda$ is the symbol traditionally used for the cosmological constant and CDM stands for cold dark matter. The majority of observations are consistent with the $\Lambda$CDM model, although various modifications to the standard model have been proposed. For the rest of this thesis we assume that the $\Lambda$CDM

model accurately describes our universe.

The CMB is not just a picture of the universe at early times: CMB photons interact with the large-scale structure in various ways after recombination and last scattering, resulting in secondary effects that modify the primordial CMB. Compton scattering of CMB photons off high-energy electrons results in the thermal Sunyaev-Zel'dovich effect which boosts low energy photons to higher energies (Sunyaev and Zeldovich, 1972). CMB photons that scatter off electrons in galaxy clusters that are moving with respect to the CMB rest frame experience a Doppler shift known as the kinetic Sunyaev-Zel'dovich effect (Sunyaev and Zeldovich, 1975; Amblard et al., 2004). Photons scatter off the free electrons produced during reionisation, suppressing the power in CMB temperature and inducing polarisation on large angular scales (Haiman and Knox, 1999). The Rees-Sciama effect, a late time integrated Sachs Wolfe effect, changes the energy of photons that pass through potential wells that evolve during the photon's passage (Rees and Sciama, 1968). One of the most significant secondary effects, and the one we focus on, is gravitational lensing: the deflection of CMB photons due to the matter that they pass (Blanchard and Schneider, 1987; Cole and Efstathiou, 1989; Linder, 1990)

Gravitational lensing is predicted by Einstein's theory of general relativity (Einstein, 1915). Earlier scientists had speculated about gravitational lensing and used Newtonian theory to calculate the amplitude of the deflection, finding a deflection half as large as the correct amplitude predicted by general relativity and confirmed by observations (Dyson et al., 1920). Lensing causes CMB photons to be deflected as they pass massive structures while traveling to us from the surface of last scattering (Seljak, 1996). Thus the primordial CMB is remapped by a deflection field, with photon positions on the sky shifting slightly from the primordial to the lensed CMB. The lensing effect contains information about the matter between us and the last scattering surface, so the lensed CMB can be used to recover the projected distribution of matter in the universe (e.g. Hu, 2001a,b; Zaldarriaga and Seljak, 1999). Gravitational lensing therefore provides a method for studying dark matter, which only interacts gravitationally.

When the CMB is lensed, the structure of the unlensed CMB (caused by the acoustic oscillations of the photon-baryon fluid before decoupling) is slightly smoothed out. Lensing also produces a non-Gaussian signal in the lensed CMB (Zaldarriaga, 2000; Hu, 2001a,b). Gravita-

tional lensing of the CMB due to large scale structure results in correlations between different harmonic modes which are uncorrelated in the unlensed CMB. These off diagonal correlations are proportional to the lensing potential, or the gravitational potential projected along the line of sight. We can therefore construct estimators based on these correlations that allow us to reconstruct the lensing potential (Zaldarriaga and Seljak, 1999; Hu and Okamoto, 2002).

Performing the lensing reconstruction in harmonic space poses difficulties for experimental data, which only covers part of the sky and contains point source excisions and nonuniform weightings. A local estimator implemented in map space can be helpful because it circumvents the need to transform into harmonic space, which is an inherently nonlocal procedure. Bucher et al. (2012) developed a real space estimator that can be applied to CMB temperature maps to locally reconstruct the lensing field. Many experiments are now mapping the CMB sky in polarisation as well as temperature, such as ACTPol (Naess et al., 2014) and SPTpol (Crites et al., 2015), as well as the now-completed Planck mission (Planck Collaboration et al., 2015f). As the sensitivity and resolution of CMB experiments continues to improve, the highest signal-to-noise lensing reconstructions will come from polarisation data (Hu and Okamoto, 2002), so in this thesis we extend the real space temperature lensing estimator to CMB polarisation.

Gravitational lensing can be used to constrain cosmological parameters. Apart from the obvious applications to constraining the matter density and the amplitude of the matter power spectrum, lensing can prove useful in breaking degeneracies between parameters that affect the CMB power spectrum in the same way. For example, having access to the lensing potential allows us to differentiate between curvature and dark energy for non-flat models of the universe (Stompor and Efstathiou, 1999). Lensing can also improve constraints on the dark energy model and neutrino masses, over and above the constraints from the lensed CMB power spectrum (de Putter et al., 2009; Benoit-Lévy et al., 2012; Allison et al., 2015a). Because lensing probes the distribution of matter, it can be used to study massive objects such as galaxy clusters (Seljak and Zaldarriaga, 2000; Dodelson, 2004; Holder and Kosowsky, 2004; Baxter et al., 2015). Galaxy lensing will in general yield more precise cluster mass results than CMB lensing (Richard et al., 2014; Jauzac et al., 2015; Limousin et al., 2015), but for high redshift objects with no background galaxies CMB lensing could prove useful in constraining cluster masses (Hu et al., 2007).

Initial lensing detections were achieved in cross-correlation using data from the Wilkinson Microwave Anisotropy Probe (WMAP) satellite (Smith et al., 2007; Hirata et al., 2008). Gravitational lensing has now been detected in both temperature and polarisation data by various CMB experiments such as the Atacama Cosmology Telescope (Das et al., 2014; van Engelen et al., 2015), the South Pole Telescope (van Engelen et al., 2012) and the POLARBEAR collaboration (Ade et al., 2014). The most significant lensing detection to date is the Planck satellite's $40\sigma$ measurement, which was achieved using a combination of temperature and polarisation data (Planck Collaboration et al., 2015d).

The radiation emitted by distant galaxies is gravitationally lensed by foreground galaxy clusters, a phenomenon known as galaxy lensing. Galaxy lensing occurs in both the strong lensing regime, in which multiple images of background galaxies are produced, and the weak lensing regime, in which the shapes of background galaxies are distorted (e.g. Kneib and Natarajan, 2011; Hoekstra et al., 2013). Galaxy lensing can be used to study the matter distribution of the cluster that forms the gravitational lens (Massey, 2010). In addition, the magnification caused by lensing means that galaxy clusters can act as telescopes that allow very distant galaxies to be observed (Richard et al., 2014). The geometry of the universe and the nature of dark energy can also be constrained by galaxy lensing (Jullo et al., 2010). The first double image of a quasar caused by strong gravitational lensing was detected by Walsh et al. (1979), although the authors were not convinced this was an effect of lensing, and speculated that the two images could be two similar quasars. Now observations of background galaxies with high-resolution telescopes such as the Hubble Space Telescope have allowed astronomers to reconstruct the matter distribution of the foreground galaxy clusters using multiple images from strong gravitational lensing (e.g. Jauzac et al., 2015), and to constrain the dark energy equation of state (e.g. Jullo et al., 2010). Distant galaxies have also been discovered using lensing (e.g. Richard et al., 2011). In addition, maps of the matter distribution have been produced using galaxy weak lensing reconstruction techniques, for example using the science verification data from the Dark Energy Survey (Chang et al., 2015).

Surveys of large scale structure, such as the Sloan Digital Sky Survey (SDSS), allow us to measure the galaxy power spectrum and constrain various cosmological parameters (e.g. Reid

et al., 2010; Rozo et al., 2010). Next generation optical/infrared experiments such as the Large Synoptic Survey Telescope (LSST) (Ivezic et al., 2008) and Euclid (Laureijs et al., 2011) will survey larger volumes of the sky with better sensitivity than current telescopes. The Square Kilometer Array (SKA) will probe the large scale structure of the universe at radio frequencies, using large volume HI intensity mapping surveys (which do not detect individual galaxies but rather the integrated emission in three-dimensional pixels), and later resolving the individual galaxies in the planned HI galaxy redshift survey (Maartens et al., 2015). All of these experiments will use gravitational lensing to probe the dark matter distribution. They will also study dark energy via the growth of large scale structure (by studying the evolution of the galaxy power spectrum directly, the growth of the matter power spectrum via gravitational lensing, and redshift-space distortions which depend on the growth rate), and the expansion history of the universe (which can be constrained by baryon acoustic oscillations and weak lensing) (Laureijs et al., 2011; Weinberg et al., 2013).

HI intensity mapping measures the integrated 21cm emission from neutral hydrogen on large scales at different redshifts, without resolving individual galaxies. Intensity mapping is a useful technique for rapidly surveying large volumes of the universe. This technique can be employed using telescopes with lower resolution and sensitivity than would be needed to detect individual galaxies, so although it will be used to great effect by the SKA (Santos et al., 2015), it can also be used by earlier, lower resolution dedicated experiments such as the Canadian Hydrogen Intensity Mapping Experiment (CHIME) (Vanderlinde and Chime Collaboration, 2014), the Baryon acoustic oscillations In Neutral Gas Observations experiment (BINGO) (Battye et al., 2012), Tianlai (Chen, 2015), and the Hydrogen Intensity and Real-time Analysis eXperiment (HIRAX) (HIRAX Collaboration, 2016) to place constraints on baryon acoustic oscillations and therefore dark energy.

CMB lensing reconstructions have been cross-correlated with other tracers of the dark matter distribution, such as quasars (Sherwin et al., 2012), the cosmic infrared background (Holder et al., 2013) and galaxies (Pearson and Zahn, 2014; Kuntz, 2015), including high redshift submillimetre galaxies (Bianchini et al., 2015) and radio galaxies (Allison et al., 2015b). Such cross-correlations constrain various clustering properties of the tracers, such as their bias with

respect to the underlying dark matter field. Cross-correlations of a foreground lens plane with lensing from two different background source planes (such as the CMB at $z \approx 1100$ and background sources for galaxy lensing at much lower redshifts) probe the geometrical distances to different redshifts, and thus constrain dark energy parameters (Jain and Taylor, 2003; Bernstein and Jain, 2004; Zhang et al., 2005; Das and Spergel, 2009). Combining results from CMB and galaxy lensing reconstructions (Hand et al., 2015; Liu and Hill, 2015) also allows us to constrain the amplitude of the density fluctuations probed by both types of lensing. In this thesis, we investigate the potential to detect the cross-correlation between CMB lensing reconstructed from Advanced ACTPol (Henderson et al., 2015) and HI intensity mapping from HIRAX (HIRAX Collaboration, 2016). A high signal to noise detection of this cross-correlation could be used to constrain the bias of neutral hydrogen with respect to the underlying dark matter field.

This thesis is structured as follows. In Chapter 2, we present the relevant cosmological background information, discussing the standard cosmological model and the growth of the early matter perturbations into the large scale structure that is responsible for lensing the CMB. We also review the primordial CMB and the weak gravitational lensing effect on CMB photons as they travel through space from the last scattering surface. We derive the real space CMB temperature and polarisation lensing estimators in Chapter 3 and show that they are the large-scale lensing field limit of the harmonic space estimators traditionally used. We investigate some of the properties and limitations of these estimators, and apply them to simulated lensed temperature and polarisation maps, demonstrating that the reconstruction based on lensed E and B mode polarisation maps is particularly accurate. A paper on real space CMB temperature and polarisation lensing estimators, based on the results in this chapter, is in preparation (Prince et al., 2016a). The cross-correlation of CMB lensing with HI intensity mapping is explored in Chapter 4. We find that this cross-correlation should be robustly detected using CMB lensing reconstructions from the upcoming Advanced ACTPol experiment (Henderson et al., 2015) and HI intensity mapping data from HIRAX (HIRAX Collaboration, 2016). This work will be included in an upcoming paper on CMB lensing and HI intensity mapping (Prince et al., 2016b).

# CHAPTER 2

# Cosmological Background

## 2.1 Standard Cosmological Model

We are—as far as we know—living in a smooth, expanding, spatially flat universe whose energy content is dominated by dark energy and dark matter, and which can be neatly described by just six cosmological parameters (Planck Collaboration et al., 2015c). In this section we explore the theoretical foundations and some features of the standard ΛCDM model of the universe.

### 2.1.1 Cosmological Principle

The cosmological principle asserts that on large scales the universe is isotropic (symmetric under rotations) and homogenous (symmetric under translations). We do not occupy a privileged place in the universe, so the part of the universe that we can observe should be a fair sample of the whole, governed by the same laws and yielding the same scientific results as would be obtained in a different region. The observed near-isotropy of the cosmic microwave background (Smoot et al., 1992) and the homogeneity of galaxy surveys on large scales (Wu et al., 1999) provide

observational support for the cosmological principle.

### 2.1.2 General Relativity

Einstein's theory of general relativity (Einstein, 1915) allows us to describe gravity as a geometric effect, in which massive objects distort spacetime. Mathematically, the geometric distortions are encoded in a spacetime metric which is related to the matter and energy content of the universe by Einstein's field equations.

#### Robertson-Walker Metric

The general form for the spacetime interval in general relativity is $ds^2 = g_{\mu\nu}dx^\mu dx^\nu$, where $g_{\mu\nu}$ is the symmetric metric tensor, $dx^0 = cdt$ is the time coordinate and $dx^i, i \in \{1, 2, 3\}$ are the three spatial coordinates. We can use the cosmological principle to determine an appropriate metric for the standard model of the universe (Robertson, 1935). The spacetime element takes the following form in comoving coordinates, that is to say a spatial coordinate system that expands with the universe, so that a comoving observer (who observes the universe to be isotropic and homogenous at any instant in time) remains at fixed spatial coordinates:

$$ds^2 = -c^2dt^2 + a^2(t)\left[d\chi^2 + f_K^2(\chi)(d\theta^2 + \sin^2\theta d\phi^2)\right], \tag{2.1}$$

where $f_K(\chi)$ depends on the curvature of the universe,

$$f_K(\chi) = \begin{cases} K^{-\frac{1}{2}}\sin(K^{\frac{1}{2}}\chi) & \text{K >0 (closed universe)} \\ \chi & \text{K = 0 (flat universe)} \\ (-K)^{-\frac{1}{2}}\sinh((-K)^{\frac{1}{2}}\chi) & \text{K <0 (open universe)} \end{cases} \tag{2.2}$$

The spatial curvature $K$ can be constrained by studying the observed angular scales of CMB anisotropies, which depend on the geometry of the universe. CMB experiments have found the universe to be spatially flat (Spergel et al., 2003), (Planck Collaboration et al., 2015c), so we take $K = 0$ in the following.

We define the conformal time $\eta$ to be the comoving distance that light could have travelled since $t = 0$. $\eta$ is thus the comoving radius of the observable universe, called the comoving horizon:

$$\eta = \int_0^t \frac{cdt'}{a(t')}. \tag{2.3}$$

Writing the spacetime interval in terms of the conformal time gives

$$ds^2 = a^2(\eta)\left[-d\eta^2 + d\chi^2 + \chi^2(d\theta^2 + \sin^2\theta d\phi^2)\right]. \tag{2.4}$$

The scale factor $a$ relates the fixed comoving separation between two comoving observers to the physical distance between them, which increases with the expansion of the universe. For convenience we stipulate that the value of the scale factor at the present time is $a_0 = 1$.

**Einstein's Field Equations**

Einstein's field equations relate the geometry of spacetime to the matter and energy content of the universe, allowing us to determine the evolution of the universe's expansion from its contents:

$$G^\mu_\nu + \Lambda g^\mu_\nu = \frac{8\pi G}{c^4} T^\mu_\nu \,. \tag{2.5}$$

The geometry of spacetime is encapsulated by the Einstein tensor $G^\mu_\nu$, which depends on the spacetime metric. Dark energy is included in the form of $\Lambda$, the cosmological constant, a vacuum energy that causes the accelerated expansion of the universe. $T^\mu_\nu$ is the stress-energy tensor, which is taken to be that of a perfect isotropic fluid with energy density $\rho$ and pressure $p$:

$$T^\mu_\nu = \begin{pmatrix} -\rho c^2 & 0 & 0 & 0 \\ 0 & p & 0 & 0 \\ 0 & 0 & p & 0 \\ 0 & 0 & 0 & p \end{pmatrix}. \tag{2.6}$$

Einstein's field equations, sometimes known in the form below as the Friedmann (2.7) and acceleration (2.8) equations, then allow us to determine the evolution of the scale factor given the contents of the universe:

$$\left(\frac{\dot{a}}{a}\right)^2 = \frac{8\pi G}{3}\rho - \frac{Kc^2}{a^2} + \frac{\Lambda c^2}{3} \tag{2.7}$$

$$\frac{\ddot{a}}{a} = -\frac{4\pi G}{3}(\rho + \frac{3p}{c^2}) + \frac{\Lambda c^2}{3}. \tag{2.8}$$

The Robertson-Walker metric with a scale factor obeying these evolution equations is called the Friedmann-Lemaître-Robertson-Walker metric, because Friedmann and Lemaître independently used these equations to solve for the evolution of the scale factor and thus the metric (Friedmann, 1922) (Lemaître, 1927). We can combine Equations (2.7) and (2.8) to obtain the conservation equation

$$\frac{d}{dt}(a^3\rho c^2) = -p\frac{d}{dt}a^3, \tag{2.9}$$

which expresses the first law of thermodynamics: the change in energy in a certain volume (on the left) is equal to the pressure times the change in proper volume (on the right).

#### Hubble Parameter

Hubble was the first to find observational evidence for the expansion of the universe predicted by Lemaître (Hubble, 1929; Lemaître, 1927), when he found a linear relation between the recessional velocities of Cepheid variable stars and their proper distances: $v = H_0 D$. This equation is known as Hubble's law, and the proportionality constant $H_0$ is called the Hubble constant. The Hubble parameter $H(t) \equiv \frac{\dot{a}}{a}$ describes how the scale factor changes with time. The Hubble constant is the Hubble parameter at present time, $H_0 \equiv H(t_0)$.

### 2.1.3 Equation of State and Density Parameters

The equation of state relates the pressure of matter to its energy density: $p = p(\rho) = w\rho c^2$, where $w$ is a constant. Dust has no pressure so $w = 0$, while for radiation and other relativistic matter $w = \frac{1}{3}$, and for the energy associated with the cosmological constant $w = -1$.

Substituting our equation of state into Equation (2.9), we find that

$$\rho(t) = a^{-3(w+1)}(t)\rho_0\,. \tag{2.10}$$

Thus the energy density of dust evolves as $\rho_m(t) = a^{-3}(t)\rho_{m,0}$ and for relativistic matter $\rho_r(t) = a^{-4}(t)\rho_{r,0}$. This can be understood intuitively: if the number density of particles remains constant

in a constant comoving volume, then the number density in the corresponding proper volume changes according to a factor of $a^{-3}$ since the proper length of each edge of a cube of comoving volume scales as $a$. For dust, the energy density $\rho$ is directly proportional to the number density, and hence we have $\rho_m \propto a^{-3}(t)$. Relativistic particles behave like photons, whose wavelength is stretched by a factor of $a$, and whose frequency and thus energy therefore decrease as $a^{-1}$, meaning that the total energy density scales as $a^{-4}$. Dark energy in the form of a cosmological constant maintains constant energy density even as the universe expands.

The radiation energy density falls off faster than the matter (dust) density. The universe was in a radiation dominated state at early times, but later entered a phase of matter domination. Matter-radiation equality occurred when $\rho_m = \rho_r$, so $a_{eq} = \frac{\rho_{r,0}}{\rho_{m,0}}$, where a subscript of zero indicates the value at the present time. The matter and radiation energy density decrease with time while the cosmological constant energy density remains constant, leading to a transition from matter domination to the current era of dark energy domination.

The critical density of the universe is the total energy density density required for the universe to be spatially flat. A universe with actual density larger than the critical density would be closed and have positive curvature, while a universe with lower density would be open, with negative curvature. As previously mentioned, we know that our universe is very close to spatially flat, with density approximately equal to the critical density, which is

$$\rho_c \equiv \frac{3H_0^2}{8\pi G} \tag{2.11}$$

at the present time. We define the density parameter for a type of matter $x$ to be the density of $x$ in units of $\rho_c$:

$$\Omega_x \equiv \frac{\rho_x}{\rho_c}\,, \tag{2.12}$$

where $x = m$ denotes ordinary matter (baryonic and dark matter), and $x = r$ denotes radiation or relativistic matter. For the energy density associated with the cosmological constant $\Lambda$ or the curvature $K$, we define

$$\Omega_\Lambda \equiv \frac{\Lambda c^2}{3H_0^2} \qquad \text{and} \qquad \Omega_K \equiv \frac{Kc^2}{H_0^2}\,. \tag{2.13}$$

The curvature density parameter is determined by how much the total energy density from matter, radiation and the cosmological constant differs from the critical density: $\Omega_K = \Omega_{m,0} + \Omega_\Lambda - 1$, where we have neglected radiation at late times when it has a very low energy density.

### 2.1.4 Evolution of the Scale Factor and Hubble Parameter

We can determine the evolution of the scale factor $a(t)$, by substituting the expression for $\rho(a)$ from Equation (2.10) into the Friedmann Equation (2.7). Again we set $K = 0$ (flat universe) and for now we neglect the cosmological constant $\Lambda$. We obtain:

$$a(t) = a_0 \left(\frac{t}{t_0}\right)^{\frac{2}{3(w+1)}} . \tag{2.14}$$

Therefore for a dust dominated universe $a(t) \propto t^{\frac{2}{3}}$, and for relativistic matter $a(t) \propto t^{\frac{1}{2}}$. Clearly $a$ is an increasing function of t, and hence the universe is expanding in both the matter and radiation dominated eras, consistent with Lemaître's predictions and Hubble's observations.

The deceleration parameter quantifies how the expansion rate of the universe is changing:

$$q = -\frac{\ddot{a}a}{\dot{a}^2} = -\frac{\ddot{a}}{aH^2}. \tag{2.15}$$

For matter or radiation dominated eras, the expansion rate slows with time, producing decelerating expansion with a deceleration parameter $q > 0$. However in the dark energy dominated era the universe expands exponentially, $a(t) \propto e^{Ht}$, resulting in a negative deceleration parameter $q < 0$. Observations of Type Ia supernovae, which serve as 'standard candles' with known luminosity, have shown that the universe is in fact undergoing accelerated expansion (Riess et al., 1998; Perlmutter et al., 1999), consistent with dark energy in the form of a cosmological constant.

We can rewrite the Friedmann Equation (2.7) in terms of the density parameters defined above as

$$H^2(t) = H_0^2 \left(a^{-4}(t)\Omega_{r,0} + a^{-3}(t)\Omega_{m,0} + a^{-2}(t)(1 - \Omega_{m,0} - \Omega_\Lambda) + \Omega_\Lambda\right) , \tag{2.16}$$

giving the expansion history of the universe as a function of its contents. We can determine the age of the universe $t_0$ using the fact that $dt = \frac{da}{\dot{a}} = \frac{da}{aH}$, giving

$$t_0 = \frac{1}{H_0} \int_0^1 \frac{da}{\sqrt{a^{-1}\Omega_{m,0} + (1 - \Omega_{m,0} - \Omega_\Lambda) + a^2\Omega_\Lambda}} \tag{2.17}$$

In calculating the above expression for $t_0$, we have again neglected $\Omega_r$. This omission does not result in a large error because the universe was only radiation dominated for a comparatively short period of time.

We can compare the predicted values of $t_0$ for various parameter values with the ages of objects in our universe to constrain the parameters. For example, a completely matter dominated, flat universe ($\Omega_m = 1$, $\Omega_K = \Omega_\Lambda = \Omega_r = 0$) would have age $t_0 = \frac{2}{3}H_0^{-1}$, or of order 10 billion years. This is younger than the oldest stars, making a purely matter dominated universe unviable. The current best-fit parameters for the $\Lambda$CDM model place the age of the universe at 13.8 billion years, which is consistent with the oldest observed stars (Planck Collaboration et al., 2015c).

### 2.1.5 Redshift

The expansion of the universe means that light from distant galaxies has its wavelength stretched as it travels, resulting in an observed redshift: light arrives at observer with a lower energy than it had when leaving the source. Redshift $z$ is defined as the fractional change in wavelength $z = \frac{\lambda_o - \lambda_e}{\lambda_e}$, where $o$ stands for the observed wavelength and $e$ for emitted. The redshift can be related to the scale factors at emission and observation:

$$1 + z = \frac{\lambda_o}{\lambda_e} = \frac{a(t_o)}{a(t_e)}\,. \tag{2.18}$$

If we take $t_o$ to be the present time, and $t_e$ to be a general time $t$, then $1 + z = 1/a(t)$. Redshift is a useful quantity as it is often possible to determine an object's redshift observationally, by the shifted frequencies of known spectral lines. We use redshift as a proxy for distance (objects at higher redshifts are further away) or time (objects at higher redshifts emitted the observed radiation at earlier times).

### 2.1.6 Distances

There are different ways to measure distance in our expanding universe, which all give different results for objects at high redshifts but reduce to Hubble's law $D = \frac{cz}{H_0}$ at low redshifts. We

explore four different ways of measuring distance here, three of which are plotted as a function of redshift in Figure (2.1).

### Proper Distance

The proper distance $D_{prop}$ between two points is calculated using the travel time of a light ray between these points: $dD_{prop} = cdt$. For a light ray propagating from a redshift $z$ to an observer at $z = 0$, Equation (2.16) gives

$$D_{prop}(z) = c\int_{t(z)}^{t_0} dt = \frac{c}{H_0}\int_{a(z)}^{a(z_0)} \frac{da}{\sqrt{a^{-1}\Omega_{m,0} + (1 - \Omega_{m,0} - \Omega_\Lambda) + a^2\Omega_\Lambda}}\,. \tag{2.19}$$

### Comoving Distance

The comoving distance comes from the definition of comoving coordinates, $dD_{com} = d\chi = \frac{dD_{prop}}{a}$. Integrating over redshift we obtain (Dodelson, 2003)

$$D_{com}(z) = \chi = \int_0^z \frac{cdz'}{H(z')}. \tag{2.20}$$

### Angular Diameter Distance

The angular diameter distance is the distance an object of known size appears to be at based on its apparent angular size on the sky: $D_{ang} = \frac{l}{\theta}$, where $l$ is the physical length of the object and $\theta$ is the angle it subtends (Liddle, 2003). In a flat universe,

$$D_{ang} = a\chi = \frac{\chi}{1+z}\,. \tag{2.21}$$

### Luminosity Distance

The luminosity distance is inferred from the flux of radiation seen by the observer, assuming the inverse square law for the reduction of intensity with distance from the source. Thus $D_{lum}^2 = \frac{L}{4\pi S}$ where $L$ is the luminosity of the source and $S$ is the flux density of the radiation at the observer (Liddle and Lyth, 2000). Radiation from a source at a comoving distance $\chi$ will have spread out over a sphere of radius $a\chi$ by the time it reaches the observer at the origin. Taking into account

the loss of energy of each photon due to redshift and the decreased frequency of the photons (each contributing a factor of $(1+z)^{-1}$ to $S$), we find that $S = \frac{L}{a\chi(1+z)^2}$ (Liddle, 2003). Thus

$$D_{lum} = \frac{\chi}{a} = \chi(1+z)\,. \tag{2.22}$$

It is clear from Figure (2.1) that the comoving distance, angular diameter distance and luminosity distance give the same results for nearby objects. However they display very different behavior for distant objects: the angular diameter distance reaches a maximum after which it falls off so that more distant objects actually appear larger on the sky; the comoving distance asymptotically approaches a constant $2c/H_0$ for large $z$; and the luminosity distance continues to increase with redshift.

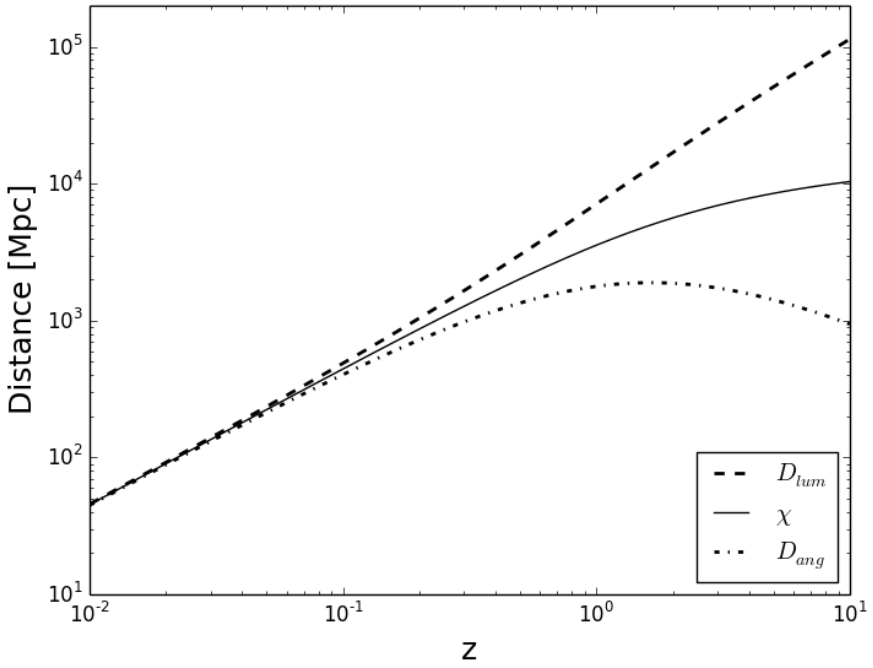


Figure 2.1: A comparison of the luminosity distance $D_{lum}$, comoving distance $\chi$, and angular diameter distance $D_{ang}$ as a function of redshift. Produced using the cosmolopy package for Python created by R Kramer[1] based on (Hogg, 1999), using the most recent Planck cosmological parameters (Planck Collaboration et al., 2015c).

[1] `http://roban.github.com/CosmoloPy`

## 2.2 Perturbation Theory and Large-Scale Structure Formation

Although the universe is homogeneous and isotropic on very large scales, it is clearly irregular on smaller scales as evidenced by the presence of structures such as galaxies and galaxy clusters. It is believed that the structures in the universe today were initially very small density perturbations (Peebles and Yu, 1970; Peebles, 1982). With time, overdense regions grew more dense because of gravitational attraction and underdense regions lost their matter to overdense regions. Dark matter played a crucial role in this process, because it does not experience radiation pressure, so the dark matter overdensities began to collapse before the baryonic matter, which was coupled to radiation at early times. The universe is spanned by a cosmic web of dark matter haloes and filaments, into which the baryonic matter falls under the force of gravity, forming galaxies and galaxy clusters.

### 2.2.1 Perturbed Einstein Equations

We can write the metric, Einstein and stress-energy tensors in a perturbed spacetime as the sum of the unperturbed background value and a small perturbation.

$$g_{\mu\nu} = \bar{g}_{\mu\nu} + \delta g_{\mu\nu} \tag{2.23}$$

$$G^{\mu}_{\nu} = \bar{G}^{\mu}_{\nu} + \delta G^{\mu}_{\nu} \tag{2.24}$$

$$T^{\mu}_{\nu} = \bar{T}^{\mu}_{\nu} + \delta T^{\mu}_{\nu} \tag{2.25}$$

We assume that the perturbations and their first and second derivatives are sufficiently small that any product of these quantities is negligible, i.e. we only keep linear order perturbation terms. This linear treatment is valid until fairly late times when the matter perturbations become nonlinear. From now on we will take $c = 1$ to simplify calculations.

We can separate Einstein's Field Equations $G^{\mu}_{\nu} = 8\pi G T^{\mu}_{\nu}$ (neglecting the cosmological constant) into an unperturbed background component $\bar{G}^{\mu}_{\nu} = 8\pi G \bar{T}^{\mu}_{\nu}$, which we dealt with in the previous section, and an equation relating the geometric perturbations to the stress-energy per-

turbations:

$$\delta G^{\mu}_{\nu} = 8\pi G \delta T^{\mu}_{\nu}. \tag{2.26}$$

### Metric Perturbations

We can rewrite $g_{\mu\nu} = \bar{g}_{\mu\nu} + \delta g_{\mu\nu} = a^2(\eta_{\mu\nu} + h_{\mu\nu})$, where $\eta_{\mu\nu}$ is the Minkowski metric (not to be confused with the conformal time $\eta$) and

$$h_{\mu\nu} = \begin{pmatrix} -2A & -B_i \\ -B_i & -2D\delta_{ij} + 2E_{ij} \end{pmatrix} . \tag{2.27}$$

We find that the spacetime interval is

$$ds^2 = a^2(\eta)[-(1+2A)d\eta^2 - 2B_i d\eta dx^i + ((1-2D)\delta_{ij} + 2E_{ij})dx^i dx^j] . \tag{2.28}$$

It can be seen that $A$ and $D$ transform as scalars, $B_i$ transforms as a 3-vector and $E_{ij}$ transforms as a 3-tensor under rotations in the background spacetime (Kurki-Suonio, 2011).

We can decompose $B_i$ into a vector and a scalar part, $B_i = -B_{,i} + B^V_i$, where $B$ is a scalar, $B_{,i}$ is the derivative of $B$ with respect to the $i^{th}$ coordinate, and $\vec{B}^V$ is a vector with $\nabla \cdot \vec{B}^V = 0$. Similarly, we can write $E_{ij}$ in terms of a scalar, vector and tensor: $E_{ij} = E^S_{ij} + E^V_{ij} + E^T_{ij}$. The first term is $E^S_{ij} = (\partial_i\partial_j - \frac{1}{3}\delta_{ij}\nabla^2)E$ for scalar $E$. The second term is given by $E^V_{ij} = -\frac{1}{2}(E_{i,j} - E_{j,i})$ where $E_i$ are the components of a divergence-free vector $\vec{E}$. The third term is a symmetric, transverse and trace-free tensor.

The metric tensor perturbations can therefore be described by four scalars $A, B, D$ and $E$; two divergence-free vectors $\vec{B}^V$ and $\vec{E}$ and one tensor $E^T_{ij}$. Taking the constraints on the vectors and tensors into account, this corresponds to ten degrees of freedom: four scalar degrees of freedom, four vector degrees of freedom and two tensor degrees of freedom. We will see that four of these degrees of freedom correspond to a choice of coordinates.

### Stress-Energy Tensor Perturbations

The background stress-energy tensor is in the form of a perfect fluid, as in Equation (2.6). The condition of homogeneity requires that the background energy density and pressure are independent of position: $\bar{\rho} = \bar{\rho}(\eta)$ and $\bar{p} = \bar{p}(\eta)$. Isotropy requires that the fluid has no peculiar velocity,

as this would locally single out a specific direction, so $\bar{u}^i = 0 \, \forall i \in \{1, 2, 3\}$, i.e. the fluid is stationary in the background universe.

There are some perturbations which keep $T^\mu_\nu = \bar{T}^\mu_\nu + \delta T^\mu_\nu$ in its perfect fluid form. These are

$$\rho = \bar{\rho} + \delta\rho \,, \qquad p = \bar{p} + \delta p \qquad \text{and} \qquad u^i = \bar{u}^i + \delta u^i = \delta u^i \equiv \frac{v^i}{a} \,. \tag{2.29}$$

We will use $\delta$ to denote $\frac{\delta\rho}{\bar{\rho}}$. To first order, $v^i = \frac{dx^i}{d\eta}$, the coordinate velocity, which is the same as the physical velocity of the fluid as seen by a comoving observer. We can express $u^\mu$ and $u_\mu$ in terms of $v_i$ and elements of the metric tensor (used to raise and lower indices). We find that $u^\mu = \frac{1}{a}(1 - A, v_i)$ and $u_\mu = a(-1 - A, v_i - B - i)$. Substituting the perturbed expressions into $T^\mu_\nu = (\rho + p)u^\mu u_\nu + u\delta^\mu_\nu$, we can compare the perturbed stress-energy tensor to the background stress-energy tensor to find $\delta T^\mu_\nu$. There are 5 more degrees of freedom, correspond to anisotropic stress perturbations $\Sigma_{ij}$ which prevent $T^\mu_\nu$ from being a perfect fluid.

We can rewrite $v_i$ as the sum of a scalar part and a vector part $v_i = v^S_i + v^V_i$, and $\Sigma_{ij} = \Sigma^S_{ij} + \Sigma^V_{ij} + \Sigma^T_{ij}$ where $\Sigma^S_{ij}$ depends on a scalar $\Sigma$, $\Sigma^V_{ij}$ depends on a vector $\Sigma_i$ and $\Sigma^T_{ij}$ is a tensor. Again, we have four scalar degrees of freedom (from $\delta\rho$, $\delta p$, $v$ and $\Sigma$), four vector degrees of freedom (two each from $v^V_i$ and $\Sigma^V_i$) and two tensor degrees of freedom (from $\Sigma^T_{ij}$). We will neglect the anisotropic stress in the rest of this section. For high precision calculations it should be included as at early times there was anisotropic pressure present from neutrinos.

The perturbation to the Einstein tensor, $\delta G_{\mu\nu}$ can be divided into scalar, vector and tensor parts, coming from the scalar, vector and tensor parts of $\delta g_{\mu\nu}$ respectively. The stress energy perturbation $\delta T_{\mu\nu}$ can be similarly split up. In linear perturbation theory, the scalar, vector and tensor perturbations evolve independently, and so we can treat them separately. The scalar perturbations are most relevant to structure formation, so we will focus on these in the following discussion. Vector perturbations decay with time and do not have a large influence at later times. Tensor perturbations correspond to gravitational waves, and have cosmological significance, but will not be a focus in this section.

### 2.2.2 Gauge Transformations

For a given coordinate system in the background spacetime, there are various possible coordinate systems in the perturbed spacetime. A gauge transformation is a transformation between two different coordinate systems in the perturbed spacetime. If we have one set of coordinates denoted $x^\alpha$ and one denoted $\tilde{x}^\alpha$ in the perturbed spacetime, we can relate them using $\tilde{x}^\alpha = x^\alpha + \xi^\alpha$ where $\xi^\alpha$ and its derivatives are small enough to keep only linear terms.

We find (Kurki-Suonio, 2011) that perturbations to covariant and mixed tensors of rank 2 transform as

$$\widetilde{\delta B}_{\mu\nu} = \delta B_{\mu\nu} - \xi^\alpha{}_{,\mu}\,\bar{B}_{\alpha\nu} - \xi^\beta{}_{,\nu}\,\bar{B}_{\mu\beta} - \bar{B}_{\mu\nu,\gamma}\,\xi^\gamma \tag{2.30}$$

$$\widetilde{\delta B}^\mu_\nu = \delta B^\mu_\nu + \xi^\mu{}_{,\alpha}\,\bar{B}^\alpha_\nu - \xi^\beta{}_{,\nu}\,\bar{B}^\mu_\beta - \bar{B}^\mu_{\nu,\gamma}\,\xi^\gamma \tag{2.31}$$

We can express the spatial components $\vec{\xi}$, where $\xi^\alpha{=}(\xi^0, \vec{\xi})$, as the sum of a curl free scalar part ($-\nabla\xi$ for scalar $\xi$) and a divergence-free vector part ($\vec{\xi_V}$) i.e. $\xi^i = \xi^i_V + \delta^{ij}\xi_{,j}$. The vector part does not affect scalar perturbation transformations, so we will neglect it in the following as we will focus on scalar perturbations. We therefore use $\xi^\alpha{=}(\xi^0, -\nabla\xi)$.

#### Scalar Perturbations

We use Equation (2.30) to write the gauge transformation equations for the scalar metric perturbation quantities $A$, $D$, $B$ and $E$ in terms of $\xi^0$ and $\xi$ as

$$\tilde{A} = A - \xi^{0\prime} - \frac{a'}{a}\xi^0 \tag{2.32}$$

$$\tilde{B} = B + \xi' - \xi^0 \tag{2.33}$$

$$\tilde{D} = D - \frac{1}{3}\nabla^2\xi + \frac{a'}{a}\xi^0 \tag{2.34}$$

$$\tilde{E} = E + \xi \tag{2.35}$$

For scalar perturbations of the stress-energy tensor, $v_i = v^s_i = -v_{,i}$, so we find using Equation (2.31)

$$\widetilde{\delta\rho} = \delta\rho - \bar{\rho}'\xi^0\,, \qquad \widetilde{\delta p} = \delta p - \bar{p}'\xi^0 \qquad \text{and} \qquad \tilde{v} = v + \xi'\,. \tag{2.36}$$

### Bardeen Potentials

The Bardeen potentials (Bardeen, 1980)

$$\Psi \equiv A + \mathcal{H}(B - E') + (B - E')' \tag{2.37}$$

$$\Phi \equiv D + \frac{1}{3}\nabla^2 E - \mathcal{H}(B - E') \tag{2.38}$$

are invariant under gauge transformations.

### Conformal-Newtonian Gauge

We can use our gauge freedom to set $E^N = B^N = 0$, where the superscript $N$ refers to the conformal-Newtonian gauge (Hu and Sugiyama, 1995). To transform to the conformal-Newtonian gauge from another gauge, we set

$$\xi = -E \tag{2.39}$$

$$\xi^0 = -B + E'. \tag{2.40}$$

This transformation gives

$$A^N = \Psi \tag{2.41}$$

$$D^N = \Phi, \tag{2.42}$$

so in the conformal-Newtonian gauge, the two nonzero scalar metric potentials are equal to the gauge-invariant Bardeen Potentials. The Bardeen potentials have straightforward physical interpretations in this gauge: $\Psi$ describes how the Newtonian potential is perturbed, while $\Phi$ gives the perturbation to the spatial curvature (Dodelson, 2003).

The perturbed spacetime interval is given by

$$ds^2 = a^2(\eta)[-(1 + 2\Psi)d\eta^2 + (1 - 2\Phi)\delta_{ij}dx^i dx^j], \tag{2.43}$$

from which we can find the components of the perturbed metric and thus the perturbed Einstein tensor. A comparison with the unperturbed Einstein tensor will yield the perturbations $\delta G^\mu_\nu$.

For scalar perturbations in the conformal-Newtonian gauge, $v = -v_{,i}$ and $B = 0$, and the perturbation to the stress energy tensor is thus

$$\delta T^{\mu}_{\nu} = \begin{pmatrix} -\delta\rho^N & -(\bar{\rho}+\bar{p})(v^N{}_{,i}) \\ (\bar{\rho}+\bar{p})v^N{}_{,i} & \delta p^N \delta^i_j \end{pmatrix}. \tag{2.44}$$

**Synchronous Gauge**

Another commonly used gauge is the synchronous gauge, in which $A = 0 = B_i$ (Bond and Efstathiou, 1984). The synchronous gauge is often used in computations, as the equations governing the evolution of perturbations are better-behaved numerically in the synchronous gauge than in the conformal Newtonian gauge.

### 2.2.3 Equations Governing the Evolution of Perturbations

Einstein's Field Equations for scalar perturbations of a perfect fluid ($\Sigma = 0$ so $\Phi = \Psi$) in the conformal-Newtonian gauge are given by

$$\nabla^2\Psi = \frac{3}{2}\mathcal{H}^2[\delta^N + 3\mathcal{H}(1+w)v^N] \tag{2.45}$$

$$\Psi' + \mathcal{H}\Psi = \frac{3}{2}\mathcal{H}^2(1+w)v^N \tag{2.46}$$

$$\Psi'' + 3\mathcal{H}\Psi' + (2\mathcal{H}' + \mathcal{H}^2)\Psi = \frac{3}{2}\mathcal{H}^2\frac{\delta p^N}{\bar{\rho}} \tag{2.47}$$

where $w$ comes from the equation of state $p = w\rho$, and $\mathcal{H} \equiv \frac{a'}{a}$ is the conformal Hubble parameter, where $'$ denotes differentiation with respect to conformal time $\eta$. The first equation is a constraint equation (if we were not considering a perfect fluid, then we would have two constraint equations) and the last two equations describe the evolution of $\Psi$.

We can use the condition of energy-momentum conservation

$$T^{\mu}_{\nu;\mu} = 0 \tag{2.48}$$

to obtain first order equations for the perturbations $\delta$ and $v$.

For perfect fluid scalar perturbations in the conformal-Newtonian gauge the perturbations satisfy the continuity equations:

$$(\delta^N)' = (1+w)(\nabla^2 v^N + 3\Phi') + 3\mathcal{H}(w\delta^N - \frac{\delta p}{\bar{\rho}}) \tag{2.49}$$

$$(v^N)' = -\mathcal{H}(1-3w)v^N - \frac{w'}{1+w}v^N + \frac{\delta p^N}{\bar{\rho}+\bar{p}} + \Phi \tag{2.50}$$

**Full System of Equations**

We consider a universe containing baryons (which we will take to include electrons), cold dark matter, photons, massless neutrinos and dark energy. The total energy density is thus

$$\rho = \rho_b + \rho_m + \rho_\gamma + \rho_\nu + \rho_{DE}\,. \tag{2.51}$$

The pressures are given by $p_b = 0 = p_m$, $p_\gamma = \frac{\rho_\gamma}{3}$, $p_\nu = \frac{\rho_\nu}{3}$ and $p_{DE} = -\rho_{DE}$. We assume that there are no perturbations in the dark energy. We need to consider interactions between photons and baryons, but can ignore interactions between the other components.

We Fourier-decompose $\delta\rho$ and $v$ as

$$\delta\rho(\eta, \vec{x}) = \sum_{\vec{k}} (\delta\rho_{\vec{k}}) e^{i\vec{k}\cdot\vec{x}} \tag{2.52}$$

$$v(\eta, \vec{x}) = \sum_{\vec{k}} \frac{v_{\vec{k}}}{k}\, e^{i\vec{k}\cdot\vec{x}}, \tag{2.53}$$

where the extra factor of $k = |\vec{k}|$ in the decomposition of $v$ is added so that $v$ has the same dimension as $v_i^S$ (in Fourier space $v_i^S = v_{,i}$ becomes $v_i^S = -i\frac{k_i}{k}v$) (Liddle and Lyth, 2000). For linear perturbations different Fourier modes $\vec{k}$ are uncorrelated, so we can treat each mode separately and work with their amplitudes $\delta\rho_{\vec{k}}$ and $v_{\vec{k}}$, dropping the subscript $\vec{k}$ in the following. Note that $k$ is the comoving wavenumber, which is related to the physical wavenumber $k_{phys}$ by $k = a\,k_{phys}$, where $a$ is the scale factor. Our continuity equations (2.49, 2.49) for scalar

perturbations in the conformal-Newtonian gauge become, in Fourier space,

$$\delta_m' = -kv_m + 3\Phi' \tag{2.54}$$

$$v_m' = -\mathcal{H}v_m + k\Phi \tag{2.55}$$

$$\delta_b' = -kv_b + 3\Phi' + \text{ (collision term)} \tag{2.56}$$

$$v_b' = -\mathcal{H}v_b + k\Phi + \text{ collision term} \tag{2.57}$$

$$\delta_\gamma' = -\frac{4}{3}kv_\gamma + 4\Phi' + \text{ (collision term)} \tag{2.58}$$

$$v_\gamma' = \frac{1}{4}k\delta_\gamma + k\Phi + \text{ collision term} \tag{2.59}$$

$$\delta_\nu' = -\frac{4}{3}kv_\gamma + 4\Phi' \tag{2.60}$$

$$v_\nu' = \frac{1}{4}k\delta_\gamma + k\Phi \tag{2.61}$$

The collision terms in brackets can be neglected, as the only collision effect that turns out to be important is momentum transfer between photons and baryons, captured in the collision terms in the velocity equations (Kurki-Suonio, 2011). In addition to these equations, we use the Einstein equations of which two will be independent at early times when the baryons and photons are tightly coupled. We can find equivalent equations in the synchronous gauge.

Solving the above set of equations for the cold dark matter component, we find that for superhorizon scales, $k \ll \mathcal{H}$, the density remains constant. The comoving Hubble scale $\mathcal{H}^{-1}$ increases with time, so superhorizon density perturbations enter the horizon when $\mathcal{H}^{-1}$ increases past $k$. Once the modes have entered the horizon, they begin to grow proportional to $\ln a$ in the radiation dominated era and $a$ in the matter dominated era as shown in the table below. The density contrast in the synchronous gauge can be calculated from the conformal Newtonian gauge result (Ma and Bertschinger, 1995, Eq. (27a)). The evolution of superhorizon modes depends on the gauge choice, but on subhorizon scales general relativistic effects become less important, and all of the gauges approach the Newtonian result.

| **Conformal-Newtonian Gauge** | Subhorizon ($d \ll d_H$) | Superhorizon ($d \gg d_H$) |
|---|---|---|
| Radiation dominated era ($a \ll a_{eq}$) | $\delta_m^N \propto \ln(a)$ | $\delta_m^N =$ constant |
| Matter dominated era ($a \gg a_{eq}$) | $\delta_m^N \propto a$ | $\delta_m^N =$ constant |

### 2.2.4 Evolution of the Power Spectrum

#### Statistics of Random Fields

We describe the statistical properties of the density perturbations or the gravitational potential by their power spectrum, which gives the amplitude of fluctuations on different spatial scales. We assume that the density perturbations were caused by an isotropic, homogeneous random process and we denote our density contrast by $\delta(\vec{x})$, where $\vec{x}$ is the spatial coordinate 3-vector. We obtain the amplitude of a mode with wavevector $\vec{k}$ by taking the Fourier transform of the density field,

$$\delta(\vec{k}) = \int d^3\vec{x} e^{-i\vec{k}\cdot\vec{x}} \delta(\vec{x}) \,. \tag{2.62}$$

The matter power spectrum for a wavevector $\vec{k}$ is defined to be the power of that $\vec{k}$ mode, i.e. the amplitude of the mode squared. Different $\vec{k}$ modes are uncorrelated while the perturbations are still linear, so the dark matter power spectrum is given by

$$\langle \delta_m(\vec{k}) \delta_m^*(\vec{k'}) \rangle = (2\pi)^3 \delta_D^3(\vec{k} - \vec{k'}) P^m(k) \,, \tag{2.63}$$

where the power spectrum $P^m(\vec{k}) = P^m(k)$ by isotropy, $\delta_D^3$ is the three dimensional Dirac delta function (which is 0 unless $\vec{k} = \vec{k'}$), and $\delta_m = \frac{\delta\rho_m}{\bar{\rho}_m}$, where $m$ refers to cold dark matter. The angular brackets denote an expectation value, taken in theory by averaging over many realisations of the matter density from the underlying statistical distribution. In reality we only have one universe, or one realisation, so we average over the density contrast in many regions of the sky.

The power spectrum is in fact the Fourier transform of the correlation function $\xi(r)$, where $\xi(r)$ is the probability over random that if there is an overdense region at $\vec{x}$, there is also an overdense region at $\vec{x} + \vec{r}$. The correlation function is a function of $r = |\vec{r}|$ because of isotropy, and can be written as $\xi(r) \equiv \langle \delta_m(\vec{x}) \delta_m(\vec{x} + \vec{r}) \rangle$.

We can also define the power spectrum of the gravitational potential, $P^\phi(k)$, where

$$\langle \phi(\vec{k}) \phi^*(\vec{k'}) \rangle = (2\pi)^3 \delta_D^3(\vec{k} - \vec{k'}) P^\phi(k) \,. \tag{2.64}$$

$\delta_m$ and $\phi$ are related by the Poisson equation $k^2\phi = 4\pi G \bar{\rho}_m a^2 \delta_m$, which describes how matter sources a gravitational potential.

### Evolution of the Gravitational Potential

We can express the value of $\phi$ at the present epoch in terms of its primordial value as

$$\phi(\vec{k}, \eta_0) = \phi(\vec{k}, \eta_i) \times \{\text{transfer function}\} \times \{\text{growth function}\}, \tag{2.65}$$

where $\phi(\vec{k}, \eta_i)$ is the primordial potential, the transfer function describes the scale-dependent evolution of perturbations through horizon crossing and the transition from radiation domination to matter domination, and the growth factor describes the time evolution of perturbations.

### Primordial Power Spectrum

We assume that the initial matter power spectrum is a power law:

$$P^m_{initial}(k) = A_m k^{n_s}, \tag{2.66}$$

where the power spectrum is given in the synchronous gauge for convenience. We can constrain $A_m$ and $n_s$ using cosmic microwave background observations. Recent results have found $n_s = 0.9667 \pm 0.004$ (Planck Collaboration et al., 2015c). We expect $n_s \approx 1$, because if $n_s \ll 1$, there would be an excess of power on large scales (small k), contradicting the fact that the CMB is isotropic on large scales, and if $n_s \gg 1$ there would be an excess of power on smaller scales, resulting in more black holes than seem to be present in the universe. $n_s = 1$ is called a scale-invariant spectrum because it results in equal power in equal log intervals in k.

From the Poisson equation, we find

$$P^\phi_{initial}(k) = A_\phi k^{n_s - 4}, \tag{2.67}$$

so $P^\phi_{init}(k) \propto k^{-3}$ for a scale-invariant potential power spectrum.

### Transfer Function

The evolution of a particular mode depends on whether it enters the horizon before or after matter-radiation equality. For superhorizon modes ($k \ll k_H$), $\phi$ is a constant both in the matter and radiation dominated eras, but the value of $\phi$ drops by $10\%$ during the transition between

radiation domination and matter domination (Dodelson, 2003). For modes that enter the horizon during the radiation dominated era, the potential oscillates (because of oscillations from radiation pressure) and decays (because of the expansion of the universe). Matter perturbations grow logarithmically during radiation domination, as seen previously. After matter-radiation equality, the perturbations grow as $\delta \propto a$. Matching the two different solutions at equality gives us an expression for $\delta(\vec{k}, \eta)$. On small scales, after matter radiation equality, we can use the Poisson equation to show that $k^2\phi \propto \delta_m \propto \log(k/k_{eq})$.

We define the transfer function to be

$$T(k) = \frac{\phi(k, a_*)}{\phi(k_{large-scale}, a_*)}\,, \tag{2.68}$$

where $a_*$ is chosen long enough after matter-radiation equality that $\phi$ is constant again, and soon enough after matter-radiation equality that curvature and dark energy effects would not affect the perturbations.

We find (Dodelson, 2003)

$$T(k) = \begin{cases} 1 & k \ll k_{eq} \\ 12(\frac{k}{k_{eq}})^{-2} \log \frac{k}{8k_{eq}} & k \gg k_{eq} \end{cases} \tag{2.69}$$

**Growth Function**

The growth factor, denoted $D(a)$, gives the (scale-independent) time evolution of perturbations. We have seen that in matter-dominated times, $\delta_m(a) \propto a$, and so in a matter-dominated universe $D(a) \propto a$. The presence of curvature or dark energy would modify the growth factor, for example dark energy increases the expansion rate of the universe and therefore suppresses structure formation. The growth factor is given by (Dodelson, 2003)

$$D(a) = \frac{5\Omega_{m,0}H_0^2}{2} H(a) \int_0^a da'[a'H(a')]^{-3}. \tag{2.70}$$

### Final Power Spectrum

After being modified by the scale-dependent transfer function and the time-dependent growth factor, the final gravitational potential is given by

$$\phi(\vec{k}, \eta_0) = \frac{9}{10}\phi(\vec{k}, \eta_i) \times T(k) \times \frac{D(a)}{a}\,. \tag{2.71}$$

The power spectrum for the gravitational potential is

$$P^{\phi}(k) = \langle|\phi(k, a_0)|^2\rangle = \left(\frac{9}{10}\right)^2 P^{\phi}_{init}(k) T^2(k) \left(\frac{D(a)}{a}\right)^2, \tag{2.72}$$

and using Poisson's equation, we can find a similar expression for the density perturbation power spectrum in the synchronous gauge:

$$P^{m}(k) = \langle|\delta_m(k, a_0)|^2\rangle = \frac{9A_{\phi}}{25\Omega^2_{m,0}H_0^4} k^{n_s} T^2(k) D^2(a_0)\,. \tag{2.73}$$

For small $k$ (large scales) $P^m \propto k$ because these modes only dropped by $10\%$ across matter-radiation equality. For large k (small scales) the power is attenuated ($P^m \propto k^{-3}$), because these fluctuations entered the horizon before matter-radiation equality and their growth was suppressed in comparison to large-scale $k$ modes.

## 2.3 Inflation

We have discussed the homogeneity and isotropy of the universe on very large scales, as well as the formation of structure that grew from the small 'seed' perturbations present in the early universe, but we have not yet considered what caused the universe to be so smooth, or how the initial perturbations were sourced. The theory of inflation, which posits an early period of exponential expansion, provides answers to both of these questions (Guth, 1981; Guth and Weinberg, 1983).

### The Horizon Problem

The CMB has been measured to be isotropic to one part in $10^5$ in all directions on the sky (Smoot et al., 1992). If we consider a Big Bang singularity at $t = 0$ followed by periods of radiation

domination and then matter domination as described earlier, then the comoving horizon when the CMB was produced at time $t_{LS}$ (the furthest that light could have travelled by last scattering) would be finite, and there would be regions of the CMB that were not causally connected. These regions could not have had any communication, and would thus have no reason to be so uniform, leaving the isotropy of the CMB unexplained. This is a consequence of the horizon problem (Misner, 1969).

### The Particle Horizon and the Hubble Radius

We can rewrite the conformal time or comoving horizon $\eta$ as (Dodelson, 2003)

$$\eta = \int_0^a d\ln(a') \frac{1}{a'H(a')}. \tag{2.74}$$

Regions separated by comoving distances greater than $\eta$ have never been in causal contact. $\eta$ is sometimes called the particle horizon because particles separated by $\eta$ could never have communicated. The comoving Hubble radius is defined to be $\frac{1}{a'H(a')}$. Particles with separations greater than the Hubble radius are not in causal contact now.

Inflation solves the horizon problem. An early period of exponential expansion results in a decreasing Hubble radius, which means that regions that were in causal contact at early times became causally disconnected as the Hubble radius shrank. Thus inflation results in a particle horizon that is much larger than the Hubble radius: regions that were not causally connected when the CMB formed could have communicated early on, explaining the CMB's near uniformity.

### Initial Perturbations

We have argued that the large scale structure seen in the universe today grew from small primordial perturbations. Inflation provides an explanation for these perturbations: quantum fluctuations present before inflation would have been amplified as space expanded, resulting in slight overdensities and underdensities being present after inflation (Padmanabhan, 1993). It is these overdensities and underdensities that provided the seeds for the large scale structure we see today.

## 2.4 The Cosmic Microwave Background

At early times, when the universe was hot and dense, radiation and matter were coupled and photons were not able to travel freely through space. The universe was ionised because the photons were energetic enough to break apart any neutral atoms that formed. Photons were coupled to the free electrons by Compton scattering, and electrons were coupled to baryons by electromagnetic interactions, resulting in frequent interactions and a coupled photon-baryon fluid. About 380 000 years after the Big Bang, the universe had cooled sufficiently to allow neutral atoms to form: this period was called recombination. Photons did not interact strongly with the neutral atoms and became decoupled from baryons—the universe became transparent to light.

The cosmic microwave background (CMB) is radiation that was released from the photon-baryon fluid after recombination and pervades the universe. At the last scattering surface, the CMB photons had very high energies but their wavelengths stretched with the expansion of the universe and they are in the microwave bandwidth when they reach us. The CMB has a blackbody distribution with characteristic temperature $2.725\text{K}$ (Mather et al., 1992), and is distributed isotropically over the sky, with anisotropic fluctuations only appearing on the order of $\frac{\Delta T}{T} \sim 10^{-5}$ (Smoot et al., 1992). These anisotropies, although small, give us very important information about the fluctuations in the early universe.

### 2.4.1 Statistics of CMB Temperature Anisotropies

The anisotropies we see started off as temperature inhomogeneities on the surface of last scattering. We can write the temperature fluctuations in a direction $\hat{n}$ on the sky in terms of spherical harmonics $Y_{lm}$ as

$$\frac{\delta T(\hat{n})}{\bar{T}} = \frac{T(\hat{n}) - \bar{T}}{\bar{T}} = \sum_{l=0}^{\infty} \sum_{m=-l}^{l} a_{lm} Y_{lm}(\hat{n}). \tag{2.75}$$

In the flat sky approximation, which is valid when looking at a small part of the sky, this decomposition in terms of spherical harmonics becomes the two-dimensional Fourier decomposition. For now we will work with the full sky harmonic decomposition, but later on when we

are focusing on lensing we will use the flat sky approximation to simplify calculations.

The angular power spectrum $C_l^{TT}$ is given by given by

$$\langle a_{lm} a^*_{l'm'} \rangle = \delta^D_{ll'} \delta^D_{mm'} C_l^{TT} \,. \tag{2.76}$$

If the fluctuations are Gaussian as we expect, then the angular power spectrum contains all the available statistical information about the temperature fluctuations.

In the flat-sky limit, $l$ is the angular wavenumber corresponding to the angular wavelength $\theta = \frac{2\pi}{l}$. Large angular wavenumbers $l$ (or multipole moments in the full sky analysis) correspond to small angular scales and vice versa.

Inhomogeneities of the temperature field at recombination are seen by us as anisotropies because when we look at the sky in different directions, we see photons from different parts of the last scattering surface. The next section describes the physics of these anisotropies.

### 2.4.2 Physics of CMB Temperature Anisotropies

#### Monopole

The $l = 0$ monopole gives the mean temperature of the CMB, which is $T = 2.725 \pm 0.001$ K (Mather et al., 1992).

#### Dipole Anisotropy

The observed CMB has a dipole anisotropy of $3.346 \pm 0.017$ mK at the $l = 1$ spherical harmonic caused by a Doppler shift due to our motion (Bennett et al., 2003). We remove the dipole anisotropy from our maps to work in the rest frame of the CMB.

#### Acoustic Peaks

As discussed earlier, before recombination electrons interacted with photons via Thomson scattering and with baryons via Coulomb scattering, resulting in the photons and baryons acting as a tightly coupled photon-baryon fluid. Gravity tended to cause the photon-baryon fluid to fall into the gravitational potential wells of the early density perturbations of the universe (created by

clumps of cold dark matter), while pressure from the photons tended to oppose the compression of the photon-baryon fluid caused by gravity. This resulted in acoustic oscillations of the photon-baryon fluid (Hu, 2013). The CMB had a higher energy density and thus temperature in regions where the photon-baryon fluid was compressed, and lower temperature where the photon-baryon fluid was rarefied.

We can Fourier decompose the potential fluctuations, and treat each mode individually. The wavelength of the mode is related to the frequency of its oscillation by $\omega = kc_s$, where $c_s$ is the speed of sound of the medium. This makes sense intuitively because if the length scale of the potential fluctuations was smaller (i.e. k was larger), then it would have taken less time for the photon-baryon fluid to compress into the potential (i.e. $\omega$ would be be larger).

We can show (Dodelson, 2003) that the photon density perturbations satisfy the equation for a damped, driven harmonic oscillator

$$\ddot{\delta}_\gamma + \frac{\mathcal{H}R}{1+R}\dot{\delta}_\gamma + \omega^2\delta_\gamma = F(\Psi), \tag{2.77}$$

where $F(\Psi)$ is the forcing function which describes the effect of the gravitational potential, $R = \frac{3\bar{\rho}_b}{4\bar{\rho}_\gamma}$ is related to the ratio of baryons to photons and $\omega$ is the frequency from the previous paragraph.

At recombination, the electrons joined with nuclei to form neutral atoms. The photon-baryon fluid was no longer strongly coupled and acoustic oscillations ceased. There is a particular mode for which the photon baryon fluid would have compressed exactly once before recombination. This mode has wavenumber $k_1 = \frac{\pi}{\text{sound horizon}}$ where the sound horizon is the distance sound could have travelled by recombination. The mode with frequency $k_2 = 2k_1$ would have compressed once and rarefied once before recombination, and would also be at an extremum at recombination. All modes with wavenumbers $k_n = nk_1$ were at their extrema at recombination, and had greater temperature variations at their wavelengths than other modes. These modes became the peaks of the temperature power spectrum. The characteristic wavenumbers of the peaks become characteristic angular wavenumbers, because we see the spatial temperature variations as angular anisotropies.

Baryons added inertial mass to the oscillations, resulting in compression in the potential

wells being more marked than rarefaction. This enhanced the odd numbered peaks over the even numbered ones, as odd peaks correspond to the photon-baryon fluid being compressed at recombination and even numbered peaks correspond to rarefaction at recombination.

We can use the position and height of the peaks to constrain various cosmological parameters (Planck Collaboration et al., 2015c). The rich structure of the power spectrum allows us to detect the effects of gravitational lensing, which will be discussed in the next section.

#### Silk Damping

Recombination occurred over a short period of time, but was not instantaneous. During recombination, the photons executed a random walk as they interacted with the electrons. On scales smaller than the average distance travelled by photons during recombination (high $l$), the acoustic oscillations are damped because mixing between hot and cold regions occurred, smoothing out the temperature fluctuations (Silk, 1968).

The acoustic peaks and small-scale damping can be seen in the temperature power spectrum plotted in Figure (2.2).

### 2.4.3 CMB Polarisation

The CMB at last scattering had a nonzero quadrupole moment, which resulted in partial linear polarisation of the CMB through Thomson scattering. We can describe radiation completely by specifying the full set of Stokes parameters: the intensity $I$, circular polarisation $V$, and linear polarisations in different directions $Q$ and $U$. Thomson scattering does not produce circular polarisation, so we only need to use the parameters Q and U to describe the linear polarisation of the CMB. The polarisation has an amplitude of $P = \sqrt{Q^2 + U^2}$ and an angle $\alpha = \frac{1}{2}\tan^{-1}(\frac{U}{Q})$. $Q$ and $U$ are the natural quantities to use in map space, while in Fourier space the polarisation can more easily be separated into electric (E) and magnetic (B) modes. For E modes the polarisation is aligned with the principle polarisation axes (parallel or perpendicular to $\vec{k}$ for each Fourier mode) which corresponds to polarisation that is radial or tangential around temperature hotspots and coldspots. B mode polarisation makes a $45^\circ$ angle with the principle axes and the E modes

(Hu and White, 1997). We can relate the Stokes parameters to the $E$ and $B$ modes by (Hu, 2008)

$$E(\vec{l}) \pm iB(\vec{l}) = \int d^2\vec{x}(Q(\vec{x}) + iU(\vec{x}))e^{-i\vec{l}\cdot\vec{x}}e^{\mp 2i\phi_l} \,. \tag{2.78}$$

where we have used the flat sky approximation.

We define the polarisation and cross spectra as follows

$$\langle Y^*(\vec{l})Z(\vec{l'})\rangle = (2\pi)^2\delta_D^2(\vec{l} - \vec{l'})C_l^{YZ} \tag{2.79}$$

where $YZ = EE$, $BB$, $EB$, $TE$ or $TB$, and $T(\vec{l})$ is the two dimensional Fourier transform of $T(\vec{x})$ in the flat sky approximation. The E mode power spectrum is shown in Figure (2.2). Thomson scattering does not produce $B$ modes, so any $B$ modes in the primordial CMB are expected to be caused by gravitational waves from inflation.

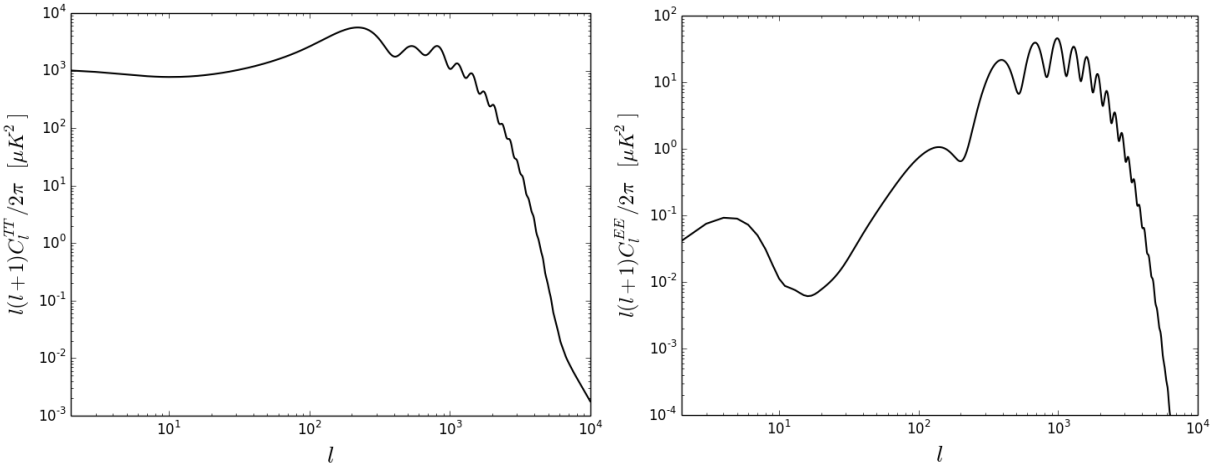


Figure 2.2: The unlensed CMB temperature (left) and E mode polarisation (right) angular power spectra.

## 2.5 Weak Gravitational Lensing of the Cosmic Microwave Background

The CMB does not just contain information about the very early universe: secondary anisotropies are imprinted on the CMB as the photons travel from the surface of last scattering to us. One

such secondary effect is gravitational lensing: the deflection of photons due to the matter that they pass. Gravitational lensing of the CMB can be used to probe the distribution of matter in our universe, of which dark matter forms a dominant part.

### 2.5.1 Deflection Angle

The deflection of light caused by the gravitational pull of matter is not a new concept: in one of the queries at the end of his book on *Opticks*, Newton suggests that light rays may be deflected by matter. Later, Newtonian gravity was used to calculate a predicted magnitude for such a deflection (von Soldner, 1804). The deflection angle predicted by Einstein's theory of general relativity is twice that predicted by the Newtonian theory of gravity, because of the effects of spacetime curvature.

Consider CMB radiation from the surface of last scattering, a comoving distance $\chi_*$ from the observer. If this light is deflected by an angle $\delta\beta$ by a gravitational potential $\Psi$ at a comoving distance $\chi$ from the observer, we want to know how the observed angle $\theta$ of the radiation will be affected, i.e. we want to find $\delta\theta$.

We can relate the angles using the spatial coordinate $f_K(\chi)$ to find (Lewis and Challinor, 2006)

$$\delta\theta_\chi = \frac{f_K(\chi_* - \chi)}{f_K(\chi_*)}\delta\beta\,. \tag{2.80}$$

In General Relativity, the deflection angle $\delta\beta$ can be shown to be $\delta\beta = -2\delta\chi\nabla_\perp\Psi$. Substituting this and integrating over the undeflected photon path (which is a good approximation in weak lensing, where deflection angles are assumed to be small) gives the total deflection angle to be

$$\vec{\alpha} = -2\int_0^{\chi_*} d\chi \frac{f_K(\chi_* - \chi)}{f_K(\chi_*)}\vec{\nabla}_\perp\Psi(\chi\hat{n}, \eta_0 - \chi)\,, \tag{2.81}$$

where $\chi\hat{n}$ gives the position and $\eta_0 - \chi$ the conformal time at which the potential $\Psi$ is evaluated. We take the universe to be flat, in which case $\frac{f_K(\chi_*-\chi)}{f_K(\chi_*)} = \frac{\chi_*-\chi}{\chi_*}$.

We can therefore describe the deflection angle in various directions across the sky by a vector field $\vec{\alpha}$. We have defined $\vec{\alpha}$ in such a way that the lensed CMB temperature $\tilde{T}$ in a direction $\hat{n}$ is

simply the unlensed temperature $T$ of the CMB in the direction $\hat{n}' = \hat{n} + \vec{\alpha}$, i.e.

$$\tilde{T}(\hat{n}) = T(\hat{n} + \vec{\alpha})\,. \tag{2.82}$$

The effect of lensing is illustrated in Figure (2.3). The top panel shows a map of the unlensed CMB on the left, and the lensed CMB on the right. We can see that the maps are very similar: lensing is a small effect. The difference between the two maps is correlated with the modulus of the deflection angle, shown in the bottom left and right panels respectively.

Lensing conserves the energy and thus the frequency of photons, so the lensed CMB has the same blackbody spectrum as if the photons had traveled to us undeflected. Lensing also conserves surface brightness. Although lensing may cause photons to converge, it also causes the apparent area the photons are coming from to appear larger. Similarly, if light diverges because of lensing, the area it seems to come from is smaller. This means that if the last scattering surface was isotropic, we would not be able to detect the effects of gravitional lensing. It is the rich structure of the anisotropies, described statistically by the CMB power spectrum, that allows us to detect the effects of lensing and reconstruct the lensing potential.

### 2.5.2 Lensing Potential

We can represent the effect of all of the potentials between $\chi_*$ and the observer as an effective lensing potential, which will be a scalar field across the sky. The deflection angle vector field $\vec{\alpha}$ will then be expressed as the gradient of this effective potential scalar field: $\vec{\alpha} = \vec{\nabla}_{\hat{n}}\psi = \vec{\nabla}\psi$.

Writing $\vec{\nabla}_\perp \Psi = \frac{\vec{\nabla}_{\hat{n}}\Psi}{\chi}$, our expression for $\vec{\alpha}$ in Equation (2.81) becomes (in a flat universe)

$$\vec{\alpha} = -2\int_0^{\chi_*} d\chi \frac{\chi_* - \chi}{\chi_*\chi}\vec{\nabla}_{\hat{n}}\Psi(\chi\hat{n}, \eta_0 - \chi)\,. \tag{2.83}$$

We define the lensing potential $\psi$ as follows:

$$\psi = -2\int_0^{\chi_*} d\chi \frac{\chi_* - \chi}{\chi_*\chi}\Psi(\chi\hat{n}, \eta_0 - \chi)\,. \tag{2.84}$$

The lensing potential is a projection of the three dimensional gravitational potential onto the two-dimensional sky, weighted according to how much a potential a comoving distance $\chi$ from us

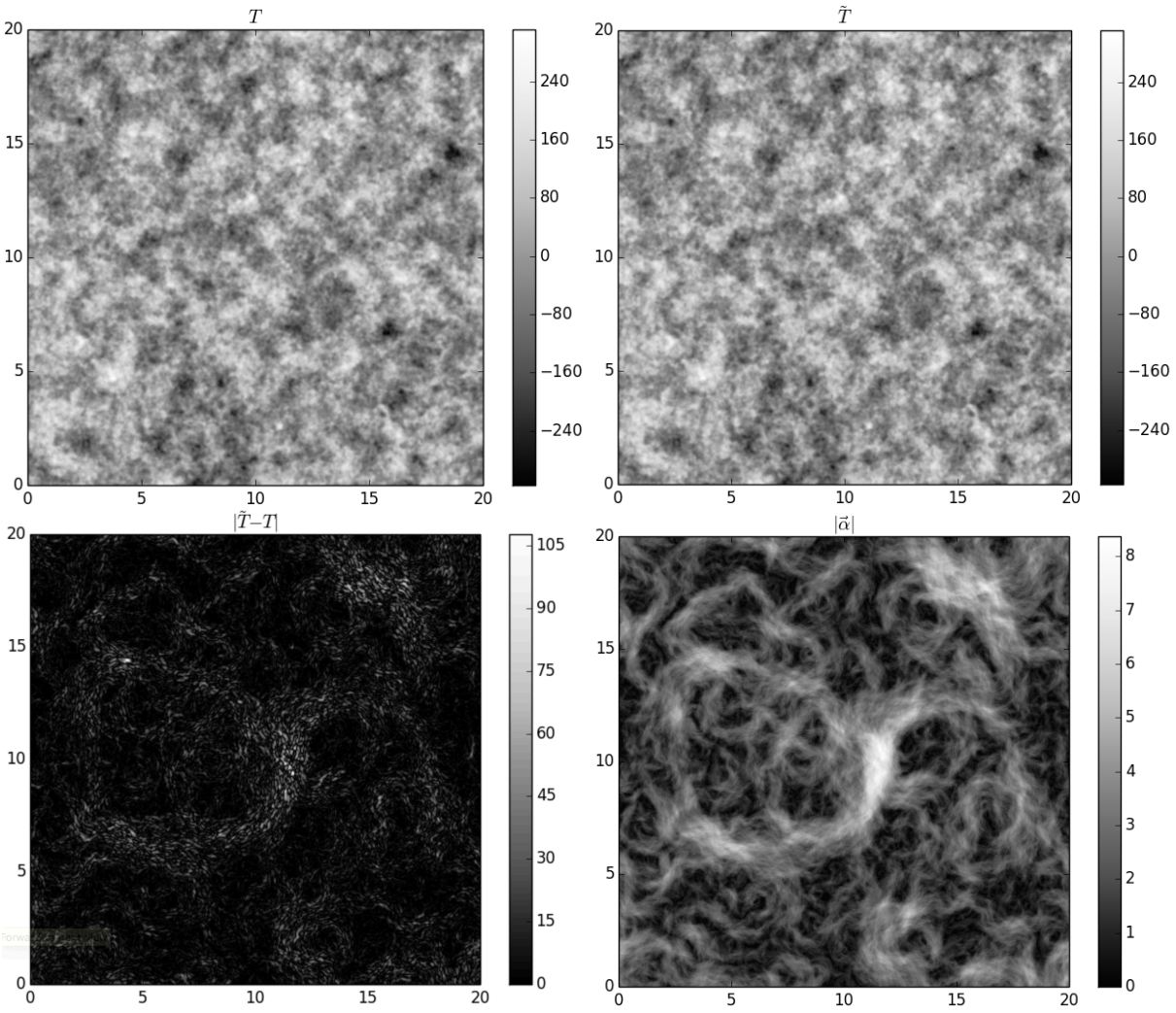


Figure 2.3: The top panel of this figure shows maps of the unlensed and lensed CMB temperature in units of $\mu$K (top left and right respectively). The bottom panel illustrates the difference between the unlensed and lensed temperature maps in units of $\mu$K (left) which is correlated with the magnitude of the deflection angle (right, shown in units of arcminutes). The horizontal and vertical axes are in units of degrees.

affects the deflection angle of a photon from a source at a distance $\chi_*$. The lensing kernel peaks halfway between us and the last scattering surface, so matter at $z \approx 1-2$ contributes the most to this weighted integral.

We treat the CMB as a single source plane at the last scattering surface $\chi = \chi_*$, neglecting the short time of recombination. We have also neglected the effects of reionisation and other late

time effects.

**Power Spectrum of the Lensing Potential**

We write the angular power spectrum of the lensing potential $\psi$ in terms of the three dimensional power spectrum of the gravitational potential $\Psi$ as follows

$$C_l^\psi = 16\pi \int \frac{dk}{k} \int_0^{\chi_*} d\chi \int_0^{\chi_*} d\chi' \frac{\chi_* - \chi}{\chi_* \chi} \frac{\chi_* - \chi'}{\chi_* \chi'} j_l(k\chi) j_l(k\chi') P^\Psi(k, \eta_0 - \chi, \eta_0 - \chi') \,. \quad (2.85)$$

The $\frac{\chi_* - \chi}{\chi_* \chi}$ factors weight the three dimensional potential along the line of sight from us to the source at $\chi_*$, according to how much a potential at $\chi$ contributes to the deflection angle. The $j_l$'s are spherical Bessel functions, which are used to project the three dimensional potentials onto the two dimensional sky.

We can simplify this expression in the Limber approximation, for which we assume that $P^\Psi(k)$ varies slowly in comparison to the Bessel functions. This is valid for high $l$. We use the identity

$$\int dk k^2 j_l(k\chi) j_l(k\chi') = \frac{\pi}{2\chi^2} \delta_D(\chi - \chi') \quad (2.86)$$

and integrate over the Bessel functions, which selects the scale $k = l/\chi$ and gives

$$C_l^\psi \approx \frac{8\pi}{l^3} \int_0^{\chi_*} \chi d\chi \left( \frac{\chi_* - \chi}{\chi_* \chi} \right)^2 P^\Psi(l/\chi, \eta_0 - \chi). \quad (2.87)$$

The power spectrum of $\vec{\alpha} = \nabla\psi$, i.e. $l(l+1)C^\psi(l)$ is shown in Figure (2.4). The RMS deflection angle (inferred from the height of the peak of the power spectrum) is around 2 arcminutes, and the deflections are coherent at scales of about 2 degrees (given by the position of the peak).

### 2.5.3 Magnification Matrix

The magnification matrix describes the distortion due to lensing. The matrix is given by the derivative of the deflection angle

$$A_{ij} = \delta_{ij} - \frac{\partial \alpha_i}{\partial x_j} = \begin{pmatrix} 1 - \kappa_0 - \gamma_+ & -\gamma_\times \\ -\gamma_\times & 1 - \kappa_0 + \gamma_+ \end{pmatrix}. \quad (2.88)$$

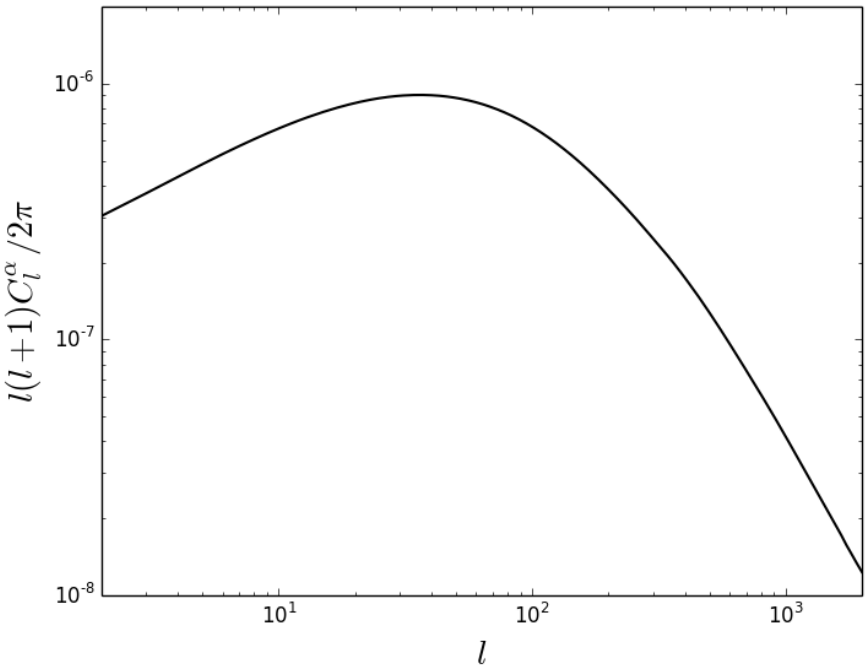


Figure 2.4: The power spectrum of the deflection angle, calculated with linear theory using CAMB: the Code for Anisotropies in the Microwave Background (Lewis and Challinor, 2011).

The convergence $\kappa_0 = \frac{1}{2}\vec{\nabla}\cdot\vec{\alpha} = \frac{1}{2}\nabla^2\psi$ determines the shape-preserving expansion or shrinking of a source due to lensing. The components of the shear, given by $\gamma_+ = \frac{1}{2}(\frac{\partial^2\psi}{\partial x_1^2} - \frac{\partial^2\psi}{\partial x_2^2})$ and $\gamma_\times = \frac{\partial^2\psi}{\partial x_1 \partial x_2}$ determine the distortion of the shape of the source along different axes due to the tidal gravitational field. In harmonic space, these relations become

$$\begin{aligned}
\kappa_0(\vec{L}) &= L^2\psi(\vec{L}) \\
\gamma_+(\vec{L}) &= (L_x^2 - L_y^2)\psi(\vec{L}) \\
\gamma_\times(\vec{L}) &= 2L_xL_y\psi(\vec{L}),
\end{aligned} \tag{2.89}$$

where $\vec{L} = (L_x, L_y)$ is the lensing wavevector in Fourier space in the flat sky approximation.

### 2.5.4 Lensed CMB Power Spectra

We will calculate the lensed CMB power spectrum in terms of the unlensed power spectrum by an expansion in the deflection angle. In order to simplify calculations, we will use the flat sky approximation and use our usual two dimensional Fourier expansion instead of expanding in spherical harmonics. This approximation is valid when we are dealing with relatively small parts of the sky. The Fourier expansions of the unlensed temperature and the lensing potential are

$$T(\vec{x}) = \int \frac{d^2\vec{l}}{(2\pi)^2} T(\vec{l})\, e^{i\vec{l}\cdot\vec{x}} \quad \text{and} \quad \psi(\vec{x}) = \int \frac{d^2\vec{l}}{(2\pi)^2} \psi(\vec{l})\, e^{i\vec{l}\cdot\vec{x}}, \tag{2.90}$$

where $T(\vec{l}) = \int d^2\vec{x} T(\vec{x}) e^{-i\vec{l}\cdot\vec{x}}$, and $\psi(\vec{l}) = \int d^2\vec{x}\psi(\vec{x}) e^{-i\vec{l}\cdot\vec{x}}$.

Now we define the power spectra for the temperature and lensing potential as

$$\langle T(\vec{l}) T^*(\vec{l'})\rangle = (2\pi)^2 \delta_D^2(\vec{l} - \vec{l'}) C_l^{TT} \text{ and } \langle \psi(\vec{l})\psi^*(\vec{l'})\rangle = (2\pi)^2 \delta_D^2(\vec{l} - \vec{l'}) C_l^{\psi}, \tag{2.91}$$

where the lensing potential power spectrum in the flat sky approximation will be equal to the lensing potential angular power spectrum on small scales.

We can expand the expression for the lensed temperature to first order as

$$\tilde{T}(\vec{x}) = T(\vec{x} + \vec{\alpha}) = T(\vec{x} + \vec{\nabla}\psi) \approx T(\vec{x}) + (\vec{\nabla}\psi)\cdot(\vec{\nabla} T(\vec{x})). \tag{2.92}$$

Taking the Fourier transform of $\tilde{T}(\vec{x})$ and using $\vec{\nabla}\psi(\vec{x}) = i\int \frac{d^2\vec{l}}{(2\pi)^2}(\vec{l})\,\psi(\vec{l})\, e^{i\vec{l}\cdot\vec{x}}$ and $\vec{\nabla} T(\vec{x}) = i\int \frac{d^2\vec{l}}{(2\pi)^2}(\vec{l})\, T(\vec{l})\, e^{i\vec{l}\cdot\vec{x}}$, we find that

$$\tilde{T}(\vec{l}) = T(\vec{l}) - \int d^2\vec{l}'\,(\vec{l}')(\vec{l} - \vec{l}')\psi(\vec{l} - \vec{l}')T(\vec{l}') = T(\vec{l}) - (\vec{l}\psi(\vec{l}))\circ(\vec{l}T(\vec{l}))\,, \tag{2.93}$$

where $\circ$ denotes convolution. We can do the same for $Q$ and $U$ polarisation and then rewrite the expression in terms of $E$ and $B$ mode polarisation. We use these expressions to find the lensed spectra for combinations of temperature and polarisation. The effects of lensing are to spread out the power at the peaks of the spectrum due to the convolution, and to transfer power to high $l$ modes (Lewis and Challinor, 2006). The effect of lensing on the temperature and $E$ mode power spectra are shown in Figure (2.5).

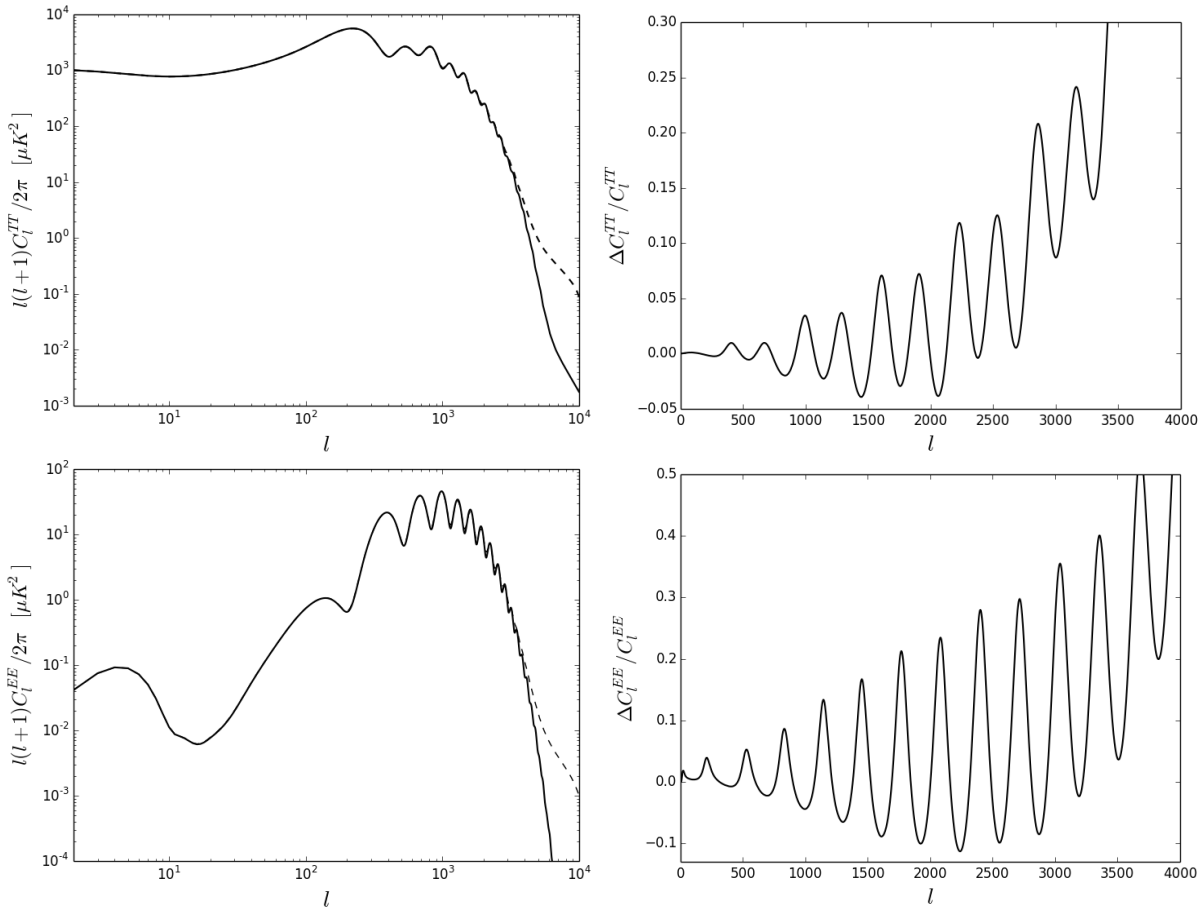


Figure 2.5: The left images show the unlensed (solid) and lensed (dashed) power spectra of the CMB temperature (top) and E mode polarisation (bottom). Lensing spreads out the peaks very slightly while transferring power to large $l$. The right panel shows the fractional change in the power spectrum caused by lensing. The plots were produced using CAMB (Lewis and Challinor, 2011).

If we take the expectation value over all values of the lensing potential $\psi$, which is statistically isotropic over the sky, and all realisations of the unlensed CMB $T(\vec{l})$, then to first order in the lensing potential power spectrum

$$\langle \tilde{T}(\vec{l})\tilde{T}^*(\vec{l'})\rangle = (2\pi)^2\delta_D^2(\vec{l}-\vec{l'})\tilde{C}_l^{TT}\,, \tag{2.94}$$

so harmonics with different $\vec{l}$ are uncorrelated. For a fixed lensing potential, however, different lensed CMB Fourier modes are correlated. Taking the expectation value over temperature and leaving the lensing potential fixed, we find the correlation between different lensed CMB $l$ modes to be proportional to the lensing potential (Hu and Okamoto, 2002; Lewis and Challinor, 2006):

$$\langle \tilde{T}(\vec{l})\tilde{T}^*(\vec{l}-\vec{L})\rangle_T = (2\pi)^2\delta_D^2(\vec{L})C_l^{TT} + \left((\vec{L}-\vec{l})\cdot\vec{L}C^{TT}_{|\vec{L}-\vec{l}|} + \vec{l}\cdot\vec{L}C_l^{TT}\right)\psi(\vec{L})\,. \tag{2.95}$$

We can use these 'off-diagonal' terms to reconstruct the lensing potential.

# CHAPTER 3

# Real Space Estimators for CMB Lensing Reconstruction

Gravitational lensing introduces non-Gaussianities into the lensed CMB (Bernardeau, 1997; Zaldarriaga, 2000; Hu, 2001a) and induces correlations between different harmonic modes, (see Equation (2.95)). Because these off-diagonal correlations are proportional to the lensing potential, quadratic estimators can be applied to the CMB temperature and polarisation in harmonic space to reconstruct the lensing potential (Zaldarriaga and Seljak, 1999; Seljak and Zaldarriaga, 1999; Hu and Okamoto, 2002; Okamoto and Hu, 2003; Cooray and Kesden, 2003). Alternative methods of reconstructing CMB lensing using likelihood-based methods have also been explored (Hirata and Seljak, 2003a,b).

In this chapter, we derive real space estimators that reconstruct the lensing convergence and shear directly from CMB temperature and polarisation maps. The real space approach can be helpful when analysing experimental data, as it makes use of local estimators which can easily cope with non uniform sky coverage and pixels that have been removed from CMB maps, whereas the ubiquitous harmonic space estimators (e.g. Hu and Okamoto, 2002) implicitly require uniform full sky coverage to work without adaptations. The estimators we present take the form of the convolution of a CMB temperature or polarisation map with a real space kernel

(limited in extent), multiplied by another CMB map.

This chapter extends previous work (Bucher et al., 2012), which focused on Planck-like temperature maps. As the sensitivity and resolution of CMB experiments continues to improve, the highest signal-to-noise lensing reconstructions will come from polarisation data (Hu and Okamoto, 2002), so we develop here similar real space estimators for polarisation in addition to temperature. We also discuss how features of the estimators depend on the experimental noise, comparing results from a Planck-like experiment (Planck Collaboration et al., 2015f) to next-generation experiments with better resolution and noise properties, such as the Advanced Atacama Cosmology Telescope Polarimeter (AdvACT) (Henderson et al., 2015). Ground-based experiments such as AdvACT do not have access to the full sky and so a local treatment is useful, especially if the survey strategy includes deep observations in relatively small patches of the sky.

## 3.1 Temperature and Polarisation Estimators

We develop estimators for the convergence ($\kappa_0$) and the two components of the shear field ($\gamma_+$ and $\gamma_\times$), which make up the deformation tensor (the part of the magnification matrix in Equation (2.88) that describes the distortion due to lensing):

$$\boldsymbol{\kappa} = \begin{pmatrix} \kappa_0 + \gamma_+ & \gamma_\times \\ \gamma_\times & \kappa_0 - \gamma_+ \end{pmatrix}, \tag{3.1}$$

where we have neglected a rotation in the matrix $\boldsymbol{\kappa}$. We develop estimators for these three quantities because $\psi$ and $\vec{\alpha}$ are both ambiguous: $\psi$ is indistinguishable from $\psi +$ (constant), and the vector field $\vec{\alpha}$ is indistinguishable from a translation (in the flat sky approximation) or a rotation (when we take sky curvature into account) of itself, since we only know the power spectrum and not the real-space temperature map of the unlensed CMB. Locally, the shear and convergence are unambiguous, and so we find estimators for these quantities.

We make use of what we will call the 'squeezed triangle approximation', in which the unlensed and lensed angular wavevectors $\vec{l}$ and $\vec{l}'$ have very similar magnitudes, which are large compared to that of the difference between them, $\vec{L} = \vec{l} - \vec{l}'$, as seen in Fig 3.1. This limit corresponds to studying the lensing fields ($\kappa_0$, $\gamma_+$ and $\gamma_\times$) on large scales (small $L$), and focusing on

small scale CMB anisotropies (large $l$). This is a reasonably good approximation because small scale anisotropies contribute most of the statistical information about lensing, and the lensing potential peaks at fairly low $L$ (see Figure (2.4)). However, the squeezed triangle approximation will result in a loss of power in our reconstruction for higher $L$ modes (small scale lensing fields). This effect is discussed in more detail in Section 3.2.

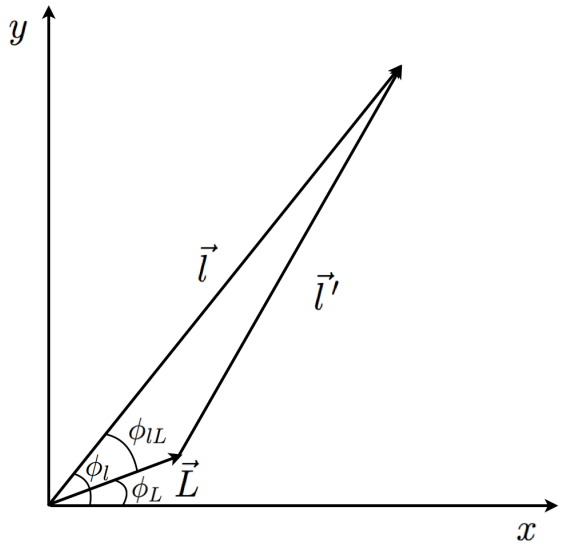


Figure 3.1: Coordinate system in Fourier space. The length of $\vec{L}$ has been exaggerated to make the diagram more readable.

We consider only weak lensing of the CMB, which is to say lensing in which the deflection angle is small. The lensing effect is thus perturbatively small, and we neglect all terms of second order or higher in the lensing fields.

### 3.1.1 Derivation from Lensed Power Spectra

We present a derivation of the real space temperature and polarisation estimators based on the approach in Bucher et al. (2012), in which we first take the squeezed triangle limit of the lensed power spectra to find the appropriate estimators in harmonic space, and then transform our expressions into real space. We recover the temperature estimator from Bucher et al. (2012) and develop original estimators for CMB polarisation.

**Lensed Fields in Terms of Unlensed Fields**

The effect of lensing is to remap photons from their primordial to their lensed positions on the sky. We can thus write the lensed temperature or polarisation in one direction on the sky (denoted by a tilde in the following) in terms of the unlensed temperature or polarisation in another direction on the sky: $\tilde{T}(\vec{x}') = T(\vec{x})$, $\tilde{Q}(\vec{x}') = Q(\vec{x})$ and $\tilde{U}(\vec{x}') = U(\vec{x})$, where we relate the positions in the unlensed and lensed sky by $\vec{x} = \boldsymbol{S}\vec{x}'$. Here $\boldsymbol{S} = e^{\boldsymbol{\kappa}}$ is the linear transformation describing the shifting of photons due to lensing in terms of the deformation tensor of Equation (3.1).

We note that the polarisation basis propagated along the perturbed photon path (in direction $\vec{x}'$ on the sky) is rotated slightly with respect to the basis propagated in the direction ($\vec{x}$). This rotation angle is less than $\sim 1$ arcminute provided we relate the two bases by a parallel transport along the spherical geodesic connecting the unlensed position to the lensed position (Lewis and Challinor, 2006), and so the effect of this rotation can be neglected.

We find the Fourier transform of the unlensed and lensed temperature maps in the flat sky approximation by integrating over areas $\mathcal{A}$ and $\mathcal{A}'$ respectively to obtain

$$T(\vec{l}) = \frac{1}{\sqrt{\mathcal{A}}} \int d^2\vec{x}\, T(\vec{x}) e^{-i\vec{l}\cdot\vec{x}} \tag{3.2}$$

$$\tilde{T}(\vec{l}) = \frac{1}{\sqrt{\mathcal{A}'}} \int d^2\vec{x}\,' \tilde{T}(\vec{x}\,') e^{-i\vec{l}\cdot\vec{x}'} \tag{3.3}$$

$$= \frac{1}{\sqrt{\det(J)\mathcal{A}}} \int d^2\vec{x}\, \det(J) T(\vec{x}) e^{-i\vec{l}\cdot(\boldsymbol{S}^{-1}\vec{x})} \tag{3.4}$$

$$= \frac{1}{\sqrt{\mathcal{A}}} \int d^2\vec{x}\, \det{}^{\frac{1}{2}}(J) T(\vec{x}) e^{-i(\boldsymbol{S}^{-1}\vec{l})\cdot\vec{x}} \tag{3.5}$$

$$= \det{}^{-\frac{1}{2}}(\boldsymbol{S}) T(\boldsymbol{S}^{-1}\vec{l}), \tag{3.6}$$

where $J$ is the Jacobian of the coordinate transformation $\boldsymbol{S}^{-1}$ and $\det J = \frac{1}{\det \boldsymbol{S}}$.

The Fourier transforms of the unlensed and lensed polarisation fields are

$$E(\vec{l}) \pm iB(\vec{l}) = \frac{1}{\sqrt{\mathcal{A}}} \int d^2\vec{x}\, (Q(\vec{x}) + iU(\vec{x}))\, e^{-i\vec{l}\cdot\vec{x}} e^{\mp 2i\phi_l} \tag{3.7}$$

$$\tilde{E}(\vec{l}) \pm i\tilde{B}(\vec{l}) = \frac{1}{\sqrt{\mathcal{A}'}} \int d^2\vec{x}\,' \left(\tilde{Q}(\vec{x}\,') + i\tilde{U}(\vec{x}\,')\right) e^{-i\vec{l}\cdot\vec{x}'} e^{\mp 2i\phi_l} \tag{3.8}$$

$$= \det{}^{-\frac{1}{2}}(\boldsymbol{S}) \frac{1}{\sqrt{\mathcal{A}}} \int d^2\vec{x} P(\vec{x}) e^{\mp 2i\phi_{l'}} e^{-i\vec{l}'\cdot\vec{x}} e^{\mp 2i(\phi_l - \phi_{l'})} \tag{3.9}$$

$$= \det{}^{-\frac{1}{2}}(\boldsymbol{S}) \left(E(\vec{l}') \pm iB(\vec{l}')\right) e^{\mp 2i(\phi_l - \phi_{l'})}, \tag{3.10}$$

where the lensed wavevector is related to the unlensed wavevector by $\vec{l}' = \boldsymbol{S}^{-1}\vec{l}$ and $\phi_{l'}$ is the polar angle of $\vec{l}'$.

Rewriting Equation (3.10) by expressing the angular factor as

$$e^{\mp 2i(\phi_l - \phi_{l'})} = 1 \mp 2i[\gamma_\times \cos(2\phi_l) - \gamma_+ \sin(2\phi_l)], \tag{3.11}$$

we find $\tilde{E}(\vec{l})$ and $\tilde{B}(\vec{l})$ by equating real and imaginary parts, obtaining

$$\tilde{E}(\vec{l}) = \det{}^{-\frac{1}{2}}(\boldsymbol{S})[E(\vec{l}') + 2(\gamma_\times \cos(2\phi_l) - \gamma_+ \sin(2\phi_l))B(\vec{l}')] \tag{3.12}$$

$$\tilde{B}(\vec{l}) = \det{}^{-\frac{1}{2}}(\boldsymbol{S})[B(\vec{l}') - 2(\gamma_\times \cos(2\phi_l) - \gamma_+ \sin(2\phi_l))E(\vec{l}')], \tag{3.13}$$

where $\vec{l}' = \boldsymbol{S}^{-1}\vec{l}$ as before. We Taylor expand $\boldsymbol{S}$ to obtain $\boldsymbol{S} = \boldsymbol{I} + \boldsymbol{\kappa}$. A calculation of the determinant keeping only first-order terms yields $\det^{-1}(\boldsymbol{S}) = 1 - 2\kappa_0$.

**Lensed Spectra in terms of Unlensed Spectra**

It is now straightforward to find the lensed angular power spectra and cross spectra of the CMB temperature and E- and B-mode polarisation in terms of the primordial spectra. The primordial B mode power spectrum $C_l^{BB}$ is expected to be a very small signal from gravitational waves, which can be neglected for our purposes, although detection of these inflationary gravitational waves would have great cosmological significance. The unlensed cross spectra $C_l^{EB}$ and $C_l^{TB}$ are zero by parity invariance.

For $XY = TT$, $EE$ and $TE$, we find

$$\begin{aligned}\tilde{C}_l^{XY} &= \det{}^{-1}(\boldsymbol{S}) C^{XY}_{|\boldsymbol{S}^{-1}\vec{l}|} \\ &= (1-2\kappa_0)\left(C_l^{XY} + \mathcal{K} l \frac{dC_l^{XY}}{dl}\right) \\ &= C_l^{XY} - \kappa_0\left(\frac{dC_l^{XY}}{d\ln l} + 2C_l^{XY}\right) - (\gamma_+\cos(2\phi_l) + \gamma_\times \sin(2\phi_l))\frac{dC_l^{XY}}{d\ln l}. \end{aligned} \tag{3.14}$$

where we have made use of the relation $l' \equiv |\boldsymbol{S}^{-1}\vec{l}| = l - \mathcal{K} l$ with

$$\mathcal{K} \equiv \frac{\vec{l}\cdot\boldsymbol{\kappa}\cdot\vec{l}}{l^2} = \kappa_0 + \gamma_+\cos(2\phi_l) + \gamma_\times \sin(2\phi_l). \tag{3.15}$$

We note that if the local spectral index $\beta \equiv \frac{d\ln C_l^{XY}}{d\ln l} = \frac{1}{C_l^{XY}}\frac{dC_l^{XY}}{d\ln l}$ takes on the value $\beta = -2$ then the power spectrum $C_l^{XY}$ is invariant under pure dilatations (for which only the convergence lensing field is nonzero). This is because $\beta = -2$ corresponds to a scale invariant two-dimensional angular power spectrum, and dilating such a field leaves it unchanged. If $\beta = 0$, corresponding to a white noise spectrum, then the power spectrum is invariant under pure shear transformations for which the convergence is zero (Bucher et al., 2012).

For $\tilde{C}_l^{TB}$ and $\tilde{C}_l^{EB}$, we have the following (where $Y$ is either $T$ or $E$):

$$\tilde{C}_l^{YB} = \langle \tilde{Y}^*(\vec{l})\tilde{B}(\vec{l})\rangle = -2C_l^{YE}\left[\gamma_\times\cos(2\phi_l) - \gamma_+\sin(2\phi_l)\right]. \tag{3.16}$$

In our approximation, the convergence has no effect on the lensed $TB$ and $EB$ power spectra, and thus we cannot use these spectra to reconstruct $\kappa_0$. This is because dilating E-mode polarisation with a large-scale convergence field that is approximately constant over the sky does not convert any of the E-mode polarisation pattern into B-modes, resulting in the lensed $TB$ and $EB$ spectra being zero. Shearing effects, however, mix polarisation E- and B-modes, and we can thus use the lensed $TB$ and $EB$ combinations to reconstruct the shear.

When we neglect primordial B modes and use our squeezed triangle approximation, we find $\tilde{C}_l^{BB} = 0$. In reality the lensed B polarisation power spectrum will be nonzero even if the unlensed spectrum is zero because some of the E-mode polarisation becomes B-mode polarisation under lensing. However, this effect is second order in $\gamma_+$ and $\gamma_\times$, and thus negligible in our linear and squeezed triangle approximations. We will therefore not work with estimators based on $\tilde{C}_l^{BB}$.

### Estimators

The squeezed triangle approximation, in which we assume a small lensing wavenumber $L$, corresponds to $\kappa_0$, $\gamma_+$ and $\gamma_\times$ varying on large scales across the sky. We use our expressions for the lensed power spectra to find estimators for $\kappa_0$, $\gamma_+$ and $\gamma_\times$ in a region of area $\mathcal{A}$ over which these quantities are constant. We can think of this region as being a (sufficiently small) pixel in the map. The estimator can then be translated to be applied at all pixels in the map.

An ansatz for an estimator for $\kappa_0$, based on the spectra for $XY = TT$, $EE$, or $TE$ from Equation (3.14) can be written as a weighted average of products of lensed maps:

$$\hat{\kappa}_0^{XY} = \frac{1}{N_{\hat{\kappa}_0}^{XY}} \mathcal{A} \int \frac{d^2\vec{l}}{(2\pi)^2} \left( \tilde{X}^*(\vec{l}) \tilde{Y}(\vec{l}) - C_l^{XY} \right) g_{\hat{\kappa}_0}^{XY}(l), \tag{3.17}$$

where $N_{\hat{\kappa}_0}^{XY}$ is the normalisation constant and $g_{\hat{\kappa}_0}^{XY}(\vec{l})$ is a weighting function. We subtract the unlensed power spectrum $C_l^{XY}$ from the observed one to isolate $\kappa_0$.

We choose the normalisation constant $N_{\hat{\kappa}_0}^{XY}$ to make the estimator unbiased, i.e. $\langle \hat{\kappa}_0^{XY} \rangle_{X,Y} = \kappa_0$, where $\langle\ \rangle_{X,Y}$ denotes an average over various realisations of the unlensed CMB temperature and polarisation maps, giving

$$N_{\hat{\kappa}_0}^{XY} = \mathcal{A} \int \frac{d^2\vec{l}}{(2\pi)^2} g_{\hat{\kappa}_0}^{XY}(l) \left( \frac{dC_l^{XY}}{d\ln l} + 2C_l^{XY} \right). \tag{3.18}$$

We set the weighting function $g_{\hat{\kappa}_0}^{XY}$ to minimise the variance of our estimator. For $XY = TT$ and $EE$, we have

$$g_{\hat{\kappa}_0}^{XY}(l) = \frac{1}{\mathcal{A}} \left( \frac{d\ln[C_l^{XY}]}{d\ln l} + 2 \right) \left( \frac{C_l^{XY}}{(C_l^{XY} + n^{XY}(l))^2} \right), \tag{3.19}$$

and for $TE$ we find that

$$g^{TE}(l) = \frac{1}{\mathcal{A}} \left( \frac{dC_l^{TE}}{d\ln l} + 2C_l^{TE} \right) \left( \frac{1}{\left(\tilde{C}_l^{TE}\right)^2 + \left(C_l^{TT} + n^{TT}(l)\right)\left(C_l^{EE} + n^{EE}(l)\right)} \right). \tag{3.20}$$

These expressions include the experimental noise $n^{XY}(l)$, which depends on the resolution and sensitivity of an experiment. The shapes of the weighting functions for Planck and AdvACT specifications are shown in Section 3.2. We use the expression $C_l^{XY} + n^{XY}(l)$ to approximate the

total measured power $\tilde{C}_l^{XY} + n^{XY}(l)$ because for most values of $l$ the difference between $C_l^{XY}$ and $\tilde{C}_l^{XY}$ is very small (as can be seen in Figure (2.5)), and for high $l$, where the difference is not negligible, the detector noise $n^{XY}(l)$ dominates the sum. The denominator comes from the four point correlation function when we calculate the variance.

We find estimators for $\gamma_+$ and $\gamma_\times$ by multiplying the observed power spectra by $\cos(2\phi_l)$ and $\sin(2\phi_l)$ to isolate the $\gamma_+$ and $\gamma_\times$ parts (since when we integrate, only the coefficients of $\cos^2(2\phi_l)$ or $\sin^2(2\phi_l)$ remain). We obtain

$$\begin{Bmatrix} \hat{\gamma}_+^{XY} \\ \hat{\gamma}_\times^{XY} \end{Bmatrix} = \frac{1}{N^{XY}_{\hat{\gamma}_+,\hat{\gamma}_\times}} \int \frac{d^2\vec{l}}{(2\pi)^2} g^{XY}_{\hat{\gamma}_+,\hat{\gamma}_\times}(l) \begin{Bmatrix} \cos(2\phi_l) \\ \sin(2\phi_l) \end{Bmatrix} \tilde{X}^*(\vec{l})\tilde{Y}(\vec{l}) \tag{3.21}$$

with the normalisation given by

$$N^{XY}_{\hat{\gamma}_+,\hat{\gamma}_\times} = \frac{\mathcal{A}}{2} \int \frac{d^2\vec{l}}{(2\pi)^2} \left( \frac{dC_l^{XY}}{d\ln l} \right) g^{XY}_{\hat{\gamma}_+,\hat{\gamma}_\times}(l), \tag{3.22}$$

and the weighting factor for $XY = TT$ and $EE$ given by

$$g^{XY}_{\hat{\gamma}_+,\hat{\gamma}_\times}(l) = \mathcal{A} \frac{C_l^{XY}}{(C_l^{XY} + n_l^{XY})^2} \left( \frac{d\ln[C_l^{XY}]}{d\ln l} \right), \tag{3.23}$$

while for $XY$=$TE$

$$g^{TE}_{\hat{\gamma}_+,\hat{\gamma}_\times}(l) = \left( \frac{1}{(\tilde{C}_l^{TE})^2 + (C_l^{TT} + n^{TT}(l))(C_l^{EE} + n^{EE}(l))} \right) \left( \frac{dC_l^{TE}}{d\ln l} \right). \tag{3.24}$$

We can also construct estimators for $\gamma_+$ and $\gamma_\times$ based on the spectra for $TB$ and $EB$. Using $Y$ to denote either $T$ or $E$, we obtain

$$\begin{Bmatrix} \hat{\gamma}_+^{YB} \\ \hat{\gamma}_\times^{YB} \end{Bmatrix} = \frac{1}{N^{YB}_{\hat{\gamma}_+,\hat{\gamma}_\times}} \int \frac{d^2\vec{l}}{(2\pi)^2} \left( \frac{C_l^{YE}}{(C_l^{YY} + n^{YY}(l))(n^{BB}(l))} \right) \begin{Bmatrix} \sin(2\phi_l) \\ \cos(2\phi_l) \end{Bmatrix} \tilde{Y}^*(\vec{l})\tilde{B}(\vec{l}), \tag{3.25}$$

where

$$N^{YB}_{\hat{\gamma}_+\hat{\gamma}_\times} = \int \frac{d^2\vec{l}}{(2\pi)^2} \frac{(C_l^{YE})^2}{(C_l^{YY} + n^{YY}(l))(n^{BB}(l))}. \tag{3.26}$$

These quadratic estimators for the lensing convergence and shear are unbiased and of minimum variance in the squeezed triangle approximation. They can be transformed into map space, giving the real space estimators that we implement.

**Real Space Implementation**

To obtain the real space convergence estimator, we substitute the expressions for the Fourier transform of the CMB maps $X$ and $Y$ (given in Equation (3.3) for the temperature) into the convergence estimator expression $\hat{\kappa}_0^{XY}$ given in Equation (3.17). Neglecting the unlensed component for now (we include it in the final expression in Equation (3.31)), we find for $XY = TT$, $EE$ or $TE$

$$\hat{\kappa}_0^{XY} = \frac{1}{N_{\hat{\kappa}_0}} \int d\vec{x} X(\vec{x}) \int d\vec{x}\,' Y(\vec{x}\,') \int \frac{d^2l}{(2\pi)^2} e^{i\vec{l}\cdot(\vec{x}-\vec{x}\,')} g^{XY}(l) \tag{3.27}$$

$$= \int d\vec{x} X(\vec{x}) \int d\vec{x}\,' Y(\vec{x}\,') K_{\hat{\kappa}_0}^{XY}(\vec{x}-\vec{x}\,') \tag{3.28}$$

$$= \int d\vec{x} X(\vec{x}) (K_{\hat{\kappa}_0}^{XY} \circ Y)(\vec{x})\,, \tag{3.29}$$

where $\circ$ denotes convolution and $K_{\hat{\kappa}_0}^{XY}$ is the inverse Fourier transform of the weighting function $g^{XY}(l)$ normalised by $N_{\hat{\kappa}_0}$:

$$K_{\hat{\kappa}_0}^{XY}(x) = \frac{1}{N_{\hat{\kappa}_0}} \int \frac{d^2l}{(2\pi)^2} e^{i\vec{l}\cdot\vec{x}} g^{XY}(l). \tag{3.30}$$

The kernel $K_{\hat{\kappa}_0}^{XY}(x)$ peaks at small angular scales, as will be shown in Section 3.2. This means that the central pixel contains the greatest signal, and integrating over other pixels makes the reconstruction noisier. Thus we keep only the reconstruction from the central pixel and translate it to different points on the map, giving our final expression for the estimator:

$$\hat{\kappa}_0^{XY}(\vec{x}) = X(\vec{x})(K_{\hat{\kappa}_0}^{XY} \circ Y)(\vec{x}) - \langle X(\vec{x})(K_{\hat{\kappa}_0}^{YY} \circ Y)(\vec{x}) \rangle_{\text{unlensed}}\,. \tag{3.31}$$

Similar expressions can be found for $\hat{\gamma}_+^{XY}(\vec{x})$ and $\hat{\gamma}_\times^{XY}(\vec{x})$. Setting

$$K_{\hat{\gamma}_+,\hat{\gamma}_\times}^{XY}(x) = \frac{1}{N_{\hat{\gamma}_+,\hat{\gamma}_\times}} \int_0^\infty \frac{dl}{(2\pi)} J_2(lx) g^{XY}(l), \tag{3.32}$$

where $J_2$ is the second order Bessel function of the first kind, and

$$K_{\begin{Bmatrix}\hat{\gamma}_+\\ \hat{\gamma}_\times\end{Bmatrix}}^{XY}(\vec{x}) = K_{\hat{\gamma}_+,\hat{\gamma}_\times}^{XY}(x) \begin{Bmatrix}\cos 2\theta(\vec{x})\\ \sin 2\theta(\vec{x})\end{Bmatrix}, \tag{3.33}$$

where $\theta(\vec{x})$ is a map of the polar angle of $\vec{x}$, we obtain

$$\begin{Bmatrix}\hat{\gamma}_+^{XY}(\vec{x})\\ \hat{\gamma}_\times^{XY}(\vec{x})\end{Bmatrix} = X(\vec{x})(K_{\begin{Bmatrix}\hat{\gamma}_+\\ \hat{\gamma}_\times\end{Bmatrix}}^{XY} \circ Y)(\vec{x}) \tag{3.34}$$

These expressions indicate how the real-space estimators are implemented to obtain maps of the lensing convergence and shear from temperature and polarisation maps.

### 3.1.2 Real Space Estimators as a limit of Harmonic Space Estimators

The real space estimators derived above are the small $L$ or large scale limit of the harmonic space estimators that are traditionally used for CMB lensing reconstruction (Seljak and Zaldarriaga, 1999; Hu and Okamoto, 2002; Cooray and Kesden, 2003). Harmonic space estimators make use of the fact that lensing induces correlations (proportional to the lensing potential) between previously uncorrelated CMB modes:

$$\langle X(\frac{\vec{L}}{2}-\vec{l})Y(\frac{\vec{L}}{2}+\vec{l})\rangle = f_{XY}(\vec{l},\vec{L})\ \phi(\vec{L}) \tag{3.35}$$

where $XY$=$TT$, $EE$ or $TE$ and

$$f_{XY}(\vec{l},\vec{L}) = \vec{L}\cdot\left(\frac{\vec{L}}{2}-\vec{l}\right)C^{XY}_{|\frac{\vec{L}}{2}-\vec{l}|} + \vec{L}\cdot\left(\frac{\vec{L}}{2}+\vec{l}\right)C^{XY}_{|\frac{\vec{L}}{2}+\vec{l}|} \tag{3.36}$$

Following Bucher et al. (2012), who presented a similar calculation for CMB temperature estimators, we have introduced a two-sided difference by using $\frac{\vec{L}}{2}\pm\vec{l}$ instead of $\vec{l}$ and $\vec{L}-\vec{l}$ so that we can take the low $L$ limit more easily.

The harmonic space estimator for the lensing potential is a weighted average of these off-diagonal modes:

$$\hat{\psi}^{XY}(\vec{L}) = \frac{1}{N^{XY}(\vec{L})}\int\frac{d^2\vec{l}}{(2\pi)^2}\tilde{X}(\frac{\vec{L}}{2}-\vec{l})\tilde{Y}^*(\frac{\vec{L}}{2}+\vec{l})g^{XY}(\vec{l},\vec{L})\,, \tag{3.37}$$

where $N^{XY}(\vec{L})$ is a normalisation factor to make the estimator unbiased, given by

$$N^{XY}(\vec{L}) = \int\frac{d^2\vec{l}}{(2\pi)^2}f_{XY}(\vec{l},\vec{L})g^{XY}(\vec{l},\vec{L}), \tag{3.38}$$

and $g^{XY}(\vec{l},\vec{L})$ is a weighting function to minimize the variance, which for $XY=TT$ and $EE$ is given by

$$g^{XY}(\vec{l},\vec{L}) = \frac{f_{XY}(\vec{l},\vec{L})}{\left(C^{XY}_{|\frac{\vec{L}}{2}-\vec{l}|}+n^{XY}(|\frac{\vec{L}}{2}-\vec{l}|)\right)\left(C^{XY}_{|\frac{\vec{L}}{2}+\vec{l}|}+n^{XY}(|\frac{\vec{L}}{2}+\vec{l}|)\right)}, \tag{3.39}$$

while for $TE$

$$g^{TE}(\vec{l},\vec{L}) = \frac{f_{TE}(\vec{l},\vec{L})\left(C_{l_1}^{TT,tot}C_{l_2}^{EE,tot} - C_{l_1}^{TE,tot}C_{l_2}^{TE,tot}\right)}{C_{l_1}^{TT,tot}C_{l_2}^{EE,tot}C_{l_1}^{EE,tot}C_{l_2}^{TT,tot} - \left(\left(C_{l_1}^{TE,tot}\right)\left(C_{l_2}^{TE,tot}\right)\right)^2} \tag{3.40}$$

where $l_1 = |\frac{\vec{L}}{2} - \vec{l}|$, $l_2 = |\frac{\vec{L}}{2} + \vec{l}|$ and $C_l^{XY,tot} = C_l^{XY} + n^{XY}(l)$.

We can simplify $f_{XY}$ in the squeezed triangle limit, where $L \ll l$ :

$$f_{XY}(\vec{l},\vec{L}) = \vec{L}\cdot\left(\frac{\vec{L}}{2} - \vec{l}\right)C^{XY}_{|\frac{\vec{L}}{2}-\vec{l}|} + \vec{L}\cdot\left(\frac{\vec{L}}{2} + \vec{l}\right)C^{XY}_{|\frac{\vec{L}}{2}+\vec{l}|} \tag{3.41}$$

$$\approx L^2 C_l^{XY} + \frac{(\vec{l}\cdot\vec{L})^2}{l}\frac{dC_l^{XY}}{dl} \tag{3.42}$$

$$\approx \frac{1}{2}L^2\left(\frac{1}{l^2}\frac{d(l^2C_l^{XY})}{d\ln(l)} + \left(\frac{2(\vec{l}\cdot\vec{L})^2}{L^2l^2} - 1\right)\frac{dC_l^{XY}}{d\ln(l)}\right) \tag{3.43}$$

$$\approx \frac{1}{2}L^2\left(\frac{1}{l^2}\frac{d(l^2C_l^{XY})}{d\ln(l)} + \cos(2\phi_{lL})\frac{dC_l^{XY}}{d\ln(l)}\right) \tag{3.44}$$

$$\approx \frac{1}{2}L^2\left(\frac{dC_l^{XY}}{d\ln(l)} + 2C_l^{XY} + \cos(2\phi_{lL})\frac{dC_l^{XY}}{d\ln(l)}\right) \tag{3.45}$$

where $\phi_{lL}$ is the angle between $\vec{L}$ and $\vec{l}$. In this limit, $C^{XY}_{|\frac{\vec{L}}{2}\pm\vec{l}|} + n^{XY}(|\frac{\vec{L}}{2}\pm\vec{l}|) \approx C_l^{XY} + n^{XY}(l)$, giving

$$g^{XY}(\vec{l},\vec{L}) = \frac{\frac{1}{2}L^2C_l^{XY}\left(\frac{d\ln(l^2C_l^{XY})}{d\ln(l)} + \cos(2\phi_{lL})\frac{d\ln(C_l^{XY})}{d\ln(l)}\right)}{\left(c_l^{XY} + n^{XY}(l)\right)^2} \tag{3.46}$$

for $XY = TT$ and $EE$, and

$$g^{TE}(\vec{l},\vec{L}) = \frac{\frac{1}{2}L^2\left(\left(\frac{dC_l^{TE}}{d\ln(l)} + 2C_l^{TE}\right) + \cos(2\phi_{lL})\frac{dC_l^{TE}}{d\ln(l)}\right)}{\left(C_l^{TT} + n^{TT}(l)\right)\left(C_l^{EE} + n^{EE}(l)\right) + \left(C_l^{TE} + n^{TE}(l)\right)^2}. \tag{3.47}$$

These approximate expressions for $g$ and for $f$ are carried through to the above expression for $N^{XY}$.

If we choose to align our $x$-axis and therefore our $l_x$-axis with the lensing wavevector $\vec{L}$, then $\phi_{lL} = \phi_l$ and we have

$$N^{XY}(\vec{L}) = \frac{1}{4}L^4(N^{XY}_{\hat{\kappa}_0} + N^{XY}_{\hat{\gamma}_+}) \tag{3.48}$$

and

$$g^{XY} = \frac{\mathcal{A}}{2}L^2\left(g^{XY}_{\hat{\kappa}_0} + g^{XY}_{\hat{\gamma}_+}\right), \tag{3.49}$$

where $N^{XY}_{\hat{\kappa}_0}$ and $g^{XY}_{\hat{\kappa}_0}$ are given in Equations (3.18) and (3.19), and $N^{XY}_{\hat{\gamma}_+}$ and $g^{XY}_{\hat{\gamma}_+}$ in Equations (3.22) and (3.23). This choice of axes corresponds to measuring the shear E and B Fourier modes, $\gamma_E$ and $\gamma_B$, where $\gamma_E(\vec{L})$ corresponds to $\gamma_+(\vec{L})$ in a frame aligned with the lensing wavevector and $\gamma_B(\vec{L})$ corresponds to $\gamma_\times(\vec{L})$ in such a frame. For any other choice of axes, the shear E and B modes can be obtained by rotating $\gamma(\vec{L}) = \gamma_+(\vec{L}) + i\gamma_\times(\vec{L})$ into the basis aligned with the wavenumber $\vec{L}$ to obtain

$$\gamma_E(\vec{L}) + i\gamma_B(\vec{L}) = e^{-2i\phi_L}(\gamma_+(\vec{L}) + i\gamma_\times(\vec{L})). \tag{3.50}$$

Substituting the expressions for $N^{XY}$ and $g^{XY}$ into Equation (3.37), we find that

$$L^2\hat{\psi}^{XY}(\vec{L}) \approx \frac{N^{XY}_{\hat{\kappa}_0}(\vec{L})}{N^{XY}_{\hat{\kappa}_0}(\vec{L}) + N^{XY}_{\hat{\gamma}_E}(\vec{L})} 2\hat{\kappa}_0 + \frac{N^{XY}_{\hat{\gamma}_E}(\vec{L})}{N^{XY}_{\hat{\kappa}_0}(\vec{L}) + N^{XY}_{\hat{\gamma}_E}(\vec{L})} 2\hat{\gamma}_E \tag{3.51}$$

where $\hat{\kappa}^{XY}_0$ and $\hat{\gamma}^{XY}_E$ are as defined in Equations (3.17) and (3.21), with the axes chosen as discussed above. We can see that the harmonic space estimator for $L^2\hat{\psi}^{XY}$ for $XY = TT$, $EE$ and $TE$ is the inverse variance weighted combination of the real space estimators for the convergence $\hat{\kappa}_0$ and the shear E mode $\hat{\gamma}_E$. This makes sense, because the expressions relating the convergence and shear plus component to the lensing potential both reduce to $L^2\psi(\vec{L})$ in Equations (2.89) if the $x$-axis is aligned with the lensing wavevector. The B mode component of the shear is forbidden in weak lensing, and is therefore not present. Thus our real space estimators for the $TT$, $EE$ and $TE$ spectra are simply the small L limits of the corresponding harmonic space estimators.

For $TB$ and $EB$, we have the following (where $Y$ is $T$ or $E$)

$$\langle Y(\frac{\vec{L}}{2} - \vec{l})B(\frac{\vec{L}}{2} + \vec{l})\rangle = f_{YB}(\vec{l}, \vec{L})\ \phi(\vec{L}) \tag{3.52}$$

where

$$f_{YB}(\vec{l}, \vec{L}) = \vec{L} \cdot \left(\frac{\vec{L}}{2} - \vec{l}\right) C^{YE}_{|\frac{\vec{L}}{2} - \vec{l}|} \sin\left(2\phi_{\frac{\vec{L}}{2}+\vec{l}, \frac{\vec{L}}{2}-\vec{l}}\right) \tag{3.53}$$

The harmonic space estimator for the lensing potential is given by

$$\hat{\psi}^{YB}(\vec{L}) = \frac{1}{N^{YB}(\vec{L})} \int \frac{d^2\vec{l}}{(2\pi)^2} \tilde{Y}(\frac{\vec{L}}{2} - \vec{l})\tilde{B}^*(\frac{\vec{L}}{2} + \vec{l}) g^{YB}(\vec{l}, \vec{L})\,, \tag{3.54}$$

where $N^{YB}(\vec{L})$ is a normalisation function and $g^{YB}(\vec{l},\vec{L})$ is a weighting function:

$$N^{YB}(\vec{L}) = \int \frac{d^2\vec{l}}{(2\pi)^2} f_{YB}(\vec{l},\vec{L}) g^{YB}(\vec{l},\vec{L}), \tag{3.55}$$

and

$$g^{YB}(\vec{l},\vec{L}) = \frac{f_{YB}(\vec{l},\vec{L})}{\left(C^{YY}_{|\frac{\vec{L}}{2}-\vec{l}|} + n^{YY}(|\frac{\vec{L}}{2}-\vec{l}|)\right) n^{BB}(|\frac{\vec{L}}{2}+\vec{l}|)}. \tag{3.56}$$

We can simplify $f_{YB}$ in the limit where $L \ll l$ (neglecting higher order terms in L):

$$f_{YB}(\vec{l},\vec{L}) \approx \left(\frac{L^2}{2} - \vec{l}\cdot\vec{L}\right) C_l^{YE} \sin\left(2\phi_{\frac{\vec{L}}{2}+\vec{l},\frac{\vec{L}}{2}-\vec{l}}\right) \tag{3.57}$$

$$\approx -\vec{l}\cdot\vec{L} C_l^{YE} \sin\left(2\phi_{\frac{\vec{L}}{2}+\vec{l},\frac{\vec{L}}{2}-\vec{l}}\right) \tag{3.58}$$

$$\approx -Ll\frac{L}{l} 2\cos(\phi_{lL})\sin(\phi_{lL}) C_l^{YE} \tag{3.59}$$

$$\approx L^2 \sin(2\phi_{lL}) C_l^{YE} \tag{3.60}$$

where $\phi_{lL}$ is the angle between $\vec{L}$ and $\vec{l}$.

Also, $C^{YY}_{|\frac{\vec{L}}{2}-\vec{l}|} + n^{YY}(|\frac{\vec{L}}{2}-\vec{l}|) \approx C_l^{YY} + n^{YY}(l)$ and $n^{BB}(|\frac{\vec{L}}{2}+\vec{l}|) \approx n^{BB}(l)$, giving

$$L^2\hat{\psi}^{YB}(\vec{L}) \approx \hat{\gamma}_E^{YB}, \tag{3.61}$$

where $\hat{\gamma}_E^{YB}$ corresponds in our choice of coordinates to $\gamma_+^{YB}$ as defined in Equation (3.25).

Again we see that the $\hat{\gamma}_B$ component is not present, as expected for weak lensing. The convergence is also missing for the $TB$ and $EB$ estimators as the large scale convergence fields in our approximation do not generate B modes.

### 3.1.3 Derivation from Lensed Correlation Functions

The estimators we have derived so far, based on E and B polarisation maps, are the real-space analogues of the quadratic polarisation lensing estimators in harmonic space (Hu and Okamoto, 2002) in the squeezed triangle approximation. However, we have not yet created truly local polarisation lensing estimators, because E and B modes themselves are inherently non-local: they depend on the alignment of the polarisation with nonlocal Fourier wave vectors.

In this section, we present an alternative derivation that deals directly with CMB correlation functions in real space, and results in lensing estimators that are applied to temperature and Q and U polarisation maps. Q and U polarisations are what we measure experimentally, and so we will obtain estimators that can be applied to maps without needing to apply nonlocal treatments to construct the polarisation E and B mode maps. We note that for simulated maps, there is no issue with using E and B mode polarisation as we can create maps with periodic boundary conditions that can easily be Fourier transformed, and so we will show results that make use of the E and B estimators defined above. However for experimental data the estimators defined for Q and U maps will be the most straightforward to apply.

We consider the correlation functions

$$\begin{aligned}
\xi_T(r) &= \langle T(\vec{x})T(\vec{x}-\vec{r})\rangle \\
\xi_-(r) &= \langle P_r(\vec{x})P_r^*(\vec{x}-\vec{r})\rangle = \langle P(\vec{x})P^*(\vec{x}-\vec{r})\rangle \\
\xi_+(r) &= \langle P_r(\vec{x})P_r(\vec{x}-\vec{r})\rangle = \langle e^{-4i\phi_r}P(\vec{x})P(\vec{x}-\vec{r})\rangle \\
\xi_\times(r) &= \langle P_r(\vec{x})T(\vec{x}-\vec{r})\rangle = \langle e^{-2i\phi_r}P(\vec{x})T(\vec{x}-\vec{r})\rangle
\end{aligned} \tag{3.62}$$

where $P(\vec{x}) = Q(\vec{x}) + iU(\vec{x})$ and $P_r(\vec{x}) = e^{-2i\phi_r}P(\vec{x})$ is the polarisation field expressed in the physically relevant basis defined by $\vec{r}$, with $\phi_r$ the polar angle of $\vec{r}$ (Lewis and Challinor, 2006). Thus $Q_r$ describes polarisation along the direction $\hat{r}$ ($Q_r$ positive) or perpendicular to $\hat{r}$ ($Q_r$ negative), and $U_r$ describes polarisation at a $45^\circ$ angle to these directions.

**Lensed Correlation Functions**

We can relate the lensed CMB temperature map $\tilde{T}(\vec{x})$ to the unlensed map $T(\vec{x})$ by

$$\tilde{T}(\vec{x}) = T(e^{\boldsymbol{\kappa}}\vec{x}) \approx T(\vec{x}+\boldsymbol{\kappa}\vec{x}) \approx T(\vec{x}) + \vec{\nabla}T(\vec{x})\cdot\boldsymbol{\kappa}\vec{x}, \tag{3.63}$$

where $\boldsymbol{\kappa}$ is the deformation tensor defined in Equation (3.1), provided the lensing effect is small. We can thus relate the lensed and unlensed temperature correlation functions:

$$\begin{aligned}
\tilde{\xi}_T(\vec{r}) &= < \tilde{T}(\vec{x})\tilde{T}(\vec{x}-\vec{r}) >_{\vec{x}} \\
&= < \tilde{T}(\vec{x}+\vec{r})\tilde{T}(\vec{x}) >_{\vec{x}} \\
&= \xi_T(\vec{r}) + < (\vec{\nabla}T(\vec{x}+\vec{r})\cdot\kappa(\vec{x}+\vec{r}))T(\vec{x}) >_{\vec{x}} + < (\vec{\nabla}T(\vec{x})\cdot\kappa\vec{x})T(\vec{x}+\vec{r}) >_{\vec{x}} \\
&= \xi_T(\vec{r}) + < (\vec{\nabla}T(\vec{x}+\vec{r})\cdot\kappa\vec{x})T(\vec{x}) >_{\vec{x}} + < (\vec{\nabla}T(\vec{x})\cdot\kappa\vec{x})T(\vec{x}+\vec{r}) >_{\vec{x}} + < (\vec{\nabla}T(\vec{x}+\vec{r})\cdot\kappa\vec{r})T(\vec{x}) >_{\vec{x}} \\
&= \xi_T(\vec{r}) + < (\vec{\nabla}T(\vec{x}+\vec{r})\cdot\kappa\vec{r})T(\vec{x}) >_{\vec{x}},
\end{aligned} \tag{3.64}$$

where the two middle terms in the second line from the bottom vary sinusoidally with the polar angle of $\vec{x}$, and thus average to zero when we take the expectation value. We find

$$< (\vec{\nabla}T(\vec{x}+\vec{r})\cdot\kappa\vec{r})T(\vec{x}) >_{\vec{x}} = r\frac{\partial\xi_T}{\partial r}(\kappa_0+\gamma_{+,r}) + \frac{\partial\xi_T}{\partial\phi}\gamma_{\times,r}\,, \tag{3.65}$$

where

$$\gamma_{+,r} + i\gamma_{\times,r} = (\gamma_+ + i\gamma_\times)e^{-2i\phi} \tag{3.66}$$

is the shear in the basis defined by the $\vec{r}$ direction. The isotropy of the unlensed CMB means that $\frac{\partial\xi_T}{\partial\phi} = 0$, so we find

$$< (\vec{\nabla}T(\vec{x}+\vec{r})\cdot\kappa\vec{r})T(\vec{x}) >_{\vec{x}} = r\frac{\partial\xi_T}{\partial r}(\kappa_0 + \gamma_+\cos 2\phi_r + \gamma_\times \sin 2\phi_r). \tag{3.67}$$

Substituting this into the expression for the lensed correlation function in Equation (3.64), we obtain our final expression relating the lensed correlation function to the unlensed correlation function:

$$\tilde{\xi}_T(\vec{r}) = \xi_T(\vec{r}) + \frac{\partial\xi_T}{\partial\ln r}(\kappa_0 + \gamma_+\cos 2\phi_r + \gamma_\times\sin 2\phi_r). \tag{3.68}$$

A similar calculation for $\tilde{\xi}_+(\vec{r})$, $\tilde{\xi}_-(\vec{r})$ and $\tilde{\xi}_\times(\vec{r})$ shows that the same relation holds for all of the correlation functions. The lensed correlation functions can be thus expressed in terms of the unlensed correlation functions defined in Equations (3.62) and the lensing fields that make up the deformation tensor, in a region in which $\kappa_0$, $\gamma_+$ and $\gamma_\times$ are constant and small, as

$$\tilde{\xi}(\vec{r}) = \xi(r) + \frac{d\xi}{d\ln(r)}\left(\kappa_0 + \gamma_+\cos(2\phi_r) + \gamma_\times\sin(2\phi_r)\right), \tag{3.69}$$

where $\xi = \xi_T, \xi_+, \xi_-$ or $\xi_\times$.

We can therefore construct estimators for the convergence and shear in this region as follows, where we have a different version of each estimator for each of the different correlation functions:

$$\begin{aligned}
\hat{\kappa_0} &= \int d^2\vec{r} K_{\kappa_0}(r)\tilde{\xi}(\vec{r}) \\
\hat{\gamma}_+ &= \int d^2\vec{r} K_\gamma(r)\cos(2\phi_r)\tilde{\xi}(\vec{r}) = \int d^2\vec{r} K_{\gamma_+}(\vec{r})\tilde{\xi}(\vec{r}) \\
\hat{\gamma}_\times &= \int d^2\vec{r} K_\gamma(r)\sin(2\phi_r)\tilde{\xi}(\vec{r}) = \int d^2\vec{r} K_{\gamma_\times}(\vec{r})\tilde{\xi}(\vec{r}),
\end{aligned} \tag{3.70}$$

where $K_{\gamma_+}(\vec{r}) \equiv K_\gamma(r)\cos(2\phi_r)$, $K_{\gamma_\times}(\vec{r}) \equiv K_\gamma(r)\sin(2\phi_r)$. The lensing kernels $K$ weight and normalise the estimators. We find the lensing kernels by relating the estimators in Equation (3.70), and thus their kernels, to the real-space estimators obtained by starting with the lensing distortion in harmonic space in Section 3.1.1. Expressions for the lensing kernels are calculated below, and the final expressions appear in Tables (3.1) and (3.2).

**Temperature Estimator**

Taking $\xi_T$, we find

$$\begin{aligned}
\hat{\kappa_0}^T &= \int d^2\vec{r} K_{\kappa_0^T}(r)\tilde{\xi}_T(\vec{r}) \\
&= \int d^2\vec{r} K_{\kappa_0^T}(r) \int d^2\vec{x} T(\vec{x})T(\vec{x}-\vec{r}) \\
&= \int d^2\vec{x} T(\vec{x}) \int d^2\vec{r} K_{\kappa_0^T}(r) T(\vec{x}-\vec{r}) \\
&= \int d^2\vec{x} T(\vec{x})(K_{\kappa_0^T} \circ T)(\vec{x}).
\end{aligned} \tag{3.71}$$

This takes the same form as the estimator in Equation (3.29) which we derived in Section 3.1.1, and so $K_{\kappa_0^T} = K_{\kappa_0}^{TT}$ calculated above. The kernel peaks at small angular scales and drops off quickly, so the cleanest reconstruction is obtained by only keeping the central pixel in the

integrand. The estimator can be translated to different points of the map, giving

$$\hat{\kappa_0}^T(\vec{x}) = T(\vec{x})(K_{\kappa_0^T} \circ T)(\vec{x}), \tag{3.72}$$

where $K_{\kappa_0^T} = K_{\kappa_0}^{TT}$ as defined in Equation (3.30).

### $\xi_+$ Estimator

For $\xi_+$ we find

$$\begin{aligned}
\hat{\kappa_0} &= \int d^2\vec{r} K(\vec{r}) \int d^2\vec{x} \tilde{P}^*(\vec{x})\tilde{P}(\vec{x}-\vec{r}) \\
&= \int d^2\vec{r} K(\vec{r}) \int d^2\vec{x} \left(\tilde{Q}(\vec{x})\tilde{Q}(\vec{x}-\vec{r}) + \tilde{U}(\vec{x})\tilde{U}(\vec{x}-\vec{r})\right) \\
&= \int d^2\vec{x} \left(\tilde{Q}(\vec{x})(K \circ \tilde{Q})(\vec{x}) + \tilde{U}(\vec{x})(K \circ \tilde{U})(\vec{x})\right).
\end{aligned} \tag{3.73}$$

Again, we can translate this estimator to different pixels on the map, giving

$$\hat{\kappa_0}(\vec{x}) = \tilde{Q}(\vec{x})(K \circ \tilde{Q})(\vec{x}) + \tilde{U}(\vec{x})(K \circ \tilde{U})(\vec{x}). \tag{3.74}$$

We obtain the kernel by taking the Fourier transform of our estimator and comparing it to the expressions for the estimators in harmonic space in Section 3.1.1. We find

$$\begin{aligned}
\hat{\kappa_0}(\vec{l}) &= \tilde{Q}(\vec{l}) \circ (K(\vec{l})\tilde{Q}(\vec{l})) + \tilde{U}(\vec{l}) \circ (K(\vec{l})\tilde{U}(\vec{l})) \\
&= \int \frac{d^2\vec{l'}}{(2\pi)^2} K(\vec{l'}) \left(\tilde{Q}(\vec{l}-\vec{l'})\tilde{Q}(\vec{l'}) + \tilde{U}(\vec{l}-\vec{l'})\tilde{U}(\vec{l'})\right) \\
&= \int \frac{d^2\vec{l'}}{(2\pi)^2} K(\vec{l'}) \left(\tilde{Q}^*(\vec{l'}-\vec{l})\tilde{Q}(\vec{l'}) + \tilde{U}^*(\vec{l'}-\vec{l})\tilde{U}(\vec{l'})\right).
\end{aligned} \tag{3.75}$$

Taking the expectation value gives

$$< \hat{\kappa_0}(\vec{l}) >_{CMB} = \int \frac{d^2\vec{l'}}{(2\pi)^2} K(\vec{l'}) \left(\tilde{C}_{\vec{l'}}^{QQ} + \tilde{C}_{\vec{l'}}^{UU}\right). \tag{3.76}$$

We can rewrite this in term of $E$ and $B$ modes using (Lewis and Challinor, 2006)

$$\begin{aligned}\tilde{C}^{QQ}_{\vec{l}} + \tilde{C}^{UU}_{\vec{l}} &= \int d^2\vec{r}\xi_+(\vec{r})e^{-i\vec{l}\cdot\vec{r}} \\ &= \tilde{C}^{EE}_{\vec{l}} + \tilde{C}^{BB}_{\vec{l}} \\ &= \tilde{C}^{EE}_{\vec{l}}, \end{aligned} \tag{3.77}$$

where the last equality holds because in our approximation $\tilde{C}^{BB}(\vec{l}) = 0$.

Our estimator thus simplifies to

$$< \hat{\kappa}_0(\vec{l}) >_{CMB} = \int \frac{d^2\vec{l'}}{(2\pi)^2} K(\vec{l'})\tilde{C}^{EE}_{\vec{l'}}, \tag{3.78}$$

which is what we find if we take the expectation value of the $EE$ estimator in Equation (3.17). Thus $K(\vec{l})$ for the $\xi_+$ estimator is the same kernel as for our existing $EE$ estimator, given in Equation (3.30).

We can make similar comparisons for the other estimators, obtaining their kernels from those defined in Section 3.1.1. Tables (3.1) and (3.2) show the forms taken by the convergence and shear plus estimators respectively, as well as the expressions for the relevant kernels. The estimators for $\gamma_\times$ are the same as those for $\gamma_+$ but with the factors of $\cos$ replaced by $\sin$ and vice versa.

Table 3.1: Convergence estimators from real space correlation functions

| Estimator | Form | Kernel |
|---|---|---|
| $\hat{\kappa}^T_0$ | $\tilde{T}(\vec{x})(K_{\kappa^T_0} \circ \tilde{T})(\vec{x})$ | $K_{\kappa^T_0} = \frac{1}{2\pi N^{TT}_{\kappa_0}} \int_0^\infty l dl J_0(lx) g^{TT}_{\kappa_0}(l)$ |
| $\hat{\kappa}^+_0$ | $\tilde{Q}(\vec{x})(K_{\kappa^+_0} \circ \tilde{Q})(\vec{x}) + \tilde{U}(\vec{x})(K_{\kappa^+_0} \circ \tilde{U})(\vec{x})$ | $K_{\kappa^+_0} = \frac{1}{2\pi N^{EE}_{\kappa_0}} \int_0^\infty l dl J_0(lx) g^{EE}_{\kappa_0}(l)$ |
| $\hat{\kappa}^-_0$ | $\tilde{Q}(\vec{x})(K_{\kappa^-_0} \circ \tilde{Q})(\vec{x}) - \tilde{U}(\vec{x})(K_{\kappa^-_0} \circ \tilde{U})(\vec{x})$ | $K_{\kappa^-_0} = \frac{1}{\pi N^{EE}_{\kappa_0}} \int_0^\infty l dl J_0(lx) g^{EE}_{\kappa_0}(l)$ |
| $\hat{\kappa}^\times_0$ | $\tilde{Q}(\vec{x})(K^Q_{\kappa^\times_0} \circ \tilde{T})(\vec{x}) + \tilde{U}(\vec{x})(K^U_{\kappa^\times_0} \circ \tilde{T})(\vec{x})$ | $K^Q_{\kappa^\times_0} = \left(\frac{1}{2\pi N^{TE}_{\kappa_0}} \int_0^\infty l dl J_0(lx) g^{TE}_{\kappa_0}(l)\right) \cos 2\phi_r$ |
| | | $K^U_{\kappa^\times_0} = \left(\frac{1}{2\pi N^{TE}_{\kappa_0}} \int_0^\infty l dl J_0(lx) g^{TE}_{\kappa_0}(l)\right) \sin 2\phi_r$ |

These estimators are provided for completeness, and for future application to experimental CMB maps. However, when we apply our real space estimators to simulated maps in Section 3.3, we make use of the estimators defined in Section 3.1.1.

Table 3.2: Shear plus estimators from real space correlation functions

| Estimator | Form | Kernel |
|---|---|---|
| $\hat{\gamma}_+^T$ | $\tilde{T}(\vec{x})(K_{\gamma_+^T} \circ \tilde{T})(\vec{x})$ | $K_{\gamma_+^T} = \left( \frac{1}{2\pi N_{\gamma_+}^{TT}} \int_0^\infty l dl J_2(lx) g_{\gamma_+}^{TT}(l) \right) \cos 2\phi_r$ |
| $\hat{\gamma}_+^+$ | $\tilde{Q}(\vec{x})(K_{\gamma_+^+} \circ \tilde{Q})(\vec{x}) + \tilde{U}(\vec{x})(K_{\gamma_+^+} \circ \tilde{U})(\vec{x})$ | $K_{\gamma_+^+} = \left( \frac{1}{2\pi N_{\gamma_+}^{EE}} \int_0^\infty l dl J_2(lx) g_{\gamma_+}^{EE}(l) \right) \cos 2\phi_r$ |
| $\hat{\gamma}_+^-$ | $\tilde{Q}(\vec{x})(K_{\gamma_+^-} \circ \tilde{Q})(\vec{x}) - \tilde{U}(\vec{x})(K_{\gamma_+^-} \circ \tilde{U})(\vec{x})$ | $K_{\gamma_+^-} = \left( \frac{1}{2\pi} \int_0^\infty l dl J_2(lx) \left( \frac{1}{\sqrt{2}} \frac{g_{\gamma_+}^{EE}(l)}{N_{\gamma_+}^{EE}} - \frac{1}{\sqrt{2}} \frac{g_{\gamma_+}^{EB}(l)}{N_{\gamma_+}^{EB}} \right) \right) \cos 2\phi_r +$ $+ \left( \frac{1}{2\pi} \int_0^\infty l dl J_6(lx) \left( \frac{1}{\sqrt{2}} \frac{g_{\gamma_+}^{EE}(l)}{N_{\gamma_+}^{EE}} + \frac{1}{\sqrt{2}} \frac{g_{\gamma_+}^{EB}(l)}{N_{\gamma_+}^{EB}} \right) \right) \cos 6\phi_r$ |
| $\hat{\gamma}_+^\times$ | $\tilde{Q}(\vec{x})(K^Q_{\gamma_+^\times} \circ \tilde{T})(\vec{x}) + \tilde{U}(\vec{x})(K^U_{\gamma_+^\times} \circ \tilde{T})(\vec{x})$ | $K^Q_{\gamma_+^\times} = \left( \frac{1}{4\pi} \int_0^\infty l dl J_0(lx) \left( \frac{1}{\sqrt{2}} \frac{g_{\gamma_+}^{TE}(l)}{N_{\gamma_+}^{TE}} - \frac{1}{\sqrt{2}} \frac{g_{\gamma_+}^{TB}(l)}{N_{\gamma_+}^{TB}} \right) \right) +$ $+ \left( \frac{1}{4\pi} \int_0^\infty l dl J_4(lx) \left( \frac{1}{\sqrt{2}} \frac{g_{\gamma_+}^{TE}(l)}{N_{\gamma_+}^{TE}} + \frac{1}{\sqrt{2}} \frac{g_{\gamma_+}^{TB}(l)}{N_{\gamma_+}^{TB}} \right) \right) \cos 4\phi_r$ $K^U_{\kappa_0^\times} = \left( \frac{1}{4\pi} \int_0^\infty l dl J_4(lx) \left( \frac{1}{\sqrt{2}} \frac{g_{\gamma_+}^{TE}(l)}{N_{\gamma_+}^{TE}} + \frac{1}{\sqrt{2}} \frac{g_{\gamma_+}^{TB}(l)}{N_{\gamma_+}^{TB}} \right) \right) \sin 4\phi_r$ |

## 3.2 Features of Real Space Estimators

We now explore various properties of the real space estimators we have introduced, including the shape of the kernels we use and the validity and consequences of using the squeezed triangle approximation.

### 3.2.1 Cumulative Information

We wish to find out which angular scales contribute the most statistical weight to each estimator in order to find out how small $L$ has to be for our squeezed triangle approximation to be valid. We do this by considering the cumulative information, or normalised cumulative signal-to-noise. For our estimators, $N_{\kappa_0}$ and $N_\gamma$ give the signal to noise squared per unit solid angle per unit $\kappa_0$, $\gamma_+$ or $\gamma_\times$, so $\chi^2(l) = \int_0^l N(l')dl'$, where the form of $N$ is given in Equations( 3.18), (3.22) and (3.26).

In order to perform this analysis we must specify the experimental configuration, since we need to use the noise of the experiment to determine the cumulative information. For a Gaussian beam, the noise is given by

$$n(l) = \sigma_p^2 e^{l^2 \theta_{beam}^2} \tag{3.79}$$

where $\theta_{beam}$ is the beam width and $\sigma_p$ is the detector noise in a pixel of side $\theta_{beam} = \theta_{FWHM}/\sqrt{8 \ln 2}$.

We compare an experiment with Planck's 143 GHz noise (Planck Collaboration et al., 2015b) to a next-generation experiment with the noise specifications of Advanced ACTPol's 150 GHz channel (Henderson et al., 2015). The specifications of the experiments are shown in Table (3.3).

Table 3.3: Planck and Advanced ACTPol Specifications

| Experiment | Channel | Beam Size $\theta_{FWHM}$ | Temperature Sensitivity | Polarisation Sensitivity |
|---|---|---|---|---|
| Planck | 143 GHz | 7.3 arcmin | 33 $\mu$K-arcmin | 70 $\mu$K-arcmin |
| AdvACT | 150 GHz | 1.4 arcmin | 7 $\mu$K-arcmin | 10 $\mu$K-arcmin |

The cumulative information for the Planck and AdvACT convergence and shear estimators is shown in Figure (3.2). Both components of the shear have the same cumulative information, plotted in black. Most of the information comes from scales over which the cumulative $\chi^2$ is changing.

Temperature estimators receive more contributions from higher angular wave numbers than polarisation estimators. For example, most of the information for the AdvACT TT estimator is found between $l \sim 1800$ and $l \sim 3000$, while for the EE estimator the corresponding scales are $l \sim 1000$ and $l \sim 2000$, and for the EB estimator most of the information comes from scales between $l \sim 400$ and $l \sim 1200$.

The improved resolution of AdvACT (solid curves) with $\theta_{beam} = 1.4$ arcminutes as opposed to Planck's beam of $\sim 7$ arcminutes means that more of the information comes from smaller scales, or larger $l$, for AdvACT than for Planck. For example for the TT estimator, most of the information for Planck comes from angular wave numbers between $l \sim 800$ and $l \sim 1600$, while for AdvACT the corresponding wavenumbers are between $l \sim 1800$ and $l \sim 3000$. The squeezed triangle approximation relies on this $l$ being much higher than the wavenumber $L$ of the lensing modes, so the squeezed triangle approximation is valid for a larger range of lensing modes for AdvACT than for Planck, allowing us to reconstruct the lensing field accurately on a wider range of scales.

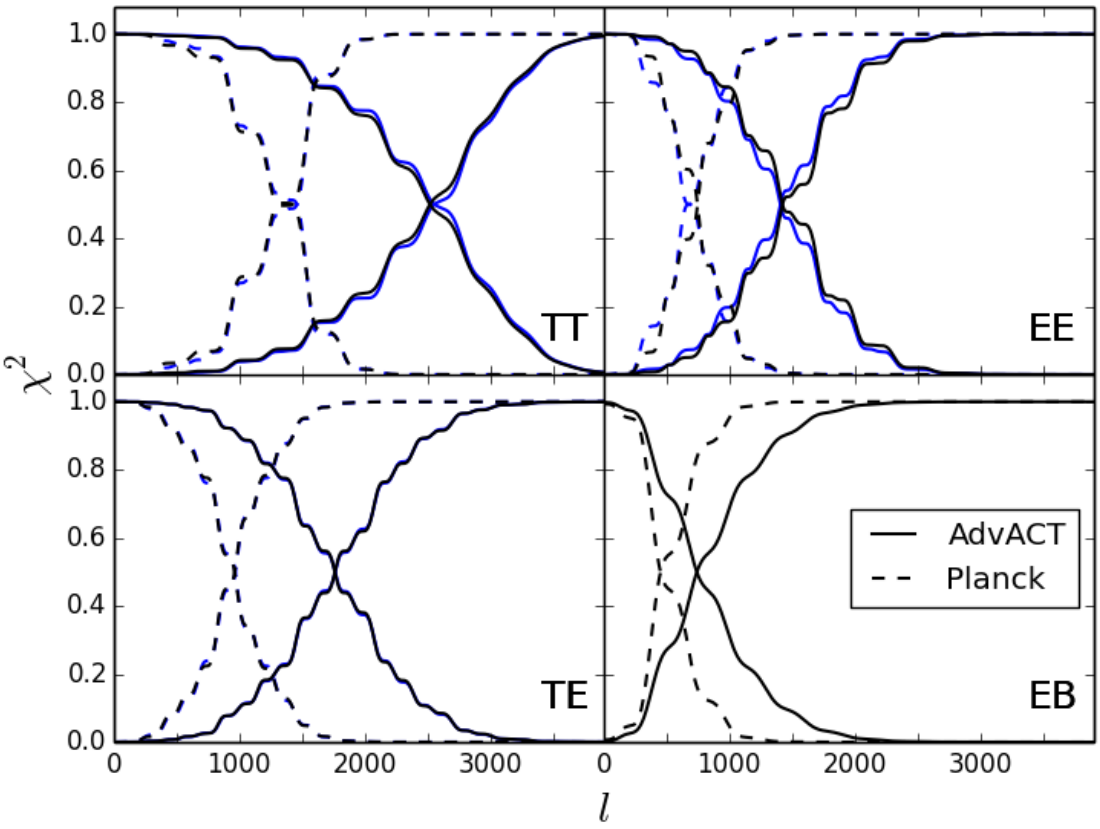


Figure 3.2: Normalised cumulative $\chi^2$, integrated from both the left and the right for different temperature and polarisation estimators, calculated using specifications from Planck (dashed lines) and AdvACT (solid lines). The blue curves are for convergence estimators while the black curves are for shear estimators.

### 3.2.2 Reconstruction Kernels

We now consider the shape of the kernels, $K(\vec{x})$, which are convolved with the lensed maps to obtain the lensing reconstruction. As discussed earlier, the real-space filters need to be limited in extent if we are to perform localised reconstructions on a small patch of the sky. The shapes of the lensing kernels in real space (Equations (3.30) and (3.32)) and harmonic space (Equations (3.19) and (3.23)) are shown in Figure (3.3) for the convergence estimators, and in Figure (3.4) for the shear estimators. Bucher et al. (2012) showed the kernels for the temperature estimator,

but the polarisation kernels are shown here for the first time. The plots are normalised to peak at unity for ease of comparison between the experimental configurations, which have different absolute normalisations.

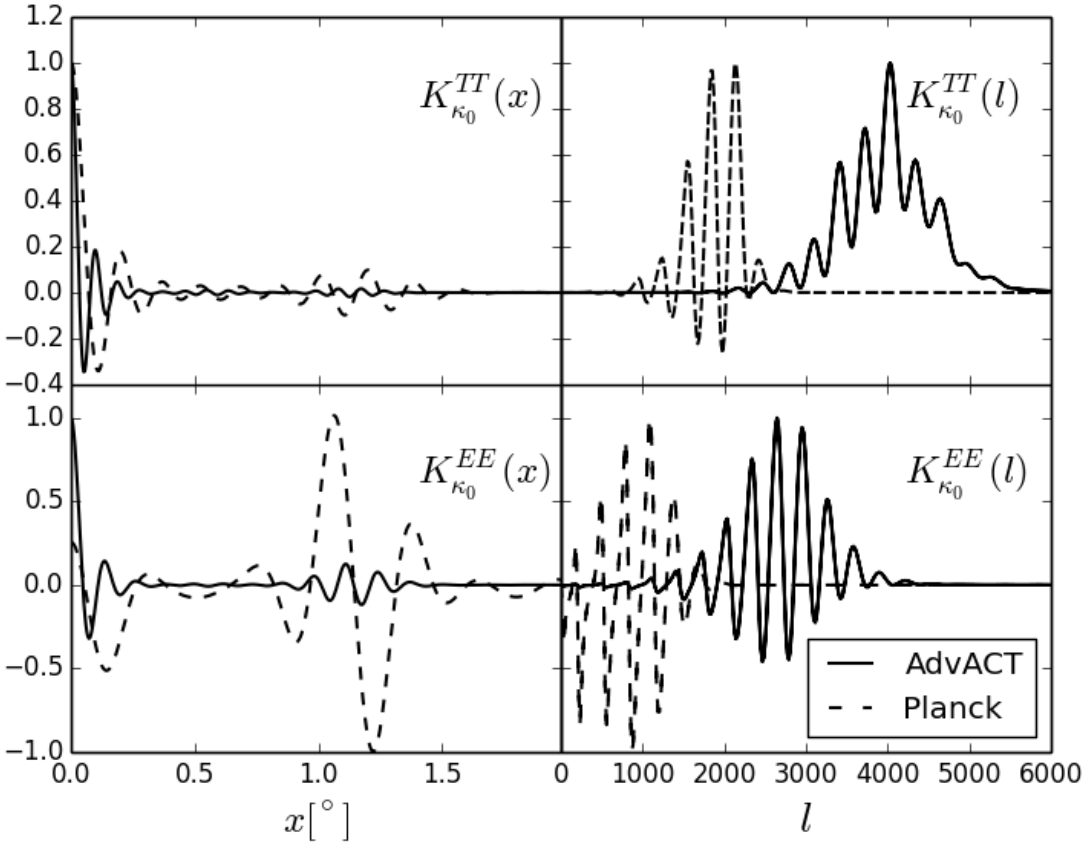


Figure 3.3: TT (top row) and EE (bottom row) convergence lensing kernels in real space (left column) and in Fourier space (right column)

The kernels for AdvACT peak at higher $l$ than those for Planck, meaning that the lensing reconstruction from maps with AdvACT noise and resolution receives much of its signal-to-noise from small-scale CMB modes that are lensed by larger-scale lensing fields. The temperature estimator reconstructions rely on higher angular wavenumbers (corresponding to smaller scale CMB anisotropies) than the polarisation estimators, as we found for the cumulative information.

Most of the information in the real space lensing kernels (in the column on the left of Figures

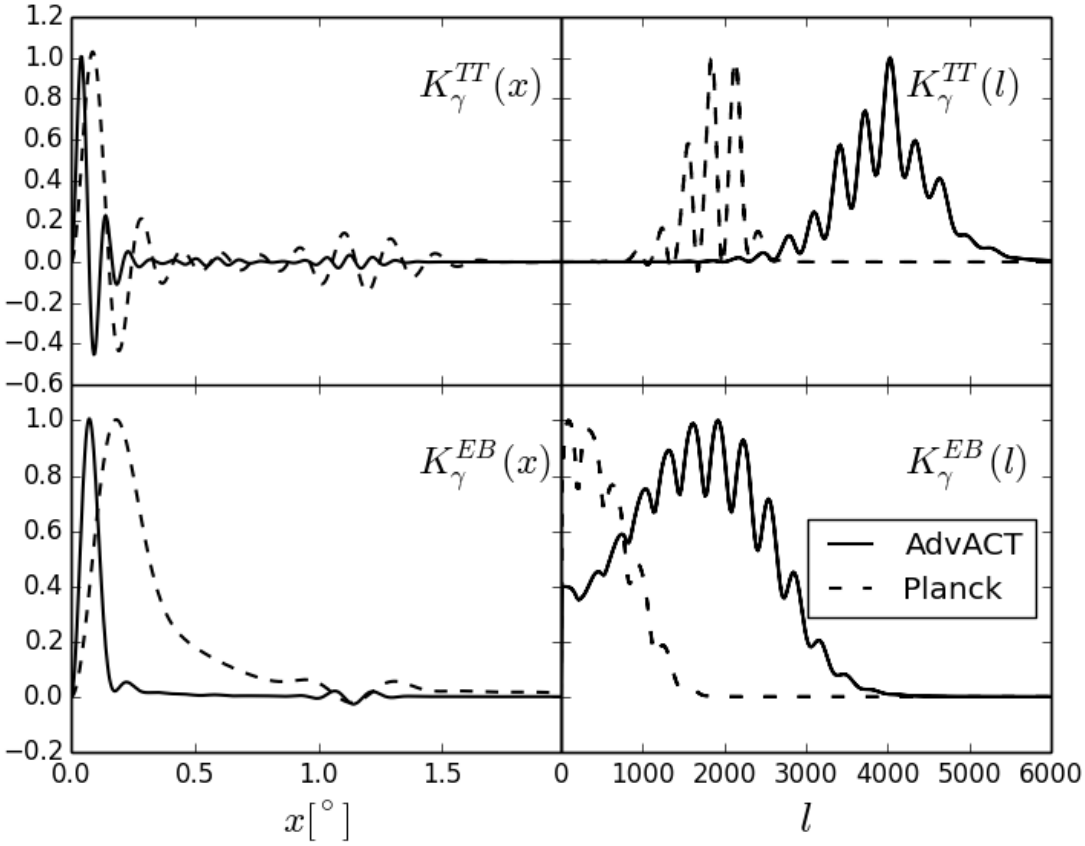


Figure 3.4: TT (top row) and EB (bottom row) shear lensing kernels in real space (left column) and in Fourier space (right column)

(3.3) and (3.4)) is contained within the first few arcminutes, with the kernels for AdvACT peaking at smaller angular scales than those for Planck. As discussed in Bucher et al. (2012), we can choose to restrict the real space filter to angular scales smaller than $x_{max}$ and then compute the optimal filter for that truncation scale from the full kernel. The limited angular extent of the filters means that we can perform the convolutions described in Section 3.1.1 over small areas of the sky, allowing us to perform localised reconstructions of the lensing convergence and shear.

**Foregrounds**

When we observe the sky at CMB frequencies, we do not only observe the lensed cosmic microwave background: there are other celestial objects that emit radiation at those frequencies, obscuring the signal we are looking for. There are also other secondary effects on the CMB apart from lensing, such as the thermal and kinetic Sunyaev-Zeldovich effects (Sunyaev and Zeldovich, 1970). One of the dominant CMB foregrounds comes from clustered cosmic infrared background sources (Dunkley et al., 2013), which begin to dominate the CMB signal at $l \sim 3000$. Thus for higher resolution experiments such as AdvACT, much of the apparent small scale signal will actually be from foregrounds, which will act as an additional source of noise in our reconstruction. To mitigate this, we can add the predicted foreground signal to our experimental noise term when we create our lensing reconstruction kernels, thus cutting off the kernels on scales that are dominated by foregrounds. Polarised foregrounds should also be taken into account to obtain kernels that give sensible results when applied to experimental maps (Planck Collaboration et al., 2015a). We do not deal with foregrounds in any more detail, as applying the estimators to experimental data is beyond the scope of this dissertation.

### 3.2.3 Multiplicative Bias

The real space estimators are only optimal in the limit of small lensing $L$, or in other words for lensing fields on much larger scales than the CMB anisotropies. For lensing fields with variations on smaller scales, that is to say lensing fields with higher $L$ modes, our reconstruction becomes less optimal and the reconstructed fields become less accurate for larger $L$, having too little or too much power (Bucher et al., 2012). We can calculate this modulation of reconstructed power as a function of $L$ by examining how a plane wave lensing field of wavenumber $L$ is reconstructed by our estimators. When the convergence is given by the plane wave $\kappa_0(\vec{x}) = Ae^{i\vec{L}\cdot\vec{x}}$, or in Fourier space $\kappa_0(\vec{l}) = (2\pi)^2 A\delta_D^2(\vec{l} - \vec{L})$, then the lensed temperature in Fourier space can be found in terms of the unlensed temperature and lensing field by Equation (2.93) to be

$$\tilde{T}(\vec{l}) = T(\vec{l}) - \frac{2A}{L^2}\vec{L}\cdot(\vec{l}-\vec{L})T(\vec{l}-\vec{L}), \tag{3.80}$$

We now investigate the lensing field that we reconstruct when the input lensing field is a plane wave with wavenumber $L$. We convert our expression for the reconstructed lensing field

into Fourier space, the convolution becomes a product and vice versa, giving

$$\begin{aligned}\langle\tilde{T}(\vec{l})\circ\Big(K(\vec{l})\tilde{T}(\vec{l})\Big)\rangle &= \langle\Big(T(\vec{l})-\frac{2A}{L^2}\vec{L}\cdot(\vec{l}-\vec{L})T(\vec{l}-\vec{L})\Big)\circ\Big(K(\vec{l})T(\vec{l})-\frac{2A}{L^2}\vec{L}\cdot(\vec{l}-\vec{L})K(\vec{l})T(\vec{l}-\vec{L})\Big)\rangle \\ &= \langle T(\vec{l})\circ\Big(K(\vec{l})T(\vec{l})\Big)\rangle + \langle\Big(-\frac{2A}{L^2}\vec{L}\cdot(\vec{l}-\vec{L})T(\vec{l}-\vec{L})\Big)\circ\Big(K(\vec{l})T(\vec{l})\Big)\rangle + \\ &+ \langle T(\vec{l})\circ\Big(-\frac{2A}{L^2}\vec{L}\cdot(\vec{l}-\vec{L})K(\vec{l})T(\vec{l}-\vec{L})\Big)\rangle + \mathcal{O}(A^2),\end{aligned} \tag{3.81}$$

where $K$ is the lensing reconstruction kernel. We thus find that the reconstructed convergence is given by

$$\begin{aligned}\langle\hat{\kappa_0}(\vec{L})\rangle &= \langle\tilde{T}(\vec{l})\circ\Big(K(\vec{l})\tilde{T}(\vec{l})\Big)\rangle - \langle T(\vec{l})\circ\Big(K(\vec{l})T(\vec{l})\Big)\rangle_{\phi=0} \\ &= \langle\Big(-\frac{2A}{L^2}\vec{L}\cdot(\vec{l}-\vec{L})T(\vec{l}-\vec{L})\Big)\circ\Big(K(\vec{l})T(\vec{l})\Big)\rangle + \langle T(\vec{l})\circ\Big(-\frac{2A}{L^2}\vec{L}\cdot(\vec{l}-\vec{L})K(\vec{l})T(\vec{l}-\vec{L})\Big)\rangle \\ &= \frac{2A}{L^2}\int d^2\vec{l}'K(\vec{L}-\vec{l}')\Big(\vec{L}\cdot\vec{l}'C_{l'}^{TT}-\vec{L}\cdot(\vec{l}'-\vec{L})C_{|\vec{l}'-\vec{L}|}^{TT}\Big).\end{aligned} \tag{3.82}$$

Dividing the reconstructed lensing field by the amplitude of the actual plane wave lensing field, we obtain the multiplicative bias, or form factor, which modulates the reconstructed lensing field amplitude as a function of wavenumber. We repeat an equivalent calculation for $EE$, $TE$, $EB$ and $TB$, deriving the form factors for the polarisation estimators, which is a new result. The expressions for the multiplicative bias for the various estimators are shown in Table (3.4). We obtain the multiplicative bias for the convergence and shear estimators by using their respective kernels.

Table 3.4: Form Factor Expressions

| Estimator | Form Factor |
|---|---|
| $TT$ | $\frac{2}{L^2}\int\frac{d^2\vec{l}}{2\pi}K(\vec{L}-\vec{l}')\Big(\vec{L}\cdot\vec{l}'C_{l'}^{TT}-\vec{L}\cdot(\vec{l}'-\vec{L})C_{\lvert\vec{l}'-\vec{L}\rvert}^{TT}\Big)$ |
| $EE$ | $\frac{2}{L^2}\int\frac{d^2\vec{l}}{2\pi}\cos 2(\phi_{\vec{l}'-\vec{L}}-\phi_{\vec{l}'})K(\vec{L}-\vec{l}')\Big(\vec{L}\cdot\vec{l}'C_{l'}^{EE}-\vec{L}\cdot(\vec{l}'-\vec{L})C_{\lvert\vec{l}'-\vec{L}\rvert}^{EE}\Big)$ |
| $TE$ | $\frac{2}{L^2}\int\frac{d^2\vec{l}}{2\pi}K(\vec{L}-\vec{l}')\Big(\vec{L}\cdot\vec{l}'\cos 2(\phi_{\vec{l}'-\vec{L}}-\phi_{\vec{l}'})C_{l'}^{TE}-\vec{L}\cdot(\vec{l}'-\vec{L})C_{\lvert\vec{l}'-\vec{L}\rvert}^{TE}\Big)$ |
| $EB$ | $\frac{2}{L^2}\int\frac{d^2\vec{l}}{2\pi}K(\vec{L}-\vec{l}')\vec{L}\cdot\vec{l}'\sin 2(\phi_{\vec{l}'-\vec{L}}-\phi_{\vec{l}'})C_{l'}^{EE}$ |
| $TB$ | $\frac{2}{L^2}\int\frac{d^2\vec{l}}{2\pi}K(\vec{L}-\vec{l}')\vec{L}\cdot\vec{l}'\sin 2(\phi_{\vec{l}'-\vec{L}}-\phi_{\vec{l}'})C_{l'}^{TE}$ |

The AdvACT and Planck form factors are shown for the shear (top panel) and convergence (bottom panel) estimators in Figure (3.5) (the shear plus and shear cross estimators have the same

form factor). For large-scale lensing fields, or small angular wave numbers $L \lesssim 100$, the lensing amplitude is accurately reconstructed because our squeezed triangle approximation is valid, while for smaller scale lensing variations the amplitude of the reconstruction is incorrect and must be rescaled. The temperature and $EB$ estimators have the most promising form factors, as the multiplicative bias falls off much less steeply with $L$ than for the other estimators. The AdvACT form factor curves tend to be higher than the corresponding Planck curves. This is because the improved specifications of the Advanced ACTPol experiment give us a better reconstruction out to higher $L$ than Planck, as we inferred from the cumulative information plot.

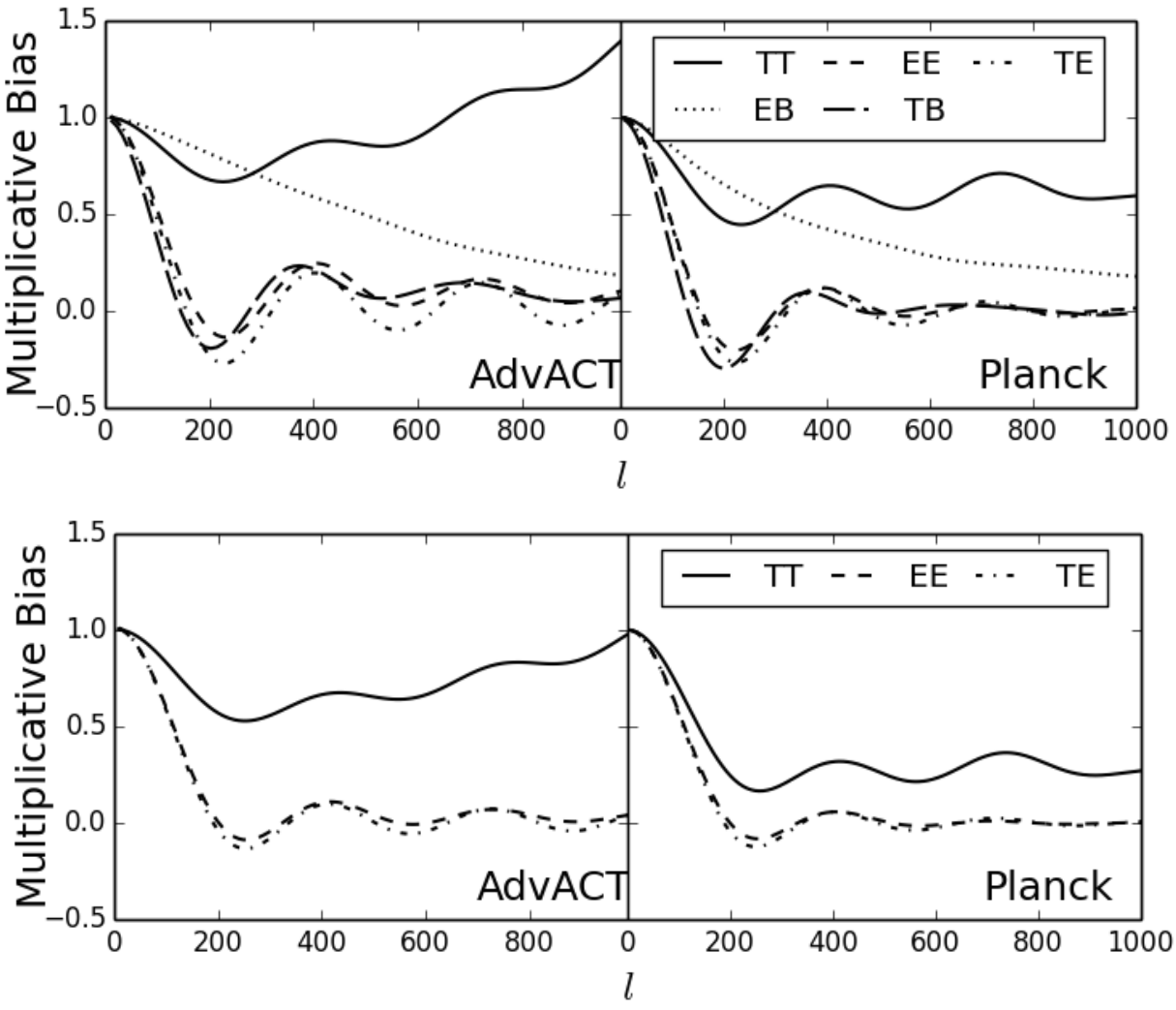


Figure 3.5: Multiplicative bias for the shear estimators (top) and convergence estimators (bottom)

Bucher et al. (2012) presented the multiplicative bias for temperature estimators applied to an experiment with Planck's sensitivity and resolution. The plot was generated using simulated lensing of temperature maps by plane wave lensing fields of different wavenumbers. Numerical errors due to low resolution simulated maps resulted in the form factor being slightly overestimated in this analysis, and also resulted in different form factors for the two shear estimators which in fact have identical multiplicative bias curves. This illustrates the value of the analytical expression for the form factor which we have developed: the computation of the form factor is reduced to numerical integration, which is faster to compute and more accurate than the simulation method.

Since we can calculate how the reconstructed lensing amplitude falls off on smaller scales (larger $L$), we can correct for this loss of reconstructed power in the convergence and shear power spectra, at the expense of an increase in the variance of our estimators.

## 3.3 Simulated CMB Lensing Map Reconstructions

In this section, we test the real space estimators presented in Section 3.1.1 on simulated CMB maps. We generate simulated CMB temperature and polarisation maps and lensing maps from the spectra produced by CAMB: the Code for Anisotropies in the Microwave Background (Lewis and Challinor, 2011). We use the simulated lensing maps to shift the unlensed CMB maps by the deflection angle, making use of a high resolution unlensed map (with a pixel scale of 0.3 arcminutes) to accurately simulate the deflection. We obtain lensed CMB maps in a $20^\circ$ by $20^\circ$ region of the sky with pixels of width 0.6 arcminutes. We then include experimental beam smearing effects and add experimental noise to obtain our final simulated lensed maps. These are the maps to which the real space estimators of Equations (3.31) and (3.34) are applied. The simulation code is an extended version of code developed by Ridl (2012) and Bucher et al. (2012). The unlensed and lensed temperature maps and the deflection angle are shown in Figure (2.3). The Q and U mode polarisation maps are shown in Figure (3.6), with the unlensed maps in the left column and the lensed maps with Planck noise in the right column. The lensing effect is small, and is difficult to detect by eye in map space, but the beam smearing in the maps on the

right is clearly visible.

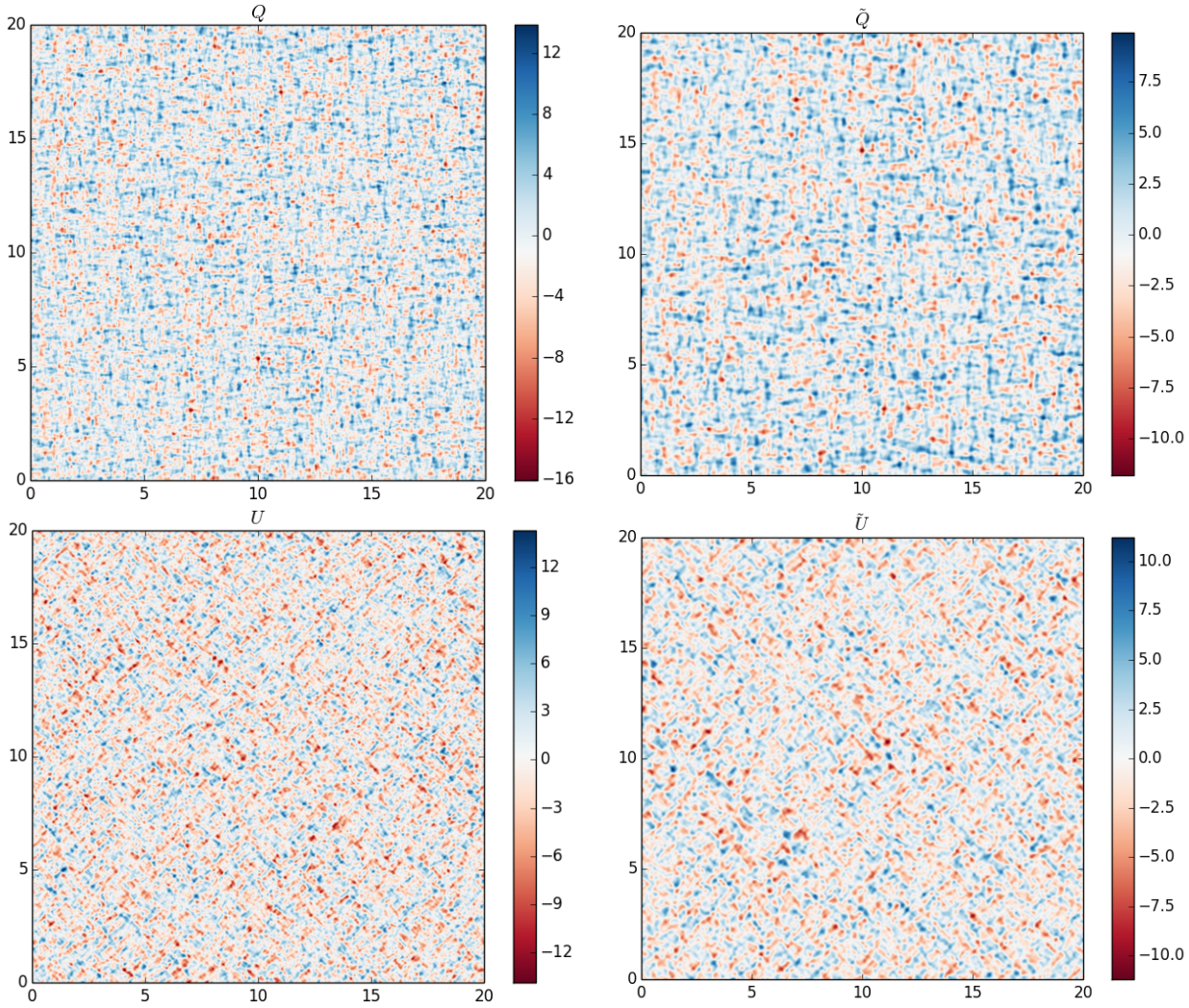


Figure 3.6: The simulated primordial Q and U polarisation maps (left top and bottom respectively) and the lensed Q and U maps with Planck noise (right top and bottom). The color scale is in $\mu$K and the axes are in degrees.

The reconstructed convergence is shown in Figure (3.7) for different combinations of temperature and E mode maps for AdvACT and Planck noise specifications, and the reconstructed shear for the EB and TB estimators is shown in Figure (3.8). The colour map shows the reconstructed field while the contours show the actual lensing field used. For an accurate reconstruction, the blue colour map regions should align with the solid contours (map positive), while the red regions should align with the dotted contours (map negative). The maps have been smoothed, keeping

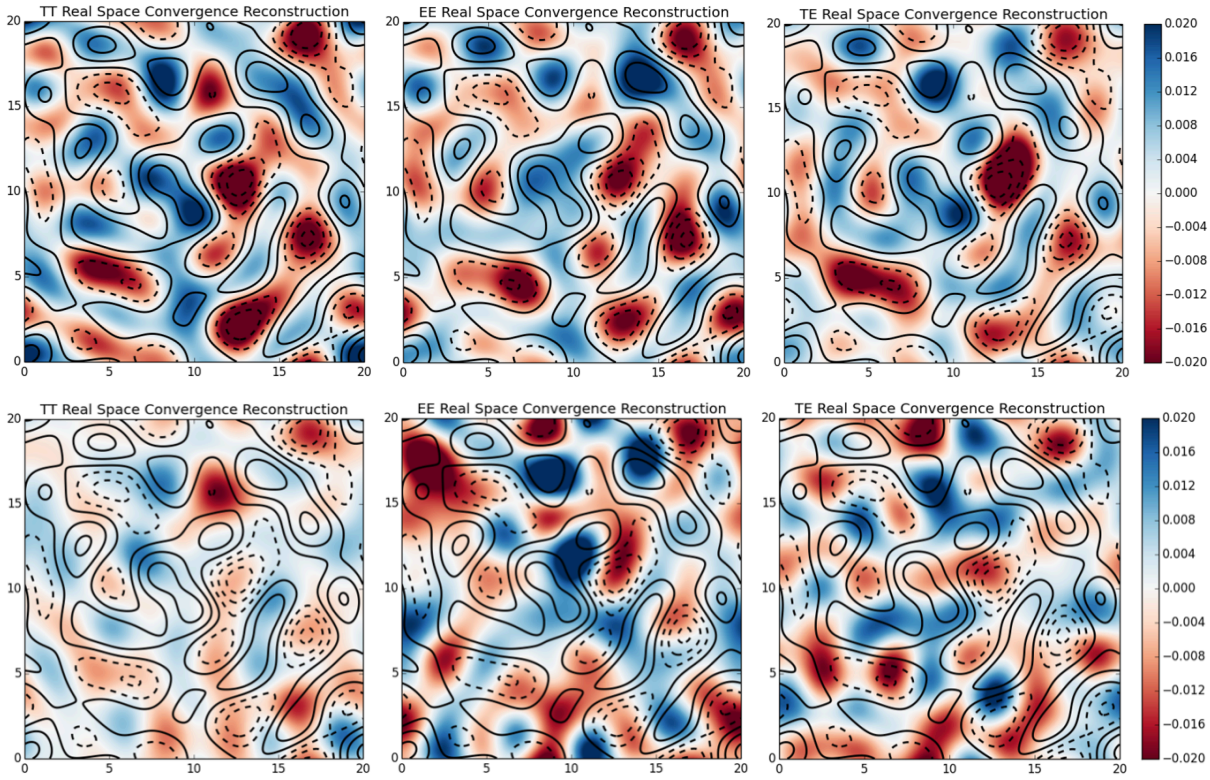


Figure 3.7: The real space convergence estimator applied to a $20^\circ$ by $20^\circ$ lensed temperature map (left), E mode polarisation map (centre), and a combination (right). The maps have been smoothed, keeping only Fourier modes with $15 < l < 100$. AdvACT noise (top row) and Planck noise (bottom row) has been added to the CMB maps and used in the reconstruction filter.

only Fourier modes with $15 < l < 100$ to show the modes that are not severely compromised by the form factor and to make the correspondence between the input and output maps clearer. Most of the reconstructed maps broadly recover the input lensing field on these scales, although the noise of the reconstructions varies.

### Instrumental Noise

Our lensing reconstructions are clearly affected by the instrumental noise of the experiment. For AdvACT noise, shown in the top row of Figures (3.7) and (3.8), the reconstructed convergence corresponds closely to the input convergence. The higher noise and poorer resolution of the Planck experiment, shown in the bottom row of the same figure, results in a much less accurate

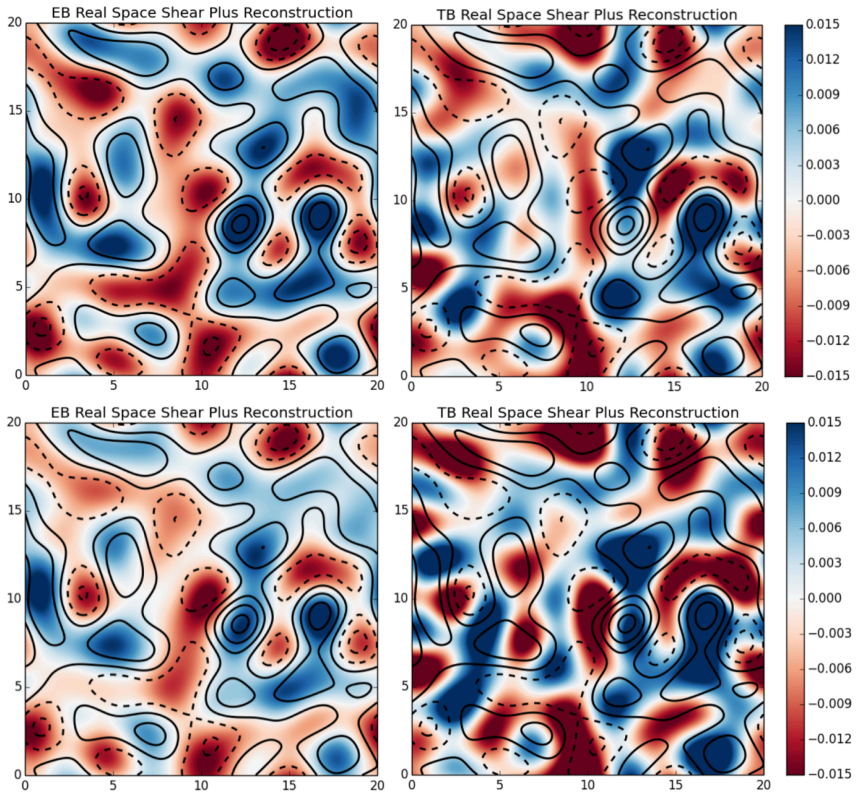


Figure 3.8: The real space shear plus estimator applied to $20°$ by $20°$ lensed E and B mode polarisation maps (left), and a temperature and temperature and B mode polarisation (right). The maps have been smoothed, keeping only Fourier modes with $15 < l < 100$. AdvACT noise (top row) and Planck noise (bottom row) has been added to the CMB maps and used in the reconstruction filter.

lensing reconstruction, as can be seen by comparing the corresponding AdvACT and Planck reconstructions.

As telescope sensitivity improves, the resulting CMB maps become less noisy and so our reconstructions improve. Additionally, as resolution improves, the smaller beam means less smearing of the observed CMB, giving us access to the small-scale CMB modes that are most affected by lensing and allowing us to reconstruct the lensing effect with much higher accuracy. In the following discussion we will use plots with AdvACT specifications.

We have not simulated the foregrounds that are included in the maps for any real CMB experiment. Foregrounds dominate the CMB on small scales and this would need to be taken

into account in the lensing kernel before applying these estimators to experimental data.

**Reconstruction noise from the unlensed map and cosmic variance**

Our lensing reconstructions contain noise due to apparent shear and convergence signals from the unlensed maps: not all of the reconstructed power comes from the true lensing signal. When we are working with observations, we cannot mitigate this effect in map space as we have no way to access a map of the primordial CMB. We can use our simulated maps to illustrate the effect of the unlensed map on the lensing reconstruction. This is shown for one of the shear reconstructions from temperature maps in Figure (3.9), where we can see from the top right panel that merely applying the lensing estimator to our simulated primordial CMB maps, which have no lensing signal, results in a nonzero estimated lensing field. The reconstruction from the lensed map (top left panel) has a noise contribution because of this. If we subtract off this noise from the lensing reconstruction, we see that our reconstruction improves dramatically (bottom left panel). This demonstrates the noise introduced into the reconstruction because of the unlensed CMB, but we cannot remove the noise in this way for an actual experimental map.

Our universe is only one of many possible realisations of the underlying statistics. If we had access to many realisations of the primordial CMB that were all lensed by the same field, we could distinguish the true lensing signal from the shape of the primordial anisotropies (Kesden et al., 2003). This is shown in the bottom right panel of Figure (3.9), where we see that in the artificial case of having many realisations of the unlensed CMB, we are able to obtain an accurate reconstruction because the noise from the different realisations is uncorrelated and averages down. Part of the improvement in the reconstruction is also due to the instrumental noise being reduced by taking an average, so the EB reconstruction also improves very slightly, as seen in Figure (3.10). Again, we cannot mitigate this effect in map space in reality, but we can improve our reconstructed lensing field power spectrum by observing many patches of the sky and combining the reconstructions in those different patches, as the large scale structure should have the same statistical properties in different regions of the sky.

In the case of estimators that depend on B modes, the reconstruction signal from the unlensed

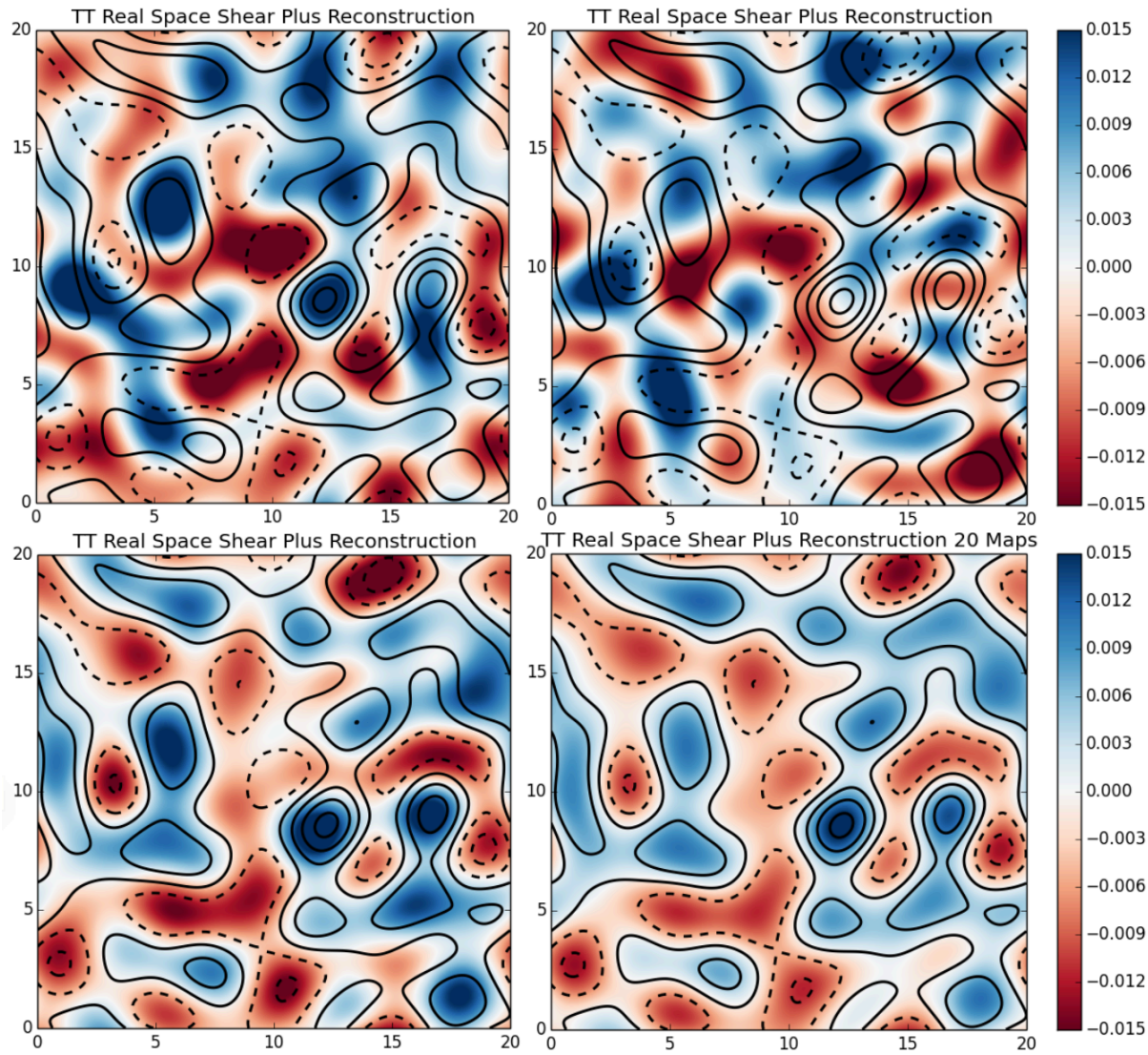


Figure 3.9: The real space temperature shear estimator applied to a $20°$ by $20°$ lensed temperature map (top left) and unlensed temperature map (top right), as well as the difference between the two reconstructions (bottom left) and the reconstruction averaged over 20 realisations of the unlensed CMB (bottom right). The maps have been smoothed, keeping only Fourier modes with $15 < l < 100$. The colour map shows the reconstructed field while the contours show the actual lensing field. AdvACT noise has been added to the CMB maps and used in the reconstruction filter.

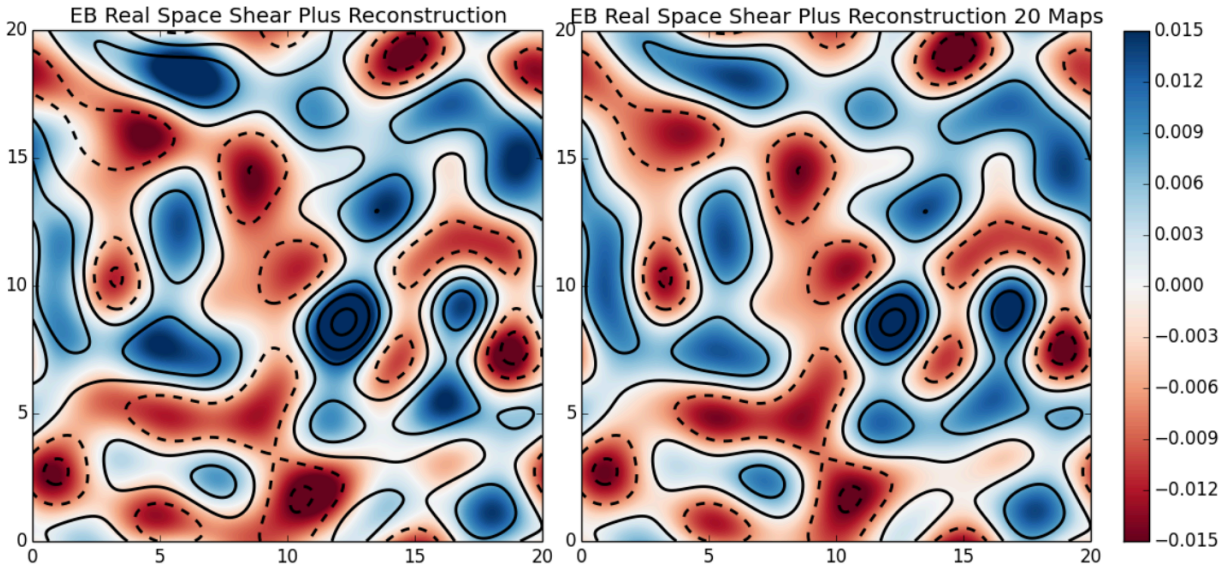


Figure 3.10: Shear plus reconstructed from E and B maps for one map (left) and averaged over 20 maps (right). The maps have been smoothed, keeping only Fourier modes with $15 < l < 100$. The colour map shows the reconstructed field while the contours show the actual lensing field. AdvACT noise has been added to the CMB maps and used in the reconstruction filter.

fields is approximately zero, as primordial B modes are negligibly small for our purposes. These estimators therefore do not have additional noise from the unlensed maps, and so the EB and TB estimators could prove promising for future experiments that can robustly detect lensed B modes. This is illustrated in Figure (3.10), which shows that the shear reconstruction from the EB estimator gives a very accurate, low-noise reconstruction on the scales shown.

### 3.3.1 Lensing Reconstruction Applications

#### Power Spectrum Estimation

We can use our reconstructed maps to find the angular power spectra of the lensing fields, for example for the convergence

$$\langle \kappa(\vec{l})\kappa^*(\vec{l'})\rangle = (2\pi)^2\delta_D^2(\vec{l}-\vec{l'})C_l^{\kappa\kappa}, \tag{3.83}$$

and similarly for the two lensing shear components. To obtain the power spectrum we need to take the Fourier transform of the reconstructed lensing field in a patch of the sky. This has some practical difficulties, but various techniques can improve the accuracy of such a Fourier transform such as an apodisation window to reduce ringing, and treating the map to reduce mode mixing (Das et al., 2011a). Obtaining the lensing angular power spectrum has the advantage of allowing us to remove the cosmic variance contribution to the lensing reconstruction by making use of the statistical properties of the CMB.

The cosmic variance of the reconstructed lensing map due to the unlensed CMB maps is seen as excess power in the lensing reconstruction power spectrum (Kesden et al., 2003). We can mitigate the effect on the power spectrum by simulating approximate unlensed CMB maps, applying our estimators to these maps, and estimating the excess power that they contribute. The approximate unlensed CMB maps can be obtained by randomising the phases of the lensed maps in Fourier space to recover the Gaussian random field we expect for the primordial CMB (thus removing the non-Gaussianities induced by lensing). This term is the Gaussian bias discussed in Das et al. (2011b).

We plan to extend the results in this chapter to include a more realistic treatment of the noise contribution from the unlensed CMB to improve the reconstructed lensing power spectrum.

### Cosmological Parameter Estimation

CMB lensing can be used in combination with the CMB power spectrum to constrain dark energy. The expansion rate cannot be distinguished from curvature using the primordial CMB power spectrum alone, as both expansion and curvature affect the angular scale of the first acoustic peak of the CMB power spectrum which corresponds to a fixed physical scale. This is known as the geometric degeneracy. However, CMB lensing provides complementary constraints on the geometry of the universe and the growth of structure, allowing us to distinguish between geometry and expansion, and constrain dark energy models (Stompor and Efstathiou, 1999). The CMB lensing power spectrum has been used for this purpose in, for example Sherwin et al. (2011); Planck Collaboration et al. (2015d,e).

Massive neutrinos are relativistic at early times, and contribute to the radiation energy density, but later become non-relativistic and similar to cold dark matter because of their weak interaction cross-section. Massive neutrinos affect the expansion rate of the universe as well as growth of structure, suppressing the matter power spectrum on scales smaller than the free-streaming scale by a factor proportional to the sum of neutrino masses (Lesgourgues et al., 2006). CMB lensing probes the matter power spectrum, and can thus constrain the mass of neutrinos (Allison et al., 2015a).

### Cross-Correlation Studies

The real space lensing reconstructions we have developed and demonstrated in this chapter allow us to probe the matter distribution in our universe, which is dominated by dark matter. This has many applications, one of which is cross-correlating the lensing field with other tracers of matter.

Cross-correlations of CMB lensing with dark matter tracers have been detected. CMB lensing has been cross-correlated with quasars (Sherwin et al., 2012), the cosmic infrared background (Holder et al., 2013), galaxy lensing (Hand et al., 2015; Liu and Hill, 2015) and galaxy distri-

butions (Pearson and Zahn, 2014; Kuntz, 2015), including high redshift submillimetre galaxies (Bianchini et al., 2015) and radio galaxies (Allison et al., 2015b).

Cross-correlations between lensing and other dark matter tracers allow us to constrain the bias of these tracers (Sherwin et al., 2012; Masui et al., 2013; Pearson and Zahn, 2014). Additionally, cross-correlations of a foreground lens plane with lensing from two different background source planes (such as the CMB at $z \approx 1100$ and background sources for galaxy lensing at much lower redshifts) probe the geometrical distances to different redshifts, and thus constrain dark energy parameters (Jain and Taylor, 2003; Bernstein and Jain, 2004; Zhang et al., 2005; Das and Spergel, 2009). CMB lensing can thus be used in cross-correlation to study the clustering properties of matter tracers relative to the underlying dark matter as well as to constrain cosmology.

# CHAPTER 4

# Cross-Correlation of CMB Lensing with HI Intensity Mapping

The primordial perturbations that later form the observed large scale structure are predicted by single-field inflation to be adiabatic, in which case the baryon density contrast spatially traces the dark matter density contrast. Neutral hydrogen (HI) gas is thus a biased tracer of dark matter. On large scales the HI bias is approximately constant because we average over many galaxies. This is confirmed by simulations. On smaller scales, the HI gas falls into the gravitational potential wells created by dark matter overdensities, resulting in an increase in the bias which depends on the details of how HI is clustered relative to the dark matter (Davé et al., 2013; Santos et al., 2015).

In addition to the the cosmological constraints that can be obtained from the HI power spectrum, HI data can be cross-correlated with other matter tracers to study the clustering properties of HI. HI intensity maps from the Green Bank Telescope have been cross-correlated with galaxies from the DEEP2 Survey (Chang et al., 2010) and later the Wiggle-Z survey (Masui et al., 2013). The possibility of detecting the cross-correlation of HI intensity maps with Lyman Break Galaxies (Villaescusa-Navarro et al., 2015), the Integrated Sachs Wolfe effect on the CMB (Guha Sarkar et al., 2009), galaxy lensing (Pourtsidou et al., 2015a,b) and CMB weak lensing (Guha

Sarkar, 2010) have been investigated.

In the previous chapter, we explored a novel method of reconstructing the gravitational lensing signal from CMB temperature and polarisation maps. We now investigate the cross-correlation of CMB lensing with HI, and the prospects for detecting this cross-correlation with the Hydrogen Intensity and Real-time Analysis eXperiment (HIRAX) (HIRAX Collaboration, 2016). The code that produced the results shown in this chapter, including all HI and cross-correlation angular power spectrum results, was developed in collaboration with A Pénin for an upcoming paper.

## 4.1 Neutral Hydrogen

Hydrogen constitutes around $75\%$ of the total baryonic mass of the universe, making it the most abundant element. Neutral hydrogen atoms first formed at recombination at a redshift of $z \sim 1100$, when the universe cooled sufficiently for protons and electrons to bond without being broken apart by an ionising photon (Peebles, 1968; Zeldovich et al., 1968). Most of the hydrogen in the universe remained neutral throughout the so-called dark ages after recombination, until the first stars lit up the sky at $z \sim 30 - 15$ (Bromm and Larson, 2004; McKee and Ostriker, 2007; Zinnecker and Yorke, 2007). The UV radiation from these stars began to ionise the neutral hydrogen, a period appropriately called the epoch of reionisation, which lasted from $z \sim 15$ to $z \sim 6$ (Barkana and Loeb, 2001). In the post-reionisation universe most of the hydrogen is ionised (denoted HII), with what is left of the neutral hydrogen situated mainly in the interstellar medium of galaxies (Bagla et al., 2010), or in dense regions of the intergalactic medium where the recombination rate is high enough to maintain a neutral hydrogen presence (Wyithe and Loeb, 2008).

Neutral hydrogen observations can be used to probe the dark ages and the epoch of reionisation (Furlanetto et al., 2006). Existing experiments such as the Murchison Widefield Array (MWA) and the Precision Array for Probing the Epoch of Reionization (PAPER) have placed upper bounds on the high-redshift HI power spectrum (Beardsley and MWA Collaboration, 2015; Ali et al., 2015), and upcoming experiments including the Hydrogen Epoch of Reionisation Ar-

ray (HERA) and the Square Kilometer Array (SKA) expect to make robust detections (DeBoer and HERA, 2015; Koopmans et al., 2015).

Post-reionisation HI observations probe the expansion history of the universe and therefore dark energy by constraining the baryon acoustic oscillation (BAO) scale in much the same way as galaxy redshift surveys (Blake and Glazebrook, 2003; Hu and Haiman, 2003; Seo and Eisenstein, 2003). In the post-reionisation epoch , HI is a biased tracer of the dark matter fluctuations (Bharadwaj et al., 2001; Wyithe and Loeb, 2008):

$$\delta_{HI}(\vec{k}) = b_{HI}\delta_m(\vec{k}). \tag{4.1}$$

Independent observations of the HI and dark matter distributions can therefore be used to constrain the bias of HI. One way of doing this is to cross-correlate CMB lensing with HI observations.

### 4.1.1 HI Lines

Neutral hydrogen can be detected by radiation that it emits and absorbs during transitions. The Lyman-alpha transition between the first excited electronic state of hydrogen (n=2) and the ground state (n=1) can be observed as an absorption feature if an HI region is illuminated from behind by a distant galaxy or quasar, resulting in n=1 electrons absorbing photons with $\lambda = 1216\mathring{A}$. The redshift of the absorption line corresponds to the distance to the HI region.

In recent years much attention has turned to the hyperfine spin-flip transition of atomic hydrogen. An electron in the ground state of hydrogen (n=1) has slightly higher energy if its spin is aligned with that of the proton than if it were anti-aligned, because of the interaction between their magnetic moments. A transition between these two states results in the emission or absorption of a photon with $\lambda$ =21 cm, or $\nu$ =1420 MHz. This is a forbidden transition with a long lifetime of $10^7$ years, but because of the abundance of neutral hydrogen even post-reionisation, enough 21 cm radiation is produced to be used as a probe of HI over a wide range of redshifts. The viability of observing the 21 cm emission of HI was first predicted by van de Hulst in 1944 after Oort prompted him to investigate emission lines, and 21 cm radiation from within our galaxy was detected a few years later (Ewen and Purcell, 1951).

### 4.1.2 Intensity Mapping

Mapping the HI emission from individual galaxies requires very sensitive, high resolution experiments. An alternative approach is intensity mapping, in which the integrated 21 cm emission of many galaxies in a pixel in three-dimensional space is measured (Chang et al., 2008; Loeb and Wyithe, 2008). The three-dimensional information is obtained by measuring angular fluctuations at different frequencies, which correspond to different redshifts. Large volumes of the universe can be probed efficiently using this method, and the noise and resolution requirements of an intensity mapping experiment are not as stringent as they would be to detect individual galaxies. This technique will be employed by upcoming dedicated experiments such as the Canadian Hydrogen Intensity Mapping Experiment (CHIME) (Vanderlinde and Chime Collaboration, 2014)), the Baryon acoustic oscillations In Neutral Gas Observations experiment (BINGO) (Battye et al., 2012), Tianlai (Chen, 2015), and the Hydrogen Intensity and Real-time Analysis eXperiment (HIRAX) as well as multi-purpose radio telescopes like MeerKAT (Booth and Jonas, 2012) and the Square Kilometer Array (Santos et al., 2015) . Large volume intensity mapping surveys are expected to result in cosmological constraints competitive with those from galaxy redshift surveys (Bull et al., 2015).

We will focus on probing the HI distribution using HI intensity mapping data from HIRAX, an experiment which will be operational in the Karoo in the next few years. HIRAX will consist of 1000 dishes, each 6 m in diameter, which will be arranged in a close-packed structure that makes use of redundant baselines.

### 4.1.3 HI Intensity Mapping Signal

The HI signal observed by radio telescopes is the flux density of the 21 cm emission line, which corresponds to the source intensity $I_\nu$ integrated over the beam. Using the Rayleigh-Jeans approximation, the intensity is converted to a brightness temperature $T = \frac{I_\nu c^2}{2k_B\nu^2}$. The total HI 21 cm signal is thus $T = \bar{T}(1 + \delta_{HI})$, where $\delta_{HI}$ is the HI density contrast. We are interested in the fluctuations $\delta T$ about the mean brightness temperature $\bar{T}$:

$$\delta T(\hat{n}, \nu) = \bar{T}(z)\delta_{HI}(\chi\hat{n}, z), \tag{4.2}$$

where $\nu = \frac{1420\text{MHz}}{1+z}$ is the observed frequency for 21 cm radiation at redshift z, $\chi$ is the comoving distance, and the mean brightness temperature is given by (Santos et al., 2015)

$$\bar{T} \approx 566h \left(\frac{H_0}{H(z)}\right) \left(\frac{\Omega_{HI}(z)}{0.003}\right) (1+z)^2 \mu\text{K}. \tag{4.3}$$

The HI density fraction $\Omega_{HI}(z) = \bar{\rho}_{HI}(z)/\rho_c$ gives the ratio of the average comoving neutral hydrogen density at redshift $z$ to the critical density of the universe at the present time. Current constraints indicate that $\Omega_{HI} \approx 10^{-3}$ independent of redshift for $z = 2 - 4$ (Péroux et al., 2003; Zafar et al., 2013).

The HI density contrast in Fourier space in the flat sky approximation is given by (Bull et al., 2015)

$$\delta_{HI}(\vec{k}) = (b_{HI} + f\mu^2)\delta_m(\vec{k}), \tag{4.4}$$

where we have modified Equation (4.1) to include the effects of redshift space distortions. We include redshift space distortions because we measure the HI brightness temperature as a function of frequency and thus redshift instead of comoving distance, meaning that peculiar velocities can cause apparent distortions along the line of sight (Kaiser, 1987). Here $\mu = k_\parallel/k$ and the linear growth rate $f$ is related to the growth factor $D$ of Equation (2.70) by $f = d\log D/d\log a$. The growth rate is related to the matter density parameter by $f(z) = \Omega_m(z)^\gamma$, where for the $\Lambda$CDM model $\gamma = 0.55$ (Bull et al., 2015).

The redshift evolution of the HI bias is not well constrained at present. There are a few observational constraints on the bias (Martin et al., 2012; Switzer et al., 2013; Masui et al., 2013), and some from hydrodynamical simulations (Wilman et al., 2008), but different predictions of the evolution of the HI bias are not in agreement (Padmanabhan et al., 2015a,b).

We can use a model of how the HI is distributed within dark matter haloes to predict the evolution of the bias and HI density fraction (Bagla et al., 2010). If a dark matter halo of mass $M$ contains a total HI mass $M_{HI}(M, z)$, and only haloes between masses $M_{min}$ and $M_{max}$ host HI, then the proper HI density is (Bull et al., 2015; Santos et al., 2015)

$$\rho_{HI}(z) = \int_{M_{min}}^{M_{max}} dM \frac{dn}{dM} M_{HI}(M), \tag{4.5}$$

where $\frac{dn}{dM}$ is the proper halo mass function. The HI bias is given by

$$b_{HI}(z) = \frac{1}{\rho_{HI}} \int_{M_{min}}^{M_{max}} dM \frac{dn}{dM} M_{HI}(M) b(M, z), \tag{4.6}$$

where $b(M, z)$ is the halo bias. The proper HI density fraction $\Omega_{HI}$ is then

$$\Omega_{HI}(z) = \frac{\rho_{HI}(z)}{(1+z)^3 \rho_{c,0}}. \tag{4.7}$$

The halo mass range for haloes expected to contain HI is given in Bagla et al. (2010). Following Bull et al. (2015) we assume that $M_{HI}$ is redshift independent and given by the power law $M_{HI} = M^{0.6}$, normalised to match the constraints from Switzer et al. (2013).

### HI signal in a bin

The neutral hydrogen signal in a frequency or redshift bin is the three dimensional signal projected along the line of sight. The signal in the direction $\hat{n}$ is given by

$$\delta T_{bin}(\hat{n}) = \int_{bin} d\nu F(\nu) \delta T(\hat{n}, \nu) \tag{4.8}$$

$$= \int_{z_{min}}^{z_{max}} \frac{dz}{(1+z)^2} \nu_{21} F\left(\nu(z)\right) \delta T(\hat{n}, z) \tag{4.9}$$

where $\nu_{21}$ =1420 MHz is the frequency of the 21 cm line, $F$ is the projection kernel weighting the contribution of the temperature contrast at different redshifts, and the temperature contrast $\delta T$ is defined in Equation (4.2). The optimal kernel will depend on the noise frequency spectrum go the experiment. For simplicity, we use a top-hat kernel to average the signal in a given frequency bin, choosing $F(\nu) = \frac{1}{\Delta\nu}$, which gives

$$\delta T_{bin}(\hat{n}) = \frac{1}{\Delta\tilde{\nu}} \int_{z_{min}}^{z_{max}} \frac{dz}{(1+z)^2} \delta T(\hat{n}, z), \tag{4.10}$$

where $\Delta\tilde{\nu} = \Delta\nu/\nu_{21}$ is the dimensionless bandwidth.

In the flat sky approximation, we approximate a small region of the sky as a plane. The unit vector $\hat{n}$ can be decomposed as (Datta et al., 2007)

$$\hat{n} = \vec{m} + \vec{x} \tag{4.11}$$

where $\vec{m}$ points to the small region we are observing and $\vec{x}$ gives the position within that region, with $\vec{m} \cdot \vec{x} = 0$, and $x \ll 1$ and $m \approx 1$.

We define the two dimensional Fourier transform of the temperature fluctuations in the plane of the sky to be

$$\delta T_{bin}(\vec{l}) = \int d^2\vec{x} e^{-i\vec{l}\cdot\vec{x}} \delta T_{bin}(\hat{n}) \tag{4.12}$$

where $\vec{l}$ gives the angular wavevector in the plane of the sky. Using the expression for $\delta T(\hat{n})$ from Equation (4.9) and writing $\delta_{HI}(\hat{n})$ in terms of its Fourier transform, we find

$$\delta T_{bin}(\vec{l}) = \frac{1}{\Delta\tilde{\nu}} \int d^2\vec{x} e^{-i\vec{l}\cdot\vec{x}} \int_{z_{min}}^{z_{max}} \frac{dz}{(1+z)^2} \bar{T}(z) \int \frac{d^3\vec{k}}{(2\pi)^3} e^{i\chi\hat{n}\cdot\vec{k}} \delta_{HI}(\vec{k}, z), \tag{4.13}$$

where $\vec{k} \cdot \hat{n} = \vec{k} \cdot \vec{m} + \vec{k} \cdot \vec{x} = k_\parallel + \vec{k}_\perp \cdot \vec{x}$. The component of the three dimensional wavevector in the plane of the sky or perpendicular to the line of sight ($\vec{k}_\perp$) is related to the angular wavevector by $\vec{k}_\perp = \vec{l}'/\chi$. Thus the Fourier transform of the HI signal in a frequency or redshift bin in the flat sky approximation is given by

$$\delta T_{bin}(\vec{l}) = \frac{1}{\Delta\tilde{\nu}} \int_{z_{min}}^{z_{max}} \frac{dz}{(1+z)^2} \frac{\bar{T}(z)}{\chi^2(z)} \int \frac{dk_\parallel}{2\pi} e^{ik_\parallel\chi} (b_{HI} + f\mu^2) \delta(k_\parallel\vec{m} + \vec{l}/\chi, z), \tag{4.14}$$

where $\delta$ is the dark matter density contrast.

### 4.1.4 HI Power Spectrum

The three-dimensional power spectrum of HI, defined at a given redshift by

$$\langle \delta T(\vec{k}) \delta T^*(\vec{k}') \rangle = (2\pi)^3 \delta_D^3((\vec{k} - \vec{k}') P^{HI}(\vec{k}, z) \tag{4.15}$$

is given by (Bull et al., 2015)

$$P^{HI}(\vec{k}, z) = \bar{T}^2(z)(b_{HI} + f\mu^2)^2 P^m(k, z) \tag{4.16}$$

where $P^m(k, z)$ is the dark matter power spectrum.

The multi-frequency angular power spectrum (taken between frequencies $\nu_1$ and $\nu_2$ separated by $\Delta\nu$) of the HI temperature fluctuations is given by (Bharadwaj and Ali, 2005; Datta et al., 2007)

$$C_l^{HI}(\nu_1, \nu_2) = \frac{\bar{T}(z_1)\bar{T}(z_2)}{\pi\chi_1\chi_2} \int_0^\infty dk_\parallel \cos(k_\parallel \Delta\chi) P^{HI}(k, z), \tag{4.17}$$

where $k = \sqrt{k_\parallel^2 + l^2/\chi^2}$. The cosine within the $k_\parallel$ integral reflects the fact that as the frequency difference increases, the HI signal between the two corresponding redshifts becomes less correlated, and the angular power is suppressed. Following Bharadwaj and Ali (2005), we can find the approximate frequency separation for which the signal becomes uncorrelated by considering how fast the HI power spectrum fall off with separation compared to the scales on which the cosine term completes an oscillation: the multifrequency angular power spectrum will only have an appreciable value if the power spectrum falls off faster than the cosine oscillates, otherwise the cosine factor will cause cancellations. The signal is correlated for comoving separations less than $\Delta\chi = \chi/u$, corresponding to frequency separations of $\Delta\nu = \chi/(\chi' u)$, where $\chi'$ denotes the derivative of the comoving distance with respect to frequency. For $\nu = 500$ MHz, the frequency separation after which the signal decorrelates is $\Delta\nu \sim 1.3$ MHz at $l \sim 600$ (Bharadwaj and Ali, 2005). It is important for experiments to use frequency channels smaller than this.

To obtain the angular power in a bin, the multi-frequency angular power spectrum is integrated over the bin (Loverde and Afshordi, 2008)

$$C_{l,bin}^{HI} = \int_{\nu_{min}}^{\nu_{max}} d\nu_1 F(\nu_1) \int_{\nu_{min}}^{\nu_{max}} d\nu_2 F(\nu_2) C_l^{HI}(\nu_1, \nu_2), \tag{4.18}$$

where $F = 1/\Delta\nu$ is the projection kernel weighting the contributions along the line of sight and normalising the resultant angular power. Thus the full expression for the angular power in a bin is given by

$$\begin{aligned} C_{l,bin}^{HI} = &\int_{bin} \frac{dz}{(1+z)^2} \frac{1}{\Delta\tilde{\nu}} \int_{bin} \frac{dz'}{(1+z')^2} \frac{1}{\Delta\tilde{\nu}'} \frac{\bar{T}(z)\bar{T}(z')}{\pi\chi\chi'} \times \\ &\int_0^\infty dk_\parallel \cos(k_\parallel(\chi - \chi'))(b_{HI} + f\mu^2)^2 P^m(k_\parallel \vec{m} + \vec{l}/\chi, z, z'). \end{aligned} \tag{4.19}$$

For a sufficiently large bin, integrating along the line of sight suppresses all except for small $k_\parallel$ modes, as higher $k_\parallel$ modes vary along the line of sight direction and thus cancel under integration. The expression for the angular power spectrum is therefore dominated by modes with $k \approx k_\perp$, allowing us to set $\mu \approx 0$ and remove $b_{HI}^2 P^m$ from the $k_\parallel$ integral, thus taking the Limber approximation (Limber, 1953; Kaiser, 1987; Loverde and Afshordi, 2008). We obtain

$$C_{l,limber}^{HI} = \int_{bin} \frac{dz}{(1+z)^2} \frac{1}{\Delta\tilde{\nu}} \frac{\bar{T}^2(z)}{\chi^2(z)} b_{HI}^2 P\left(\frac{l+1/2}{\chi}, z\right). \tag{4.20}$$

The Limber approximation holds for large $l$, or fluctuations on small angular scales, and wide bins (Valageas et al., 2011). We choose to use the full, general expression for the angular power spectrum from Equation (4.19).

The HI angular power spectrum for several bin sizes is shown in the left panel of Figure (4.1). The HI angular power spectra in this and later plots were calculated using a modified version of code developed by A Pénin. We used the following fiducial values for the cosmological parameters (Planck Collaboration et al., 2013): $h = 0.67$, $\Omega_\Lambda = 0.683$, $\Omega_b = 0.049$, $n_s = 0.962$, $\sigma_8 = 0.834$ and $N_{eff} = 3.04$, with $\Omega_K = 0$ and $w = -1$. Because we average the signal in each bin, the angular power spectrum does not change significantly with varying bin size. However, the amplitude of the angular power does drop slightly for larger bins, because the signal becomes less correlated and averages down. The signal is also shown for four 100 MHz bins at different redshifts in Figure (4.1). Again, in the redshift range we are considering (z=1.77 to 2.55) the signal does not change dramatically although bins at higher frequencies (lower redshift) have lower HI angular power spectra over most of their $l$ range. This is because the bias of HI is smaller at lower redshift (Padmanabhan et al., 2015a), and so the amplitude of the HI signal decreases with increasing frequency.

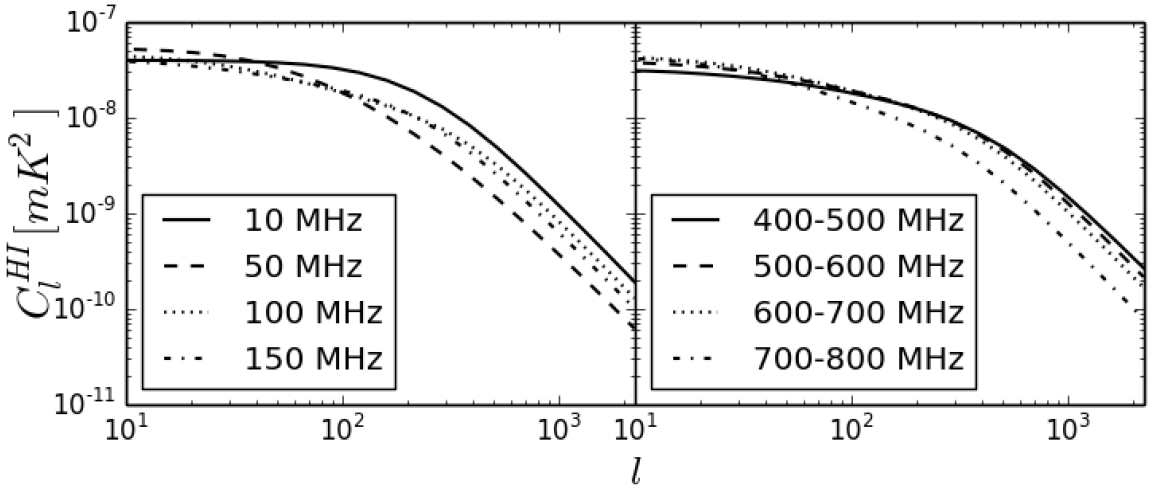


Figure 4.1: HI angular power spectrum for different bin sizes centred at z=1 (left) and for four 100MHz bins in the HIRAX redshift range (right).

### 4.1.5 Thermal Noise from HI Intensity Mapping

The HI intensity mapping signal can be observed using radio telescope arrays in interferometer or single dish mode. We evaluate the noise angular power spectrum using the specifications for HIRAX, given in Table (4.1) (HIRAX Collaboration, private communication). Although the total survey area of HIRAX should be about 25 000 square degrees, we consider a 10 000 square degree area that overlaps with CMB lensing data, giving $f_{sky} = S_{area}[\text{steradians}]/4\pi = 0.24$.

Table 4.1: HIRAX Specifications

| Quantity | Symbol | Value |
|---|---|---|
| System temperature | $T_{inst}$ | 50K |
| Number of dishes | $N_{dish}$ | 1024 |
| Dish diameter | $D_{dish}$ | 6m |
| Minimum frequency | $\nu_{min}$ | 400 MHz |
| Maximum frequency | $\nu_{max}$ | 800 MHz |
| Minimum redshift | $z_{min}$ | 0.77 |
| Maximum redshift | $z_{max}$ | 2.55 |
| Survey area | $S_{area}$ | 25 000 square degrees |
| Survey time | $t_{obs}$ | 2 years |

HIRAX will be used as a radio interferometer. Interferometers sample the visibility at different points on the $uv$ plane that correspond to the separation between each pair of antennas, known as the baseline. The visibility $V$ is related to the HI brightness temperature $\delta T(\hat{n})$ and the primary beam of the telescope $A(\hat{n})$ by (Zaldarriaga et al., 2004)

$$V(\vec{u}) = \frac{2k_B}{\lambda^2} \int d^2\vec{x} \delta T(\hat{n}) A(\hat{n}) e^{-2\pi i \vec{u}\cdot\vec{x}}. \tag{4.21}$$

The baseline $\vec{u}$ is related to the physical distance between two antenna $D$ and the wavelength of observation by $u = D/\lambda$, and $\vec{u}$ is related to the angular wavevector by $\vec{l} = 2\pi\vec{u}$.

The thermal noise from the detector for the real component of a visibility measurement, for

a single polarisation is given by (Thompson et al., 1986)

$$\sigma_{real} = \frac{\sqrt{2}k_B T_{sys}}{A_{eff}\sqrt{\delta\nu\delta t}}. \tag{4.22}$$

To obtain the noise for the complex visibility, the independent real and imaginary components of the noise can be combined in quadrature to give

$$\sigma = \sqrt{2}\sigma_{real} = \frac{2k_B T_{sys}}{A_{eff}\sqrt{\delta\nu\delta t}}. \tag{4.23}$$

The noise decreases as the square root of the number of samples, which is proportional to the product of the frequency channel width $\delta\nu$ and the correlation time for a single visibility $\delta t$. The system temperature $T_{sys} = T_{inst} + T_{sky}$ is the sum of instrumental and sky noise, with $T_{sky} = 60\text{K}\left(\frac{\nu}{300\text{MHz}}\right)^{-2.5}$. $A_{eff}$ is the effective area of the dish, and $\lambda$ is the wavelength of the observation.

For an interferometer, the noise for different baselines on the $uv$ plane will be uncorrelated, while the signal will be correlated for baselines with separations less than $\delta u = 1/\sqrt{FOV}$ (in units of wavelength) where the field of view is $FOV = \lambda^2/A_{eff}$. Averaging the signal over a resolution element in $uv$ space of area $\delta^2 u$ thus reduces the noise of the detection. The noise goes as $\sigma \propto 1/\sqrt{N(\vec{u})}$, where $N(\vec{u})$ is the number of baselines in the $uv$ element at the position $\vec{u}$. $N$ can be written in terms of the average number density of baselines, $N(\vec{u}) = n(\vec{u})\delta^2 u$. Sky rotation results in azimuthal symmetry in the $uv$ plane coverage, so $n(\vec{u}) = n(u)$ depends only on the magnitude of $u$. The average baseline density integrated over the $uv$ plane is normalised to give total number of baselines, $\int 2\pi u\, du\, n(u) = N_d(N_d - 1)/1$ where $N_d$ is the number of dishes. Therefore for a resolution element in the $uv$ plane of size $(\delta u)^2 = A_{eff}/\lambda$ and a pointing time $t_p$,

$$\sigma = \frac{2k_B T_{sys}}{A_{eff}\sqrt{\delta\nu\, t_p n(u)(\delta u)^2}}. \tag{4.24}$$

The square of the observed visibilities is related to the angular power spectrum by (Zaldarriaga et al., 2004)

$$\langle |V(\vec{u}|^2 \rangle = \left(\frac{2k_B}{\lambda^2}\right)^2 C_l^{HI} \int d^2\vec{u}' |A(\vec{u} - \vec{u}')|^2 \tag{4.25}$$

$$\approx \left(\frac{2k_B}{\lambda^2}\right)^2 C_l^{HI} \frac{1}{\delta^2 u}. \tag{4.26}$$

Using the fact that the average noise squared in each visibility is $\langle |N(\vec{u}|^2 \rangle = \sigma^2$, where $\sigma$ is given in Equation (4.23), the noise angular power for a single pointing is given by (Pourtsidou et al., 2015b)

$$C_l^N = \frac{T_{sys}^2 [FOV]^2}{\delta\nu \, t_p n(u)}. \tag{4.27}$$

For many pointings covering a total area $S_{area}$, the number of observed modes is increased by $S_{area}/FOV$ and the pointing time is related to the total observation time by $t_p = t_{obs} FOV/S_{area}$. Combining the frequency channels in a bandwidth $B$ gives $B/\delta\nu$ samples, and so the noise

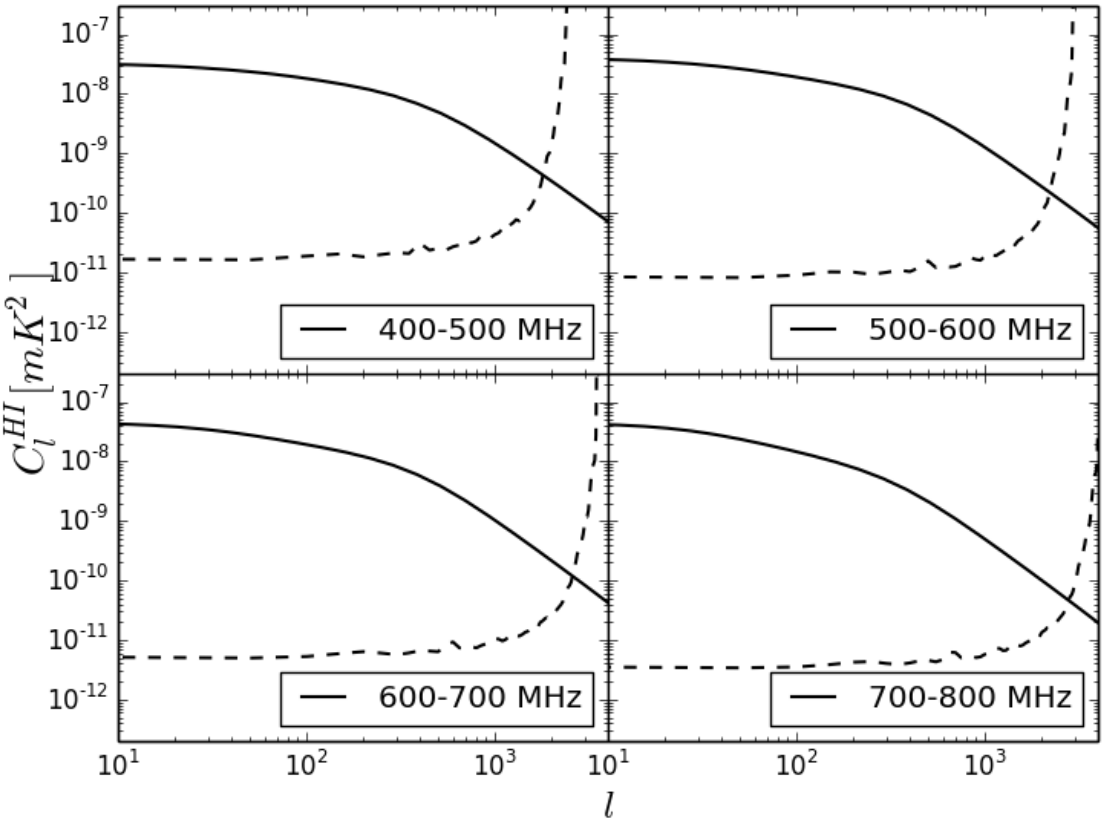


Figure 4.2: HI angular power spectrum (solid curve) and HIRAX noise angular power spectrum (dashed curve) for four 100MHz bins in the HIRAX redshift range.

becomes

$$\mathcal{N}_L^{HI} \equiv C_l^N = \frac{T_{sys}^2 [FOV]^2}{B t_{obs} n(u)}. \tag{4.28}$$

The HI angular power spectrum and noise are shown for four 100MHz bins in the HIRAX redshift range in Figure (4.2). For bins at higher frequencies (lower redshifts), the noise is lower and the beam is smaller, so the noise cutoff occurs at larger angular wavenumbers. We see that HIRAX will make a decisive detection of the signal, although a more realistic forecast of the HI angular power spectrum detection should include foreground residuals.

### 4.1.6 Foregrounds

The HI signal is buried within astrophysical foregrounds that are about six orders of magnitude larger than the signal (Shaw et al., 2015). Galactic synchrotron emission dominates the foregrounds at the relevant frequencies, and extragalactic points sources and bremsstrahlung also contaminate the signal (Santos et al., 2005). The challenging task of extracting the signal from the foregrounds is made possible by the differing behaviour of the HI signal and the foregrounds in frequency space. The foregrounds vary smoothly and gradually as a function of frequency, and they are therefore confined to low $k_\parallel$ modes. The HI signal, on the other hand, varies rapidly as a function of distance along the line of sight, and thus frequency, and so the HI signal is contained in higher $k_\parallel$ modes. We can thus remove the foregrounds and obtain the HI signal, at the expense of losing the low $k_\parallel$ modes (Zaldarriaga et al., 2004; Wang et al., 2006; McQuinn et al., 2006; Liu et al., 2009; Shaw et al., 2015).

We include the effect of foreground removal in our simulated angular power spectra by implementing a low $k_\parallel$ cutoff at $k_\parallel = k_{FG} \sim 1/(\chi \Delta\tilde{\nu})$ (Bull et al., 2015), neglecting all modes that vary on larger scales. This corresponds to around $k_{\parallel,min} = 0.007$h Mpc$^{-1}$ for a bin between 700 and 800 MHz, and is the theoretical minimum $k_\parallel$ attainable with foreground subtraction.

Two challenges in foreground removal are mode mixing, which converts angular structure into spectral structure due to the frequency dependence of the experiment's beam, and Faraday rotation of polarised foregrounds. Various foreground removal schemes have been developed to take mode mixing and polarised foregrounds into account, for example the Karhunen-

Loéve transform in the m-mode formalism developed for transit telescopes (Shaw et al., 2015). Following this treatment that includes more realistic sky and telescope simulations and signal reconstruction, the authors have found that the cutoff for $k_{\parallel}$ is somewhat higher, around $k_{\parallel,min} = 0.02$h Mpc$^{-1}$ (Shaw et al., 2015), which we also consider here.

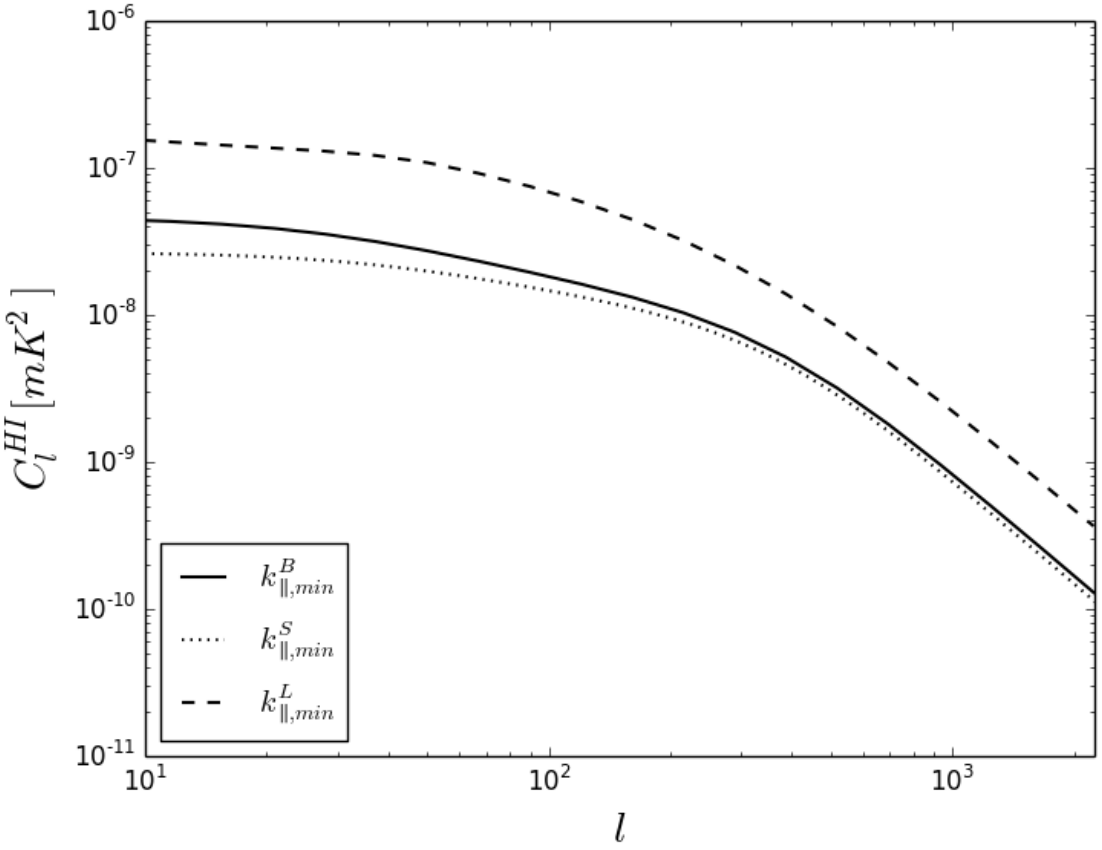


Figure 4.3: HI angular power spectrum showing the effect of varying $k_{\parallel,min}$ for a 100 MHz bin centred on $z = 1$.

We explore the effect of cutting out low $k_{\parallel}$ modes in Figure (4.3), which shows the angular power spectra for $k^B_{\parallel,min} = 1/(\chi\Delta\tilde{\nu})$ (Bull et al., 2015), $k^S_{\parallel,min} = 0.02$h Mpc$^{-1}$ (Shaw et al., 2015), which is larger than the Bull et al. expression for the bin widths plotted, and a low $k_{\parallel,min}$ corresponding to no foreground removal, $k^L_{\parallel,min} = 10^{-4}$h Mpc$^{-1}$. As expected, the signal decreases as more low $k_{\parallel}$ modes are removed, with the Bull et al. (2015) and Shaw et al. (2015)

cutoffs yielding similar results, although the larger $k^S_{\parallel,min}$ results in a slightly smaller angular spectrum.

In all plots in this chapter in which $k_{\parallel,min}$ is unspecified, we have used the low $k_\parallel$ cutoff from Bull et al. (2015), as well as their suggested high $k_\parallel$ cutoff at $k_\parallel = 0.15\text{Mpc}^{-1}$, which is due to information on small scales being smeared out as a result of nonlinear velocities.

We have considered the ideal case in which foregrounds are removed completely. In reality foreground residuals contaminate the signal (Santos et al., 2005). We postpone a more complete foreground treatment that includes the effects of residual foregrounds to future work.

### 4.1.7 HI Signal to Noise

The error in estimating the angular power spectrum at a given $l$ is given by (Kesden et al., 2003)

$$\sigma^{HI} = \frac{C_l^{HI} + \mathcal{N}_l^{HI}}{\sqrt{N_{modes}}}, \tag{4.29}$$

where $N_{modes}$ is the number of modes in an annulus centred on $l$. In the flat sky approximation,

$$N_{modes} = 2l\Delta l f_{sky}. \tag{4.30}$$

The HI signal to noise is therefore given by

$$\frac{S}{N} = \frac{\sqrt{N_{modes}}}{C_l^{HI} + \mathcal{N}_l^{HI}} C_l^{HI}. \tag{4.31}$$

The HI signal to noise is shown for different bin sizes in the top left panel of Figure (4.4), using the Bull et al. $k_\parallel$ cutoffs described above (Bull et al., 2015). The signal to noise improves somewhat for larger individual frequency bins, mainly because the thermal noise is reduced as the bandwidth increases. However, combining many smaller bins, for example taking ten 10 MHz bins instead of one 100 MHz bin over the same frequency range, would increase the total HI signal over that from just integrating over the 100 MHz bin. The signal to noise is also shown for four bins at different redshifts within the HIRAX redshift range in the top right panel of Figure (4.4). It is clear that bins at higher frequencies have larger signal to noise, especially on smaller angular scales because of the improved angular resolution with increasing frequency.

The bottom panels show the cumulative signal to noise, obtained from combining the different $l$ modes in quadrature. HIRAX will detect the HI intensity mapping angular power spectrum at high significance with a cumulative signal to noise of 800 - 1000, and will be able to constrain standard cosmological parameters such as the dark energy fraction and the Hubble parameter, as well as extensions to the standard model such as the dark energy equation of state and the geometry of the universe (Bull et al., 2015).

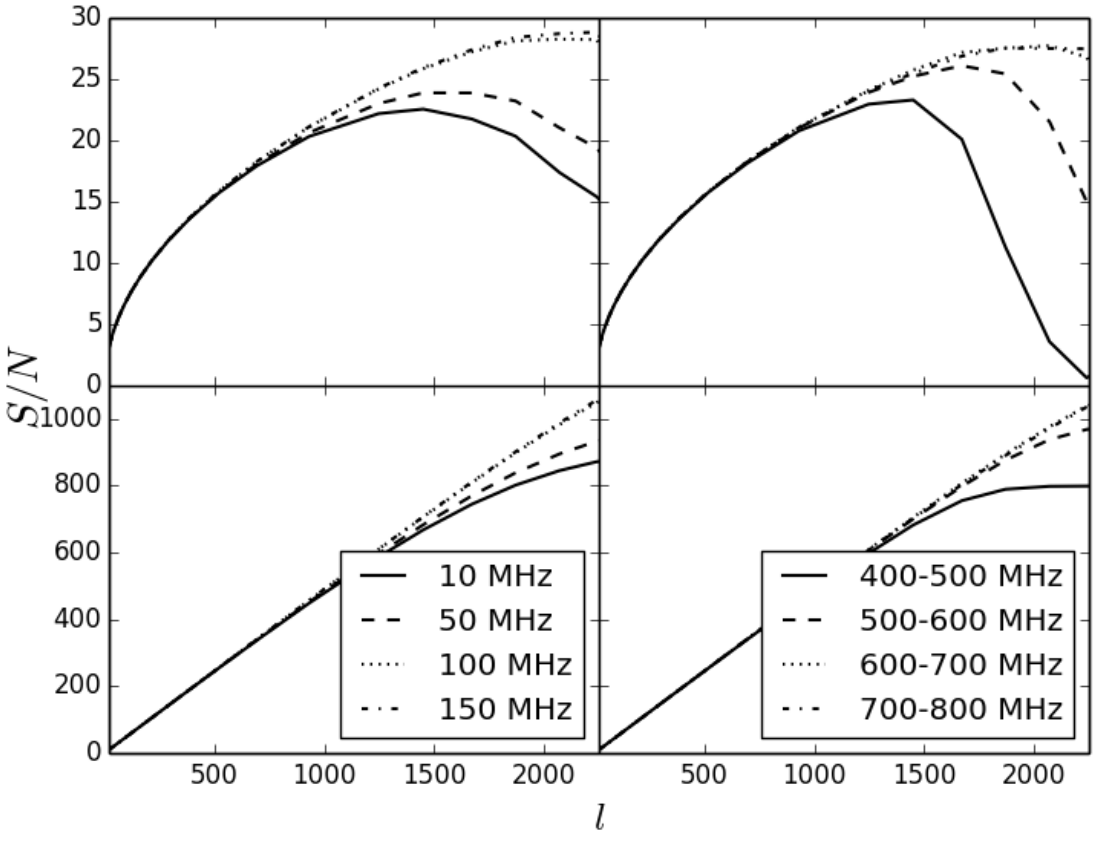


Figure 4.4: HI signal to noise for single bins of varying width centred at z=1 (left) and for four 100MHz bins in the HIRAX redshift range (right). The top panels show the signal to noise and the bottom panels show the cumulative signal to noise.

## 4.2 CMB Lensing Convergence

The CMB lensing signal is discussed in detail in Chapter 3. In this section we present an overview of the CMB lensing convergence signal and noise expressions needed to evaluate the theoretical cross-correlation between HI intensity mapping and CMB lensing.

### 4.2.1 Lensing Signal

The CMB lensing convergence $\kappa$ is a weighted projection of the dark matter overdensity $\delta$ (Bartelmann and Schneider, 2001):

$$\kappa(\hat{n}) = \int_0^{z_*} dz W^\kappa(z) \delta(\chi(z)\hat{n}, z) \tag{4.32}$$

where $z_*$ denotes the redshift of the last scattering surface and the CMB lensing kernel is given by

$$W^\kappa(z) = \frac{3}{2}\Omega_m H_0^2 \frac{1+z}{H(z)} \frac{\chi(z)}{c} \frac{\chi(z_*) - \chi(z)}{\chi(z_*)} \tag{4.33}$$

The lensing kernel is shown in Figure (4.5). It peaks at redshifts of around $z = 1$ to $z = 2$, which overlaps significantly with the redshift range which will be probed by HIRAX, $z = 0.77$ to $z = 2.55$, making CMB lensing ideal for cross-correlation with HIRAX's HI intensity mapping signal.

The lensing convergence in harmonic space in the flat sky approximation is

$$\kappa(\vec{l}) = \int d^2\vec{x} e^{-i\vec{l}\cdot\vec{x}} \kappa(\hat{n}) \tag{4.34}$$

$$= \int_0^{z_*} dz \frac{W^\kappa(z)}{\chi^2(z)} \int \frac{dk_\parallel}{2\pi} e^{ik_\parallel \chi} \delta(k_\parallel \vec{m} + \vec{l}/\chi, z) \tag{4.35}$$

The CMB lensing convergence angular power spectrum is given, in the Limber approximation by

$$C_l^\kappa = \int_0^{z_*} dz \frac{H(z)}{c} \frac{\left(W^\kappa(z)\right)^2}{\chi^2(z)} P\left(\frac{l+1/2}{\chi}, z\right). \tag{4.36}$$

We use the Limber approximation here because the redshift range we integrate over is very large, and so the Limber approximation holds for a wide range of scales. The lensing convergence power spectrum is shown in Figure (4.6)

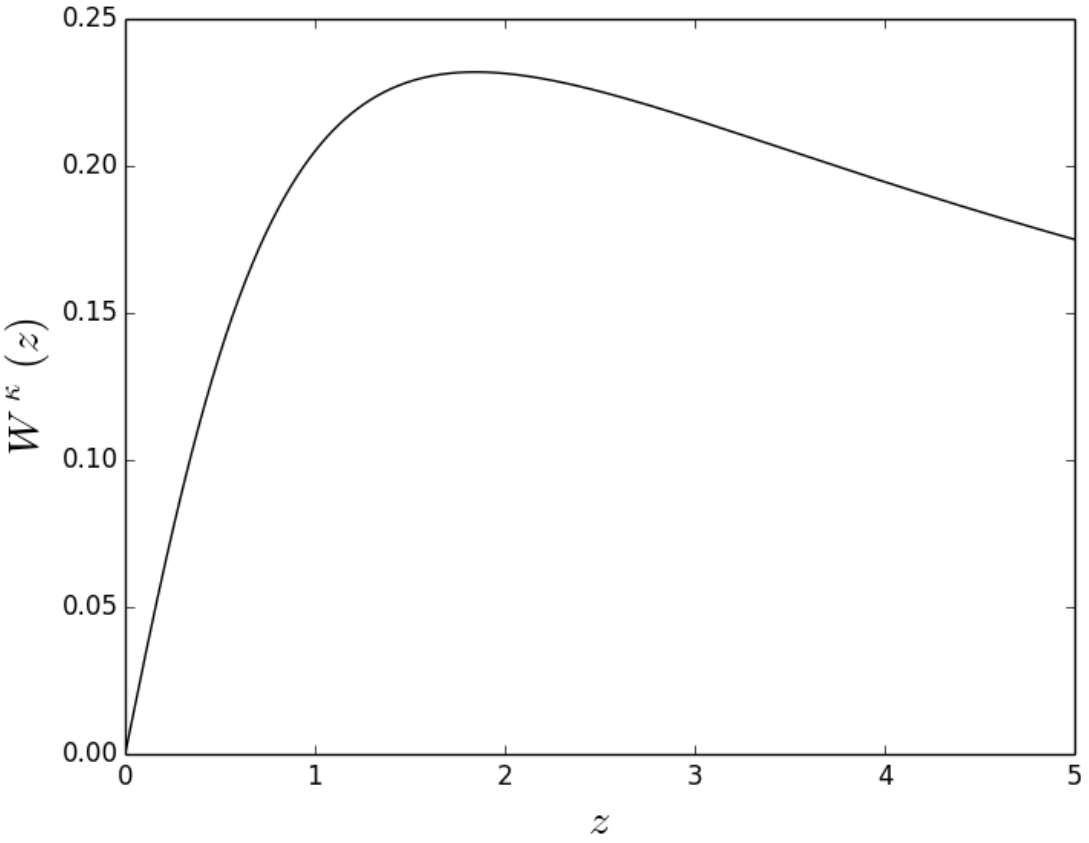


Figure 4.5: The CMB lensing kernel.

### 4.2.2 Lensing Reconstruction Noise

In harmonic space, the minimum variance estimator for the lensing potential (Hu and Okamoto, 2002) is given by Equation (3.37)

$$\hat{\psi}^{XY}(\vec{L}) = \frac{1}{N^{XY}(\vec{L})} \int \frac{d^2\vec{l}}{(2\pi)^2} \tilde{X}(\vec{L}-\vec{l})\tilde{Y}^*(\vec{l}) g^{XY}(\vec{l},\vec{L})\,, \tag{4.37}$$

where $XY$ denotes the combination of temperature and polarisation used for the reconstruction. The normalisation factor is given by

$$N^{XY}(\vec{L}) = \int \frac{d^2\vec{l}}{(2\pi)^2} f_{XY}(\vec{l},\vec{L}) g^{XY}(\vec{l},\vec{L}), \tag{4.38}$$

and it ensures that the estimator is unbiased, or $\langle\hat{\psi}(\vec{L})\rangle_{CMB} = \psi(\vec{L})$. The lensing potential power spectrum from this estimator has a noise term

$$\langle\hat{\psi}(\vec{L})\hat{\psi}^*(\vec{L}')\rangle = (2\pi)^2\delta_D^2(\vec{L}-\vec{L}')(C_L^\psi + \mathcal{N}_L^\psi). \tag{4.39}$$

To zeroth order in the lensing potential, the noise of the reconstruction is given by the inverse of the normalisation factor $\mathcal{N}_L^\psi = \frac{1}{N^{XY}(\vec{L})}$ (Hu and Okamoto, 2002; Kesden et al., 2003)

The convergence is related to the lensing potential by

$$\kappa(\vec{L}) = \frac{1}{2}L^2\psi(\vec{L}), \tag{4.40}$$

so the convergence noise is given by

$$\langle\hat{\kappa}(\vec{L})\hat{\kappa}^*(\vec{L}')\rangle = (2\pi)^2\delta_D^2(\vec{L}-\vec{L}')(C_L^\kappa + \mathcal{N}_L^\kappa) \tag{4.41}$$

$$= (2\pi)^2\delta_D^2(\vec{L}-\vec{L}')(C_L^\kappa + \frac{L^4}{4}\mathcal{N}_L^\psi), \tag{4.42}$$

so the lensing convergence noise is related to the normalisation factor in Equation (4.38) by

$$\mathcal{N}_L^\kappa = \frac{L^4}{4}\frac{1}{N^{XY}(\vec{L})}. \tag{4.43}$$

The $EB$ reconstruction noise gives the best reconstruction for experiments with high resolution and sensitivity (Hu and Okamoto, 2002). The reconstruction noise for an AdvACT-like experiment with specifications given in Table (3.3) is shown in Figure (4.6), together with the lensing convergence angular power spectrum. A southern sky survey is planned for AdvACT, which will overlap with the region of the sky surveyed by HIRAX. We conservatively assume a 10 000 square degree overlap.

Kesden et al. (2003) show that there is an additional noise term of first order in $C_L^\phi$, because of the noise contributions of other lensing modes to the $\vec{L}$ mode reconstruction.This higher order noise becomes more important as experimental resolution and sensitivity improve, but it will still be an order of magnitude below the zeroth order noise term for the AdvACT experiment, so we neglect it here.

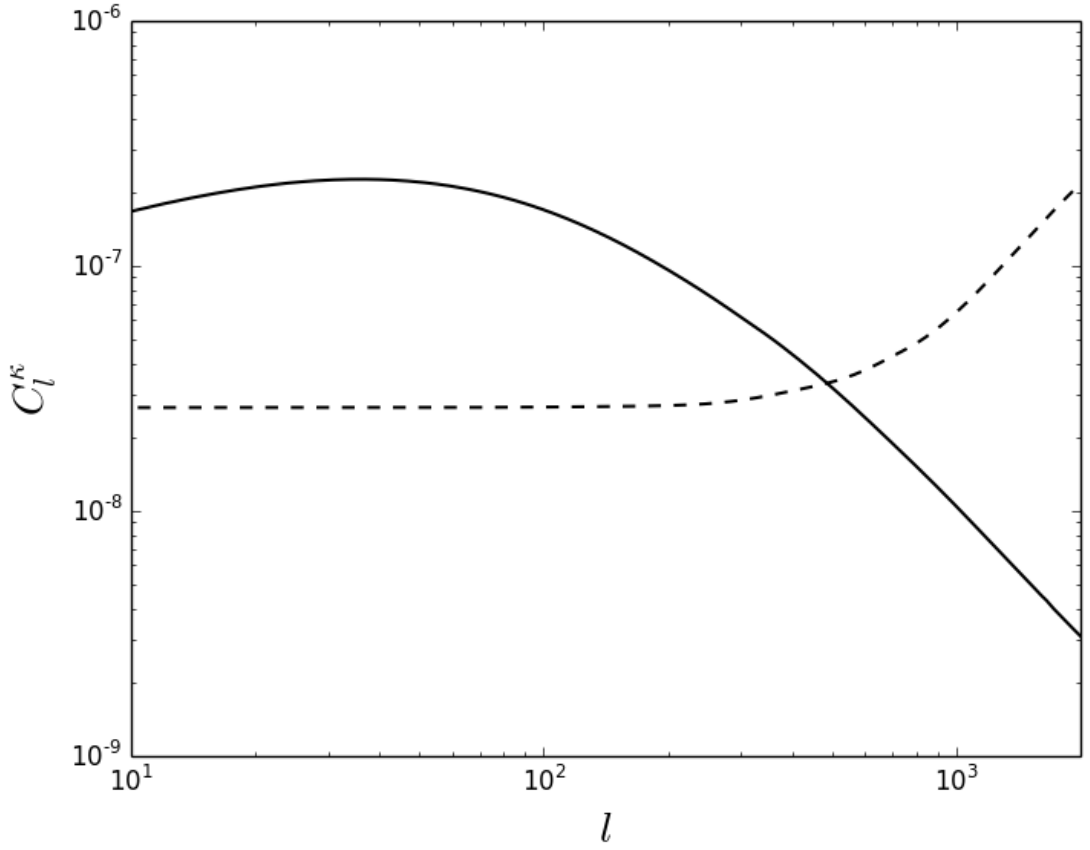


Figure 4.6: The CMB lensing convergence angular power spectrum (solid curve) and noise (dashed curve). The angular power spectrum was computed using CAMB (Lewis and Challinor, 2011).

## 4.3 Cross-Correlation of CMB Lensing with HI Intensity Mapping

We now explore the theoretical cross-correlation between the lensing convergence and the HI temperature contrast.

### 4.3.1 Cross-Correlation Angular Power Spectrum

The cross-correlation between the convergence from CMB lensing and the temperature fluctuations from HI intensity mapping is obtained from Equations (4.19) and (4.35) to be

$$\begin{aligned}\langle \delta T(\vec{l})\kappa^*(\vec{l}')\rangle =& \frac{1}{\Delta\tilde{\nu}}\int_{z_{min}}^{z_{max}} \frac{dz}{(1+z)^2}\frac{\bar{T}(z)}{\chi^2(z)}\int_0^{z_*} dz' \frac{W^\kappa(z')}{\chi^2(z')}\times \\ &\times \int \frac{dk_\parallel}{2\pi}\int \frac{dk'_\parallel}{2\pi} e^{i(k_\parallel \chi - k'_\parallel \chi')}(b_{HI}+f\mu^2)\langle \delta(k_\parallel \vec{m}+\vec{l}/\chi, z)\delta(k'_\parallel \vec{m}+\vec{l}'/\chi', z')\rangle\end{aligned} \tag{4.44}$$

The dark matter power spectrum at a given wavenumber $k$ between two different redshifts is

$$\langle \delta(\vec{k}, z)\delta(\vec{k}', z')\rangle = (2\pi)^3\delta_D^3(\vec{k}-\vec{k}')P^m(\vec{k}, z, z') \tag{4.45}$$

so our expression for the cross-correlation becomes

$$\begin{aligned}\langle \delta T(\vec{l})\kappa^*(\vec{l}')\rangle =& \frac{1}{\Delta\tilde{\nu}}\int_{z_{min}}^{z_{max}} \frac{dz}{(1+z)^2}\frac{\bar{T}(z)}{\chi^2(z)}\int_0^{z_*} dz' \frac{W^\kappa(z')}{\chi^2(z')}\times \\ &\times \int \frac{dk_\parallel}{2\pi} e^{ik_\parallel(\chi-\chi')}(b_{HI}+f\mu^2)P^m(k_\parallel \vec{m}+\vec{l}/\chi, z, z')(2\pi)^2\delta_D^2\left(\frac{\vec{l}}{\chi}-\frac{\vec{l}'}{\chi'}\right).\end{aligned} \tag{4.46}$$

The HI signal in a given bin should only be correlated with the CMB lensing due to matter within the HI bin, and random correlations from outside the bin should average down in the signal, although they will contribute to the noise. We therefore assume that the cross-correlation is negligible outside the HI bin. We also take bins small enough that $\chi \approx \chi'$, giving

$$\delta_D^2(\vec{k}_\perp - \vec{k}'_\perp) = \delta_D^2\left(\frac{\vec{l}-\vec{l}'}{\chi}\right) \approx \chi\chi'\delta_D^2(\vec{l}-\vec{l}'). \tag{4.47}$$

Under these assumptions, the cross-correlation becomes

$$\begin{aligned}\langle \delta T(\vec{l})\kappa^*(\vec{l}')\rangle =& \frac{1}{\Delta\tilde{\nu}}\int_{z_{min}}^{z_{max}} \frac{dz}{(1+z)^2}\frac{\bar{T}(z)}{\chi(z)}\int_{z_{min}}^{z_{max}} dz' \frac{W^\kappa(z')}{\chi(z')}\times \\ &\times \int \frac{dk_\parallel}{2\pi} e^{ik_\parallel(\chi-\chi')}(b_{HI}+f\mu^2)P^m(k_\parallel \vec{m}+\vec{l}/\chi, z, z')(2\pi)^2\delta_D^2(\vec{l}-\vec{l}')\end{aligned} \tag{4.48}$$

which gives

$$C_{l,bin}^{HI-\kappa} = \frac{1}{\Delta\tilde{\nu}} \int_{z_{min}}^{z_{max}} \frac{dz}{(1+z)^2} \frac{\bar{T}(z)}{\chi(z)} \int_{z_{min}}^{z_{max}} dz' \frac{W^{\kappa}(z')}{\chi(z')} \int \frac{dk_{\parallel}}{2\pi} e^{ik_{\parallel}(\chi-\chi')} (b_{HI} + f\mu^2) P^m(k_{\parallel}\vec{m} + \vec{l}/\chi, z, z'). \tag{4.49}$$

The amplitude of the cross-correlation increases as the bandwidth increases, as shown in the left panel of Figure (4.7), because there is a larger overlap between the HI bin and the lensing kernel. The four 100 MHz bins in the HIRAX redshift range have similar signals, as can be seen in the right panel of Figure (4.7). The lowest redshift bin ($\nu$=700 - 800 MHz) has a smaller cross-correlation amplitude than the other bins because this bin corresponds to $z = 0.78$ to $z = 1.03$, where the lensing kernel is smallest (see Figure (4.5)). The cross-correlation angular power spectra in this and later plots were calculated using a modified version of code developed by A Pénin.

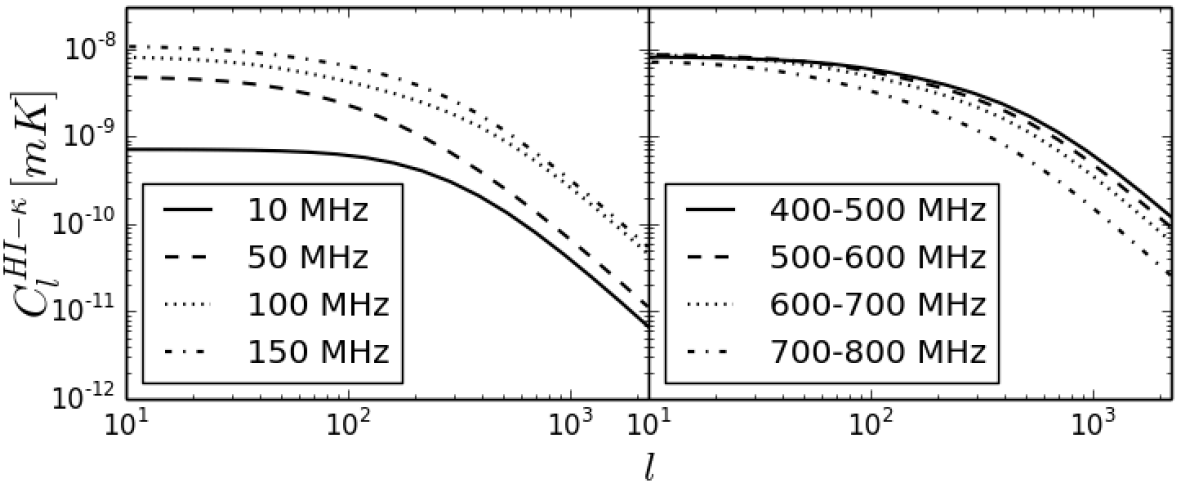


Figure 4.7: Cross-correlation signal for different bin sizes centred at z=1 (left) and for four 100MHz bins in the HIRAX redshift range (right), using the $k_{\parallel,min}^{B}$ cutoff from Bull et al. (2015).

### 4.3.2 Cross-Correlation Noise

The CMB lensing–HI cross spectrum in an annulus in Fourier space is given by

$$C_L^{HI-\kappa} = \frac{1}{N_{modes}} \int_{a_L} d^2\vec{l}\kappa_{CMB}^{*}(\vec{l})\delta T(\vec{l}) \tag{4.50}$$

where $a_L$ is the annulus in which we measure the power and $N_{modes}$ is the number of individual modes that are in the annulus and therefore contribute to the angular power spectrum. The number of modes is given by

$$N_{modes} = \frac{2\pi L \Delta L}{(2\pi)^2/S_{area}} = 2L\Delta L f_{sky} \tag{4.51}$$

where $(2\pi)^2/S_{area}$ is the area of an individual mode in $\vec{L}$ space and $S_{area}$ is the size of the survey.

The variance of the cross power spectrum is

$$\sigma^2_{C_L^{HI-\kappa}} = \langle (C_L^{HI-\kappa})^2 \rangle - \langle C_L^{HI-\kappa} \rangle^2, \tag{4.52}$$

where the first term is

$$\begin{aligned}
\langle (C_L^{HI-\kappa})^2 \rangle =& \frac{1}{N^2_{modes}} \int_{a_L} d^2\vec{l} \int_{a_L} d^2\vec{l'} \langle \kappa^*(\vec{l}) \delta T(\vec{l}) \kappa^*(\vec{l'}) \delta T(\vec{l'}) \rangle \\
=& \frac{1}{N^2_{modes}} \int_{a_L} d^2\vec{l} \int_{a_L} d^2\vec{l'} \langle \kappa^*(\vec{l}) \delta T(\vec{l}) \rangle \langle \kappa^*(\vec{l'}) \delta T(\vec{l'}) \rangle + \langle \kappa^*(\vec{l}) \delta T(\vec{l'}) \rangle \langle \kappa^*(\vec{l'}) \delta T(\vec{l}) \rangle + \\
&+ \langle \kappa^*(\vec{l}) \kappa^*(\vec{l'}) \rangle \langle \delta T(\vec{l}) \delta T(\vec{l'}) \rangle \\
=& \frac{1}{N^2_{modes}} \left[ \int_{a_L} d^2\vec{l} \int_{a_L} d^2\vec{l'} C_l^{HI-\kappa} C_{l'}^{HI-\kappa} + \int_{a_L} d^2\vec{l} \left( (C_l^{HI-\kappa})^2 + C_l^{\kappa,tot} C_l^{HI,tot} \right) \right],
\end{aligned} \tag{4.53}$$

with the total convergence and HI angular power given by

$$C_l^{\kappa,tot} = C_l^{\kappa} + \mathcal{N}_l^{\kappa} \tag{4.54}$$

$$C_l^{HI,tot} = C_l^{HI} + \mathcal{N}_l^{HI}. \tag{4.55}$$

We include the noise in the total angular power as $\kappa$ and $\delta T$ are noisy experimental quantities. We assume that the lensing reconstruction noise and the HI noise are uncorrelated so that $C_l^{HI-\kappa}$ is not biased. The HI noise $\mathcal{N}_l^{HI}$ is the thermal noise angular power spectrum from Equation (4.28).

The second term in the variance expression of Equation (4.52) is given by

$$\langle C_L^{HI-\kappa} \rangle^2 = \frac{1}{N^2_{modes}} \int_{a_L} d^2\vec{l} \int_{a_L} d^2\vec{l'} C_l^{HI-\kappa} C_{l'}^{HI-\kappa}, \tag{4.56}$$

which cancels with the first term of Equation (4.53), so that the variance is given by

$$\sigma^2_{C_L^{HI-\kappa}} = \frac{1}{N^2_{modes}} \int_{a_L} d^2\vec{l} \Big( (C_l^{HI-\kappa})^2 + C_l^{\kappa,tot} C_l^{HI,tot} \Big) . \tag{4.57}$$

Assuming that the expression in the integral is approximately constant over the annulus, we can evaluate it at the central $l$ value of the annulus and remove it from the integral. We then integrate over the annulus, obtaining its area. This cancels with one of the $N_{modes}$ factors, giving

$$\sigma^2_{C_L^{HI-\kappa}} = \frac{1}{N_{modes}} \Big( (C_L^{HI-\kappa})^2 + C_L^{\kappa,tot} C_L^{HI,tot} \Big) \tag{4.58}$$

or

$$\sigma_{C_L^{HI-\kappa}} = \sqrt{\frac{(C_L^{HI-\kappa})^2 + (C_L^{\kappa} + \mathcal{N}_L^{\kappa})(C_L^{HI} + \mathcal{N}_L^{HI})}{N_{modes}}}. \tag{4.59}$$

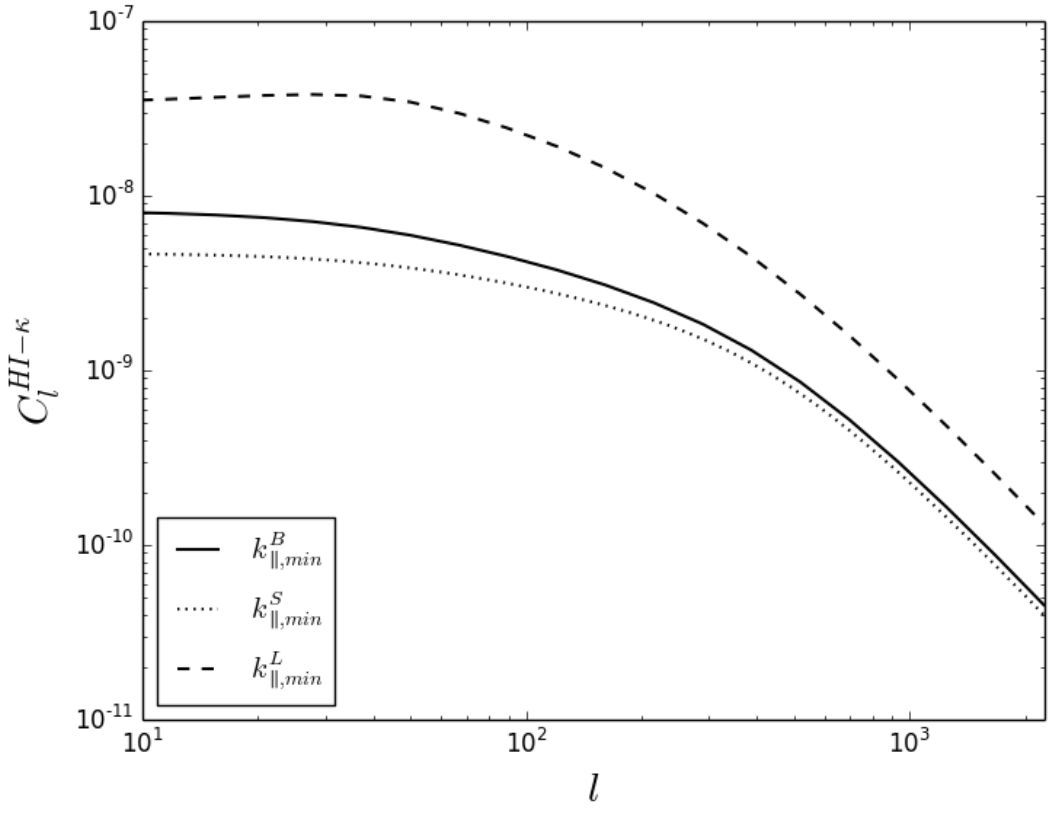


Figure 4.8: Cross-correlation angular power spectrum showing the effect of varying $k_{\parallel,min}$ for a 100MHz bin centered on $z = 1$

Figure (4.8) shows the effect of reducing $k_{\parallel,min}$ in a 100 MHz bin centred on $z = 1$, resulting in the amplitude of the cross-correlation increasing by almost an order of magnitude. Therefore if galactic foregrounds in the HI intensity mapping data could be removed on large scales along the line of sight (low $k_{\parallel}$), or if these HI modes could be reconstructed, the cross-correlation signal would be significantly enhanced. Zhu et al. (2015) discuss the possibility of using the cosmic tidal reconstruction method to recover the long wavelength radial modes and thus increase the cross-correlation signal. The cross-correlation signal and noise are shown for four 100 MHz bins in Figure (4.9), using the $k^B_{\parallel,min}$ cutoff from the HI foregrounds discussed in Section 4.1.6 (Bull et al., 2015). The detection for an individual $l$ mode is marginal, so accessing lower $k_{\parallel}$ modes would be highly beneficial.

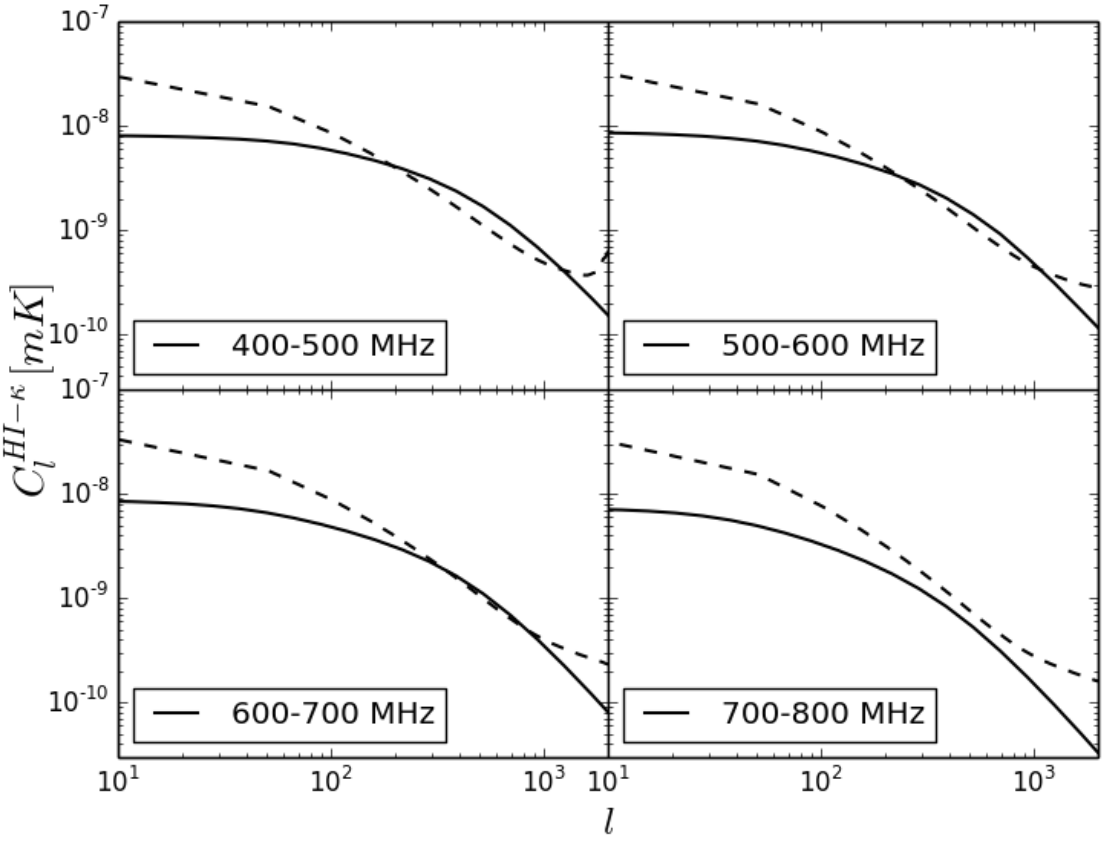


Figure 4.9: Cross-correlation signal and noise for four 100MHz bins in the HIRAX redshift range, using the $k^B_{\parallel,min}$ cutoff from Bull et al. (2015).

### 4.3.3 Cross-Correlation Signal to Noise

We can use the expressions for the cross-correlation angular power spectrum and noise to find the signal to noise ratio in a given annulus:

$$\frac{S}{N} = \frac{C_L^{HI-\kappa}}{\sigma_{C_L^{HI-\kappa}}} = C_L^{HI-\kappa} \sqrt{\frac{N_{modes}}{(C_L^{HI-\kappa})^2 + (C_L^{\kappa} + \mathcal{N}_L^{\kappa})(C_L^{HI} + \mathcal{N}_L^{HI})}}. \tag{4.60}$$

The signal to noise is shown in the top panel of Figure (4.10). Larger bins have lower noise and higher signal than smaller bins, and thus result in higher signal to noise, as shown in the left panel. Unlike in the case of the HI autocorrelation discussed in Section 4.1.7, dividing larger

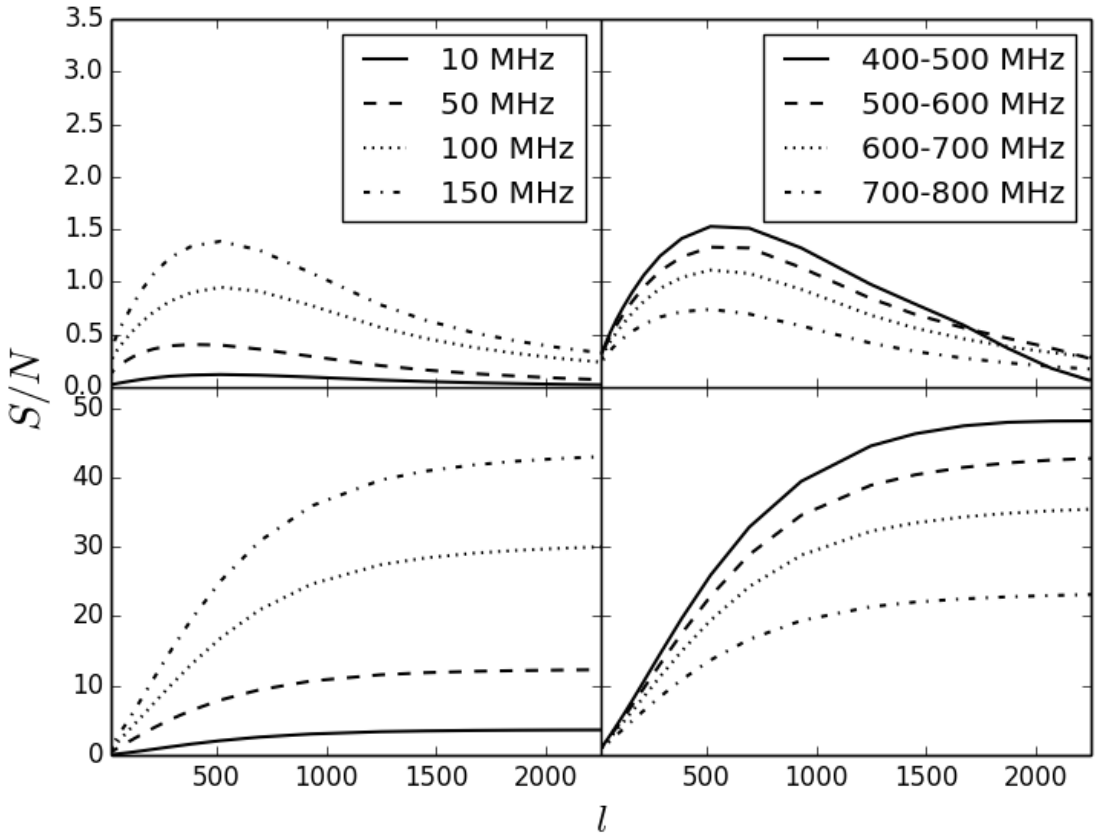


Figure 4.10: Cross-correlation signal to noise for different bin sizes centred at z=1 (left) and for four 100MHz bins in the HIRAX redshift range (right). The top panel shows the signal to noise while the bottom panel shows the cumulative signal to noise. The $k^B_{\parallel,min}$ cutoff from Bull et al. (2015) has been used.

(100 MHz, for example) frequency bins into multiple smaller bins (such as ten 10 MHz bins) offers no signal to noise advantage, as the small overlap between the HI bin and CMB lensing kernel results in the signal to noise ratio for smaller bins being significantly suppressed.

The signal to noise for individual $l$ modes is not highly significant, but we can add the contributions from different annuli in $l$ space in quadrature to obtain the cumulative signal to noise, shown in the bottom panel of Figure (4.10). We find that a significant statistical detection of the cross-correlation will be possible, with a total signal to noise of between 20 and 50 for the four 100 MHz bins, shown in the bottom right panel of Figure (4.10). The cross-correlation signal to noise is smaller where the lensing kernel is smaller. For the four bins in the HIRAX redshift range, this occurs for the $\nu$ =700-800 MHz bin as discussed above. We chose to use these four bins to balance the requirements of having sufficiently large bins to obtain a significant detection of the cross-correlation in each bin, while having multiple bins to study the cross-correlation over a range of redshifts. We expect that the overall signal to noise will be reduced somewhat once foreground residuals are included in our treatment, which will be taken into account in our forthcoming paper.

### 4.3.4 Constraints from the Lensing-HI Cross-Correlation

The cross-correlation between CMB lensing and HI intensity mapping can be used to constrain the HI bias and density parameter in the four different redshift bins via the product $\Omega_{HI}b_{HI}$. Because of the large cumulative signal to noise of the cross-correlation detection, the cross-correlation signal can also be detected at reasonable significance in different $l$ bins to investigate the scale dependence of the bias in addition to its redshift evolution. We can quantify the constraints that can be placed on $\Omega_{HI}b_{HI}$ using the Fisher matrix forecasting formalism. These constraints will be presented in future work.

# CHAPTER 5

# Conclusion

*Gravity is a habit that is hard to shake off.*

– Terry Pratchett

The standard ΛCDM cosmological model describes a universe dominated by dark energy and dark matter, and characterised by just six cosmological parameters. CMB observations (Spergel et al., 2003; Planck Collaboration et al., 2015c), large-scale structure surveys (e.g. Eisenstein et al., 2005; Reid et al., 2010) and type Ia supernovae observations (Perlmutter et al., 1999; Riess et al., 1998, 2007) have informed the standard model and placed precise constraints on the model parameters. Upcoming experiments such as Euclid (Laureijs et al., 2011), the Large Synoptic Survey Telescope (Ivezic et al., 2008) and the Square Kilometer Array (Maartens et al., 2015) will survey larger volumes of the universe than ever before, and will have the potential to place even more precise constraints on the cosmological parameters, as well as to further test the validity of the standard model and possibly discover as yet unthought of physics.

The cosmic microwave background anisotropies are caused by small spatial variations in the matter density at early times. These perturbations seeded the formation of large-scale structure:

slight overdensities grew into larger structures as they attracted matter from underdense regions. The observed CMB contains secondary anisotropies caused by interactions of CMB photons with the large-scale structure as they travel from the surface of last scattering. One of the ways that large-scale structure interacts with CMB photons is by gravitational lensing–the deflection of photons as they pass massive objects. Gravitational lensing is sensitive to the total matter distribution, and can thus be used to probe dark matter, which dominates the matter density. We described the standard model of cosmology in Chapter 2, including the growth of large-scale structure, the primordial CMB, and the effect of gravitational lensing.

Most methods of reconstructing the gravitational lensing potential make use of harmonic space lensing estimators. Real space estimators implemented locally in map space could prove advantageous for CMB observations, which have point source excisions and non-uniform sky coverage, making it difficult to accurately obtain harmonic space quantities. As the sensitivity and resolution of CMB experiments continues to improve, the least noisy CMB lensing reconstructions will come from polarisation (Hu and Okamoto, 2002). In Chapter 3, we extended an existing real space lensing estimator based on CMB temperature maps (Bucher et al., 2012) to CMB polarisation, and showed that this estimator can be obtained from the standard harmonic space estimator in the large-scale lensing field approximation. We then explored the validity of this approximation, studying which angular scales contribute the most statistical weight to the estimators. We investigated the effect of the large-scale lensing field (squeezed triangle) approximation on the lensing reconstruction, showing that the real space reconstruction amplitude is accurate on large scales, but not on small scales. We calculated how the reconstruction amplitude varies with angular wavenumber, which can be used to correct the power of the reconstruction at the expense of an increase in the variance. We found that reconstructions from the high resolution and sensitivity AdvACT experiment are more accurate out to smaller scales than an experiment with Planck noise. We also noted that the TT and EB estimators are less negatively affected by this modulation of reconstructed power with scale than the other estimators, offering the most promising real space reconstructions. The real space estimators are implemented using a real space kernel which is convolved with the CMB map. We showed that these kernels are limited in spatial extent, and can therefore be applied locally to small regions of a CMB map. In future

work, we plan to develop alternative real space estimators that provide accurate reconstructions over a wide range of scales by applying two reconstruction kernels to the lensing map.

We tested the real space estimators that we developed on simulated lensed CMB maps, finding that on large scales the reconstructed lensing field agrees with the input lensing field, although the reconstruction has noise contributions from the unlensed map. The EB estimator reconstruction is in excellent agreement with the actual lensing field, because there is no cosmic variance from primordial B modes, which are expected to be very small. This illustrates the value of developing polarisation estimators. The results from this study will be published in a forthcoming paper, currently in preparation (Prince et al., 2016a). The next step in this research programme is to apply these estimators to experimental CMB maps to reconstruct the actual lensing convergence and shear, and thus to probe the matter distribution.

In Chapter 4 we investigated what could be learned from combining CMB lensing reconstructions with intensity maps of the neutral hydrogen distribution. Neutral hydrogen (HI) is a biased tracer of the dark matter distribution. HI can be observed via the redshifted 21 cm radiation that it emits, which can be used to map the distribution of neutral hydrogen over a wide range of redshifts. The technique of HI intensity mapping, in which the integrated signal from many HI galaxies within a 3D pixel is detected, provides a way to rapidly map the HI throughout large volumes of the universe without requiring high resolution experiments. HI intensity mapping can be used to probe the expansion history and geometry of the universe by measuring the baryon acoustic oscillation scale at different redshifts.

Cross-correlating HI intensity mapping with CMB lensing would allow us to place constraints on the clustering of HI relative to the underlying dark matter field. We found that CMB lensing reconstructed from AdvACT data (Henderson et al., 2015) and post-reionisation HI intensity mapping data from HIRAX (HIRAX Collaboration, 2016) would allow us to detect the cross-correlation with a cumulative signal to noise ratio of between 20 and 50 for each of four bins in the HIRAX redshift range. Such a detection of the cross-correlation could be used to constrain the HI bias over a range of redshifts and scales. In a forthcoming paper, we will present forecasts of constraints on the HI bias and density parameter from this cross-correlation (Prince et al., 2016b).

# CHAPTER 6

# Bibliography

Ade, P. A. R., Akiba, Y., Anthony, A. E., Arnold, K., Atlas, M., Barron, D., Boettger, D., Borrill, J., Chapman, S., Chinone, Y., Dobbs, M., Elleflot, T., Errard, J., Fabbian, G., Feng, C., Flanigan, D., Gilbert, A., Grainger, W., Halverson, N. W., Hasegawa, M., Hattori, K., Hazumi, M., Holzapfel, W. L., Hori, Y., Howard, J., Hyland, P., Inoue, Y., Jaehnig, G. C., Jaffe, A., Keating, B., Kermish, Z., Keskitalo, R., Kisner, T., Le Jeune, M., Lee, A. T., Linder, E., Leitch, E. M., Lungu, M., Matsuda, F., Matsumura, T., Meng, X., Miller, N. J., Morii, H., Moyerman, S., Myers, M. J., Navaroli, M., Nishino, H., Paar, H., Peloton, J., Quealy, E., Rebeiz, G., Reichardt, C. L., Richards, P. L., Ross, C., Schanning, I., Schenck, D. E., Sherwin, B., Shimizu, A., Shimmin, C., Shimon, M., Siritanasak, P., Smecher, G., Spieler, H., Stebor, N., Steinbach, B., Stompor, R., Suzuki, A., Takakura, S., Tomaru, T., Wilson, B., Yadav, A., Zahn, O., and Polarbear Collaboration (2014). Measurement of the Cosmic Microwave Background Polarization Lensing Power Spectrum with the POLARBEAR Experiment. *Physical Review Letters*, 113(2):021301.

Ali, Z. S., Parsons, A. R., Zheng, H., Pober, J. C., Liu, A., Aguirre, J. E., Bradley, R. F., Bernardi,

G., Carilli, C. L., Cheng, C., DeBoer, D. R., Dexter, M. R., Grobbelaar, J., Horrell, J., Jacobs, D. C., Klima, P., MacMahon, D. H. E., Maree, M., Moore, D. F., Razavi, N., Stefan, I. I., Walbrugh, W. P., and Walker, A. (2015). PAPER-64 Constraints on Reionization: The 21 cm Power Spectrum at z = 8.4. *Astrophys. J.*, 809:61.

Allison, R., Caucal, P., Calabrese, E., Dunkley, J., and Louis, T. (2015a). Towards a cosmological neutrino mass detection. *Physical Review D.*, 92(12):123535.

Allison, R., Lindsay, S. N., Sherwin, B. D., de Bernardis, F., Bond, J. R., Calabrese, E., Devlin, M. J., Dunkley, J., Gallardo, P., Henderson, S., Hincks, A. D., Hlozek, R., Jarvis, M., Kosowsky, A., Louis, T., Madhavacheril, M., McMahon, J., Moodley, K., Naess, S., Newburgh, L., Niemack, M. D., Page, L. A., Partridge, B., Sehgal, N., Spergel, D. N., Staggs, S. T., van Engelen, A., and Wollack, E. J. (2015b). The Atacama Cosmology Telescope: measuring radio galaxy bias through cross-correlation with lensing. *Mon. Not. R. Astron. Soc.*, 451:849–858.

Alpher, R. A., Bethe, H., and Gamow, G. (1948). The Origin of Chemical Elements. *Physical Review*, 73:803–804.

Amblard, A., Vale, C., and White, M. (2004). Weak lensing of the CMB by large-scale structure. *New Astron.*, 9:687–704.

Bagla, J. S., Khandai, N., and Datta, K. K. (2010). HI as a probe of the large-scale structure in the post-reionization universe. *Mon. Not. R. Astron. Soc.*, 407:567–580.

Bardeen, J. M. (1980). Gauge-invariant cosmological perturbations. *Physical Review D.*, 22:1882–1905.

Barkana, R. and Loeb, A. (2001). In the beginning: the first sources of light and the reionization of the universe. *Phys. Rep.*, 349:125–238.

Bartelmann, M. and Schneider, P. (2001). Weak gravitational lensing. *Physics Reports*, 340:291–472.

Battye, R. A., Brown, M. L., Browne, I. W. A., Davis, R. J., Dewdney, P., Dickinson, C., Heron, G., Maffei, B., Pourtsidou, A., and Wilkinson, P. N. (2012). BINGO: a single dish approach to 21cm intensity mapping. *ArXiv e-prints*.

Baxter, E. J., Keisler, R., Dodelson, S., Aird, K. A., Allen, S. W., Ashby, M. L. N., Bautz, M., Bayliss, M., Benson, B. A., Bleem, L. E., Bocquet, S., Brodwin, M., Carlstrom, J. E., Chang, C. L., Chiu, I., Cho, H.-M., Clocchiatti, A., Crawford, T. M., Crites, A. T., Desai, S., Dietrich, J. P., de Haan, T., Dobbs, M. A., Foley, R. J., Forman, W. R., George, E. M., Gladders, M. D., Gonzalez, A. H., Halverson, N. W., Harrington, N. L., Hennig, C., Hoekstra, H., Holder, G. P., Holzapfel, W. L., Hou, Z., Hrubes, J. D., Jones, C., Knox, L., Lee, A. T., Leitch, E. M., Liu, J., Lueker, M., Luong-Van, D., Mantz, A., Marrone, D. P., McDonald, M., McMahon, J. J., Meyer, S. S., Millea, M., Mocanu, L. M., Murray, S. S., Padin, S., Pryke, C., Reichardt, C. L., Rest, A., Ruhl, J. E., Saliwanchik, B. R., Saro, A., Sayre, J. T., Schaffer, K. K., Shirokoff, E., Song, J., Spieler, H. G., Stalder, B., Stanford, S. A., Staniszewski, Z., Stark, A. A., Story, K. T., van Engelen, A., Vanderlinde, K., Vieira, J. D., Vikhlinin, A., Williamson, R., Zahn, O., and Zenteno, A. (2015). A Measurement of Gravitational Lensing of the Cosmic Microwave Background by Galaxy Clusters Using Data from the South Pole Telescope. *Astrophys. J.*, 806:247.

Beardsley, A. and MWA Collaboration (2015). Epoch of Reionization observations from the first semester of data from the Murchison Widefield Array. In *American Astronomical Society Meeting Abstracts*, volume 225 of *American Astronomical Society Meeting Abstracts*, page 301.04.

Bennett, C. L., Halpern, M., Hinshaw, G., Jarosik, N., Kogut, A., Limon, M., Meyer, S. S., Page, L., Spergel, D. N., Tucker, G. S., Wollack, E., Wright, E. L., Barnes, C., Greason, M. R., Hill, R. S., Komatsu, E., Nolta, M. R., Odegard, N., Peiris, H. V., Verde, L., and Weiland, J. L. (2003). First-Year Wilkinson Microwave Anisotropy Probe (WMAP) Observations: Preliminary Maps and Basic Results. *Astrophys. J. Supp.*, 148:1–27.

Benoit-Lévy, A., Smith, K. M., and Hu, W. (2012). Non-Gaussian structure of the lensed CMB power spectra covariance matrix. *Physical Review D.*, 86(12):123008.

Bernardeau, F. (1997). Weak lensing detection in CMB maps. *Astron. Astrophys.*, 324:15–26.

Bernstein, G. and Jain, B. (2004). Dark Energy Constraints from Weak-Lensing Cross-Correlation Cosmography. *Astrophys. J.*, 600:17–25.

Bharadwaj, S. and Ali, S. S. (2005). On using visibility correlations to probe the HI distribution from the dark ages to the present epoch - I. Formalism and the expected signal. *Mon. Not. R. Astron. Soc.*, 356:1519–1528.

Bharadwaj, S., Nath, B. B., and Sethi, S. K. (2001). Using HI to Probe Large Scale Structures at z ˜ 3. *Journal of Astrophysics and Astronomy*, 22:21.

Bianchini, F., Bielewicz, P., Lapi, A., Gonzalez-Nuevo, J., Baccigalupi, C., de Zotti, G., Danese, L., Bourne, N., Cooray, A., Dunne, L., Dye, S., Eales, S., Ivison, R., Maddox, S., Negrello, M., Scott, D., Smith, M. W. L., and Valiante, E. (2015). Cross-correlation between the CMB Lensing Potential Measured by Planck and High-z Submillimeter Galaxies Detected by the Herschel-Atlas Survey. *Astrophys. J.*, 802:64.

Blake, C. and Glazebrook, K. (2003). Probing Dark Energy Using Baryonic Oscillations in the Galaxy Power Spectrum as a Cosmological Ruler. *Astrophys. J.*, 594:665–673.

Blanchard, A. and Schneider, J. (1987). Gravitational lensing effect on the fluctuations of the cosmic background radiation. *Astron. Astrophys.*, 184:1–6.

Bond, J. R. and Efstathiou, G. (1984). Cosmic background radiation anisotropies in universes dominated by nonbaryonic dark matter. *Astrophys. J. Lett.*, 285:L45–L48.

Booth, R. S. and Jonas, J. L. (2012). An Overview of the MeerKAT Project. *African Skies*, 16:101.

Bromm, V. and Larson, R. B. (2004). The First Stars. *Annu. Rev. Astron. Astrophys.*, 42:79–118.

Bucher, M., Carvalho, C. S., Moodley, K., and Remazeilles, M. (2012). CMB lensing reconstruction in real space. *Physical Review D.*, 85(4):043016.

Bull, P., Ferreira, P. G., Patel, P., and Santos, M. G. (2015). Late-time Cosmology with 21 cm Intensity Mapping Experiments. *Astrophys. J.*, 803:21.

Chang, C., Vikram, V., Jain, B., Bacon, D., Amara, A., Becker, M. R., Bernstein, G., Bonnett, C., Bridle, S., Brout, D., Busha, M., Frieman, J., Gaztanaga, E., Hartley, W., Jarvis, M., Kacprzak, T., Kovács, A., Lahav, O., Lin, H., Melchior, P., Peiris, H., Rozo, E., Rykoff, E., Sánchez, C., Sheldon, E., Troxel, M. A., Wechsler, R., Zuntz, J., Abbott, T., Abdalla, F. B., Allam, S., Annis, J., Bauer, A. H., Benoit-Lévy, A., Brooks, D., Buckley-Geer, E., Burke, D. L., Capozzi, D., Carnero Rosell, A., Carrasco Kind, M., Castander, F. J., Crocce, M., D'Andrea, C. B., Desai, S., Diehl, H. T., Dietrich, J. P., Doel, P., Eifler, T. F., Evrard, A. E., Fausti Neto, A., Flaugher, B., Fosalba, P., Gruen, D., Gruendl, R. A., Gutierrez, G., Honscheid, K., James, D., Kent, S., Kuehn, K., Kuropatkin, N., Maia, M. A. G., March, M., Martini, P., Merritt, K. W., Miller, C. J., Miquel, R., Neilsen, E., Nichol, R. C., Ogando, R., Plazas, A. A., Romer, A. K., Roodman, A., Sako, M., Sanchez, E., Sevilla, I., Smith, R. C., Soares-Santos, M., Sobreira, F., Suchyta, E., Tarle, G., Thaler, J., Thomas, D., Tucker, D., and Walker, A. R. (2015). Wide-Field Lensing Mass Maps from Dark Energy Survey Science Verification Data. *Physical Review Letters*, 115(5):051301.

Chang, T.-C., Pen, U.-L., Bandura, K., and Peterson, J. B. (2010). An intensity map of hydrogen 21-cm emission at redshift z˜0.8. *Nature.*, 466:463–465.

Chang, T.-C., Pen, U.-L., Peterson, J. B., and McDonald, P. (2008). Baryon Acoustic Oscillation Intensity Mapping of Dark Energy. *Physical Review Letters*, 100(9):091303.

Chen, X. (2015). The Tianlai 21cm intensity mapping experiment. *IAU General Assembly*, 22:2252187.

Clowe, D., Bradač, M., Gonzalez, A. H., Markevitch, M., Randall, S. W., Jones, C., and Zaritsky, D. (2006). A Direct Empirical Proof of the Existence of Dark Matter. *Astrophys. J. Lett.*, 648:L109–L113.

Cole, S. and Efstathiou, G. (1989). Gravitational lensing of fluctuations in the microwave background radiation. *Mon. Not. R. Astron. Soc.*, 239:195–200.

Cooray, A. and Kesden, M. (2003). Weak lensing of the CMB: extraction of lensing information from the trispectrum. *New Astron.*, 8:231–253.

Crites, A. T., Henning, J. W., Ade, P. A. R., Aird, K. A., Austermann, J. E., Beall, J. A., Bender, A. N., Benson, B. A., Bleem, L. E., Carlstrom, J. E., Chang, C. L., Chiang, H. C., Cho, H.-M., Citron, R., Crawford, T. M., de Haan, T., Dobbs, M. A., Everett, W., Gallicchio, J., Gao, J., George, E. M., Gilbert, A., Halverson, N. W., Hanson, D., Harrington, N., Hilton, G. C., Holder, G. P., Holzapfel, W. L., Hoover, S., Hou, Z., Hrubes, J. D., Huang, N., Hubmayr, J., Irwin, K. D., Keisler, R., Knox, L., Lee, A. T., Leitch, E. M., Li, D., Liang, C., Luong-Van, D., McMahon, J. J., Mehl, J., Meyer, S. S., Mocanu, L., Montroy, T. E., Natoli, T., Nibarger, J. P., Novosad, V., Padin, S., Pryke, C., Reichardt, C. L., Ruhl, J. E., Saliwanchik, B. R., Sayre, J. T., Schaffer, K. K., Smecher, G., Stark, A. A., Story, K. T., Tucker, C., Vanderlinde, K., Vieira, J. D., Wang, G., Whitehorn, N., Yefremenko, V., and Zahn, O. (2015). Measurements of E-Mode Polarization and Temperature-E-Mode Correlation in the Cosmic Microwave Background from 100 Square Degrees of SPTpol Data. *Astrophys. J.*, 805:36.

Das, S., Louis, T., Nolta, M. R., Addison, G. E., Battistelli, E. S., Bond, J. R., Calabrese, E., Crichton, D., Devlin, M. J., Dicker, S., Dunkley, J., Dünner, R., Fowler, J. W., Gralla, M., Hajian, A., Halpern, M., Hasselfield, M., Hilton, M., Hincks, A. D., Hlozek, R., Huffenberger, K. M., Hughes, J. P., Irwin, K. D., Kosowsky, A., Lupton, R. H., Marriage, T. A., Marsden, D., Menanteau, F., Moodley, K., Niemack, M. D., Page, L. A., Partridge, B., Reese, E. D., Schmitt, B. L., Sehgal, N., Sherwin, B. D., Sievers, J. L., Spergel, D. N., Staggs, S. T., Swetz, D. S., Switzer, E. R., Thornton, R., Trac, H., and Wollack, E. (2014). The Atacama Cosmology

Telescope: temperature and gravitational lensing power spectrum measurements from three seasons of data. *Journal of Cosmology and Astroparticle Physics.*, 4:014.

Das, S., Marriage, T. A., Ade, P. A. R., Aguirre, P., Amiri, M., Appel, J. W., Barrientos, L. F., Battistelli, E. S., Bond, J. R., Brown, B., Burger, B., Chervenak, J., Devlin, M. J., Dicker, S. R., Bertrand Doriese, W., Dunkley, J., Dünner, R., Essinger-Hileman, T., Fisher, R. P., Fowler, J. W., Hajian, A., Halpern, M., Hasselfield, M., Hernández-Monteagudo, C., Hilton, G. C., Hilton, M., Hincks, A. D., Hlozek, R., Huffenberger, K. M., Hughes, D. H., Hughes, J. P., Infante, L., Irwin, K. D., Baptiste Juin, J., Kaul, M., Klein, J., Kosowsky, A., Lau, J. M., Limon, M., Lin, Y.-T., Lupton, R. H., Marsden, D., Martocci, K., Mauskopf, P., Menanteau, F., Moodley, K., Moseley, H., Netterfield, C. B., Niemack, M. D., Nolta, M. R., Page, L. A., Parker, L., Partridge, B., Reid, B., Sehgal, N., Sherwin, B. D., Sievers, J., Spergel, D. N., Staggs, S. T., Swetz, D. S., Switzer, E. R., Thornton, R., Trac, H., Tucker, C., Warne, R., Wollack, E., and Zhao, Y. (2011a). The Atacama Cosmology Telescope: A Measurement of the Cosmic Microwave Background Power Spectrum at 148 and 218 GHz from the 2008 Southern Survey. *Astrophys. J.*, 729:62.

Das, S., Sherwin, B. D., Aguirre, P., Appel, J. W., Bond, J. R., Carvalho, C. S., Devlin, M. J., Dunkley, J., Dünner, R., Essinger-Hileman, T., Fowler, J. W., Hajian, A., Halpern, M., Hasselfield, M., Hincks, A. D., Hlozek, R., Huffenberger, K. M., Hughes, J. P., Irwin, K. D., Klein, J., Kosowsky, A., Lupton, R. H., Marriage, T. A., Marsden, D., Menanteau, F., Moodley, K., Niemack, M. D., Nolta, M. R., Page, L. A., Parker, L., Reese, E. D., Schmitt, B. L., Sehgal, N., Sievers, J., Spergel, D. N., Staggs, S. T., Swetz, D. S., Switzer, E. R., Thornton, R., Visnjic, K., and Wollack, E. (2011b). Detection of the Power Spectrum of Cosmic Microwave Background Lensing by the Atacama Cosmology Telescope. *Physical Review Letters*, 107(2):021301.

Das, S. and Spergel, D. N. (2009). Measuring distance ratios with CMB-galaxy lensing cross-correlations. *Physical Review D.*, 79(4):043509.

Datta, K. K., Choudhury, T. R., and Bharadwaj, S. (2007). The multifrequency angular power spectrum of the epoch of reionization 21-cm signal. *Mon. Not. R. Astron. Soc.*, 378:119–128.

Davé, R., Katz, N., Oppenheimer, B. D., Kollmeier, J. A., and Weinberg, D. H. (2013). The neutral hydrogen content of galaxies in cosmological hydrodynamic simulations. *Mon. Not. R. Astron. Soc.*, 434:2645–2663.

de Putter, R., Zahn, O., and Linder, E. V. (2009). CMB lensing constraints on neutrinos and dark energy. *Physical Review D.*, 79(6):065033.

DeBoer, D. R. and HERA (2015). Hydrogen Epoch of Reionization Array (HERA). In *American Astronomical Society Meeting Abstracts*, volume 225 of *American Astronomical Society Meeting Abstracts*, page 328.03.

Dodelson, S. (2003). *Modern cosmology*. Academic Press.

Dodelson, S. (2004). CMB-cluster lensing. *Physical Review D.*, 70(2):023009.

Dunkley, J., Calabrese, E., Sievers, J., Addison, G. E., Battaglia, N., Battistelli, E. S., Bond, J. R., Das, S., Devlin, M. J., Dünner, R., Fowler, J. W., Gralla, M., Hajian, A., Halpern, M., Hasselfield, M., Hincks, A. D., Hlozek, R., Hughes, J. P., Irwin, K. D., Kosowsky, A., Louis, T., Marriage, T. A., Marsden, D., Menanteau, F., Moodley, K., Niemack, M., Nolta, M. R., Page, L. A., Partridge, B., Sehgal, N., Spergel, D. N., Staggs, S. T., Switzer, E. R., Trac, H., and Wollack, E. (2013). The Atacama Cosmology Telescope: likelihood for small-scale CMB data. *Journal of Cosmology and Astroparticle Physics.*, 7:025.

Dyson, F. W., Eddington, A. S., and Davidson, C. (1920). A Determination of the Deflection of Light by the Sun's Gravitational Field, from Observations Made at the Total Eclipse of May 29, 1919. *Philosophical Transactions of the Royal Society of London Series A*, 220:291–333.

Einstein, A. (1915). Die Feldgleichungen der Gravitation. *Sitzungsberichte der Königlich Preußischen Akademie der Wissenschaften (Berlin), Seite 844-847.*, pages 844–847.

Eisenstein, D. J., Zehavi, I., Hogg, D. W., Scoccimarro, R., Blanton, M. R., Nichol, R. C., Scranton, R., Seo, H.-J., Tegmark, M., Zheng, Z., Anderson, S. F., Annis, J., Bahcall, N., Brinkmann, J., Burles, S., Castander, F. J., Connolly, A., Csabai, I., Doi, M., Fukugita, M.,

Frieman, J. A., Glazebrook, K., Gunn, J. E., Hendry, J. S., Hennessy, G., Ivezić, Z., Kent, S., Knapp, G. R., Lin, H., Loh, Y.-S., Lupton, R. H., Margon, B., McKay, T. A., Meiksin, A., Munn, J. A., Pope, A., Richmond, M. W., Schlegel, D., Schneider, D. P., Shimasaku, K., Stoughton, C., Strauss, M. A., SubbaRao, M., Szalay, A. S., Szapudi, I., Tucker, D. L., Yanny, B., and York, D. G. (2005). Detection of the Baryon Acoustic Peak in the Large-Scale Correlation Function of SDSS Luminous Red Galaxies. *Astrophys. J.*, 633:560–574.

Ewen, H. I. and Purcell, E. M. (1951). Observation of a Line in the Galactic Radio Spectrum: Radiation from Galactic Hydrogen at 1,420 Mc./sec. *Nature.*, 168:356.

Friedmann, A. (1922). Über die Krümmung des Raumes. *Zeitschrift fur Physik*, 10:377–386.

Furlanetto, S. R., Oh, S. P., and Briggs, F. H. (2006). Cosmology at low frequencies: The 21 cm transition and the high-redshift Universe. *Phys. Rep.*, 433:181–301.

Gamow, G. (1948). The Origin of Elements and the Separation of Galaxies. *Physical Review*, 74:505–506.

Guha Sarkar, T. (2010). CMBR weak lensing and HI 21-cm cross-correlation angular power spectrum. *Journal of Cosmology and Astroparticle Physics.*, 2:002.

Guha Sarkar, T., Datta, K. K., and Bharadwaj, S. (2009). The CMBR ISW and HI 21 cm cross-correlation angular power spectrum. *Journal of Cosmology and Astroparticle Physics.*, 8:019.

Guth, A. H. (1981). Inflationary universe: A possible solution to the horizon and flatness problems. *Physical Review D.*, 23:347–356.

Guth, A. H. and Weinberg, E. J. (1983). Could the universe have recovered from a slow first-order phase transition? *Nuclear Physics B*, 212:321–364.

Haiman, Z. and Knox, L. (1999). Reionization of the Intergalactic Medium and its Effect on the CMB. In de Oliveira-Costa, A. and Tegmark, M., editors, *Microwave Foregrounds*, volume 181 of *Astronomical Society of the Pacific Conference Series*, page 227.

Hand, N., Leauthaud, A., Das, S., Sherwin, B. D., Addison, G. E., Bond, J. R., Calabrese, E., Charbonnier, A., Devlin, M. J., Dunkley, J., Erben, T., Hajian, A., Halpern, M., Harnois-Déraps, J., Heymans, C., Hildebrandt, H., Hincks, A. D., Kneib, J.-P., Kosowsky, A., Makler, M., Miller, L., Moodley, K., Moraes, B., Niemack, M. D., Page, L. A., Partridge, B., Sehgal, N., Shan, H., Sievers, J. L., Spergel, D. N., Staggs, S. T., Switzer, E. R., Taylor, J. E., Van Waerbeke, L., Welker, C., and Wollack, E. J. (2015). First measurement of the cross-correlation of CMB lensing and galaxy lensing. *Physical Review D.*, 91(6):062001.

Henderson, S. W., Allison, R., Austermann, J., Baildon, T., Battaglia, N., Beall, J. A., Becker, D., De Bernardis, F., Bond, J. R., Calabrese, E., Choi, S. K., Coughlin, K. P., Crowley, K. T., Datta, R., Devlin, M. J., Duff, S. M., Dunner, R., Dunkley, J., van Engelen, A., Gallardo, P. A., Grace, E., Hasselfield, M., Hills, F., Hilton, G. C., Hincks, A. D., Hlozek, R., Ho, S. P., Hubmayr, J., Huffenberger, K., Hughes, J. P., Irwin, K. D., Koopman, B. J., Kosowsky, A. B., Li, D., McMahon, J., Munson, C., Nati, F., Newburgh, L., Niemack, M. D., Niraula, P., Page, L. A., Pappas, C. G., Salatino, M., Schillaci, A., Schmitt, B. L., Sehgal, N., Sherwin, B. D., Sievers, J. L., Simon, S. M., Spergel, D. N., Staggs, S. T., Stevens, J. R., Thornton, R., Van Lanen, J., Vavagiakis, E. M., Ward, J. T., and Wollack, E. J. (2015). Advanced ACTPol Cryogenic Detector Arrays and Readout. *ArXiv e-prints*.

Hirata, C. M., Ho, S., Padmanabhan, N., Seljak, U., and Bahcall, N. A. (2008). Correlation of CMB with large-scale structure. II. Weak lensing. *Physical Review D.*, 78(4):043520.

Hirata, C. M. and Seljak, U. (2003a). Analyzing weak lensing of the cosmic microwave background using the likelihood function. *Physical Review D.*, 67(4):043001.

Hirata, C. M. and Seljak, U. (2003b). Reconstruction of lensing from the cosmic microwave background polarization. *Physical Review D.*, 68(8):083002.

HIRAX Collaboration (2016). HIRAX: The Hydrogen Intensity and Real-time Analysis eXperiment. `http://www.acru.ukzn.ac.za/~hirax/`. Accessed: 2016-02-02.

Hoekstra, H., Bartelmann, M., Dahle, H., Israel, H., Limousin, M., and Meneghetti, M. (2013). Masses of Galaxy Clusters from Gravitational Lensing. *Space Sci. Rev.*, 177:75–118.

Hogg, D. W. (1999). Distance measures in cosmology. *ArXiv Astrophysics e-prints*.

Holder, G. and Kosowsky, A. (2004). Gravitational Lensing of the Microwave Background by Galaxy Clusters. *Astrophys. J.*, 616:8–15.

Holder, G. P., Viero, M. P., Zahn, O., Aird, K. A., Benson, B. A., Bhattacharya, S., Bleem, L. E., Bock, J., Brodwin, M., Carlstrom, J. E., Chang, C. L., Cho, H.-M., Conley, A., Crawford, T. M., Crites, A. T., de Haan, T., Dobbs, M. A., Dudley, J., George, E. M., Halverson, N. W., Holzapfel, W. L., Hoover, S., Hou, Z., Hrubes, J. D., Keisler, R., Knox, L., Lee, A. T., Leitch, E. M., Lueker, M., Luong-Van, D., Marsden, G., Marrone, D. P., McMahon, J. J., Mehl, J., Meyer, S. S., Millea, M., Mohr, J. J., Montroy, T. E., Padin, S., Plagge, T., Pryke, C., Reichardt, C. L., Ruhl, J. E., Sayre, J. T., Schaffer, K. K., Schulz, B., Shaw, L., Shirokoff, E., Spieler, H. G., Staniszewski, Z., Stark, A. A., Story, K. T., van Engelen, A., Vanderlinde, K., Vieira, J. D., Williamson, R., and Zemcov, M. (2013). A Cosmic Microwave Background Lensing Mass Map and Its Correlation with the Cosmic Infrared Background. *Astrophys. J. Lett.*, 771:L16.

Hu, W. (2001a). Angular trispectrum of the cosmic microwave background. *Physical Review D.*, 64(8):083005.

Hu, W. (2001b). Mapping the Dark Matter through the Cosmic Microwave Background Damping Tail. *Astrophys. J. Lett.*, 557:L79–L83.

Hu, W. (2008). Lecture Notes on CMB Theory: From Nucleosynthesis to Recombination. *ArXiv e-prints*. arxiv.org/abs/0802.3688.

Hu, W. (2013). Intermediate Guide to the Acoustic Peaks and Polarization. http://background.uchicago.edu/ whu/intermediate/intermediate.html.

Hu, W., DeDeo, S., and Vale, C. (2007). Cluster mass estimators from CMB temperature and polarization lensing. *New Journal of Physics*, 9:441.

Hu, W. and Haiman, Z. (2003). Redshifting rings of power. *Physical Review D.*, 68(6):063004.

Hu, W. and Okamoto, T. (2002). Mass Reconstruction with Cosmic Microwave Background Polarization. *Astrophys. J.*, 574:566–574.

Hu, W. and Sugiyama, N. (1995). Anisotropies in the cosmic microwave background: an analytic approach. *Astrophys. J.*, 444:489–506.

Hu, W. and White, M. (1997). A CMB polarization primer. *New Astronomy*, 2:323–344.

Hubble, E. (1929). A Relation between Distance and Radial Velocity among Extra-Galactic Nebulae. *Proceedings of the National Academy of Science*, 15:168–173.

Ivezic, Z., Tyson, J. A., Abel, B., Acosta, E., Allsman, R., AlSayyad, Y., Anderson, S. F., Andrew, J., Angel, R., Angeli, G., Ansari, R., Antilogus, P., Arndt, K. T., Astier, P., Aubourg, E., Axelrod, T., Bard, D. J., Barr, J. D., Barrau, A., Bartlett, J. G., Bauman, B. J., Beaumont, S., Becker, A. C., Becla, J., Beldica, C., Bellavia, S., Blanc, G., Blandford, R. D., Bloom, J. S., Bogart, J., Borne, K., Bosch, J. F., Boutigny, D., Brandt, W. N., Brown, M. E., Bullock, J. S., Burchat, P., Burke, D. L., Cagnoli, G., Calabrese, D., Chandrasekharan, S., Chesley, S., Cheu, E. C., Chiang, J., Claver, C. F., Connolly, A. J., Cook, K. H., Cooray, A., Covey, K. R., Cribbs, C., Cui, W., Cutri, R., Daubard, G., Daues, G., Delgado, F., Digel, S., Doherty, P., Dubois, R., Dubois-Felsmann, G. P., Durech, J., Eracleous, M., Ferguson, H., Frank, J., Freemon, M., Gangler, E., Gawiser, E., Geary, J. C., Gee, P., Geha, M., Gibson, R. R., Gilmore, D. K., Glanzman, T., Goodenow, I., Gressler, W. J., Gris, P., Guyonnet, A., Hascall, P. A., Haupt, J., Hernandez, F., Hogan, C., Huang, D., Huffer, M. E., Innes, W. R., Jacoby, S. H., Jain, B., Jee, J., Jernigan, J. G., Jevremovic, D., Johns, K., Jones, R. L., Juramy-Gilles, C., Juric, M., Kahn, S. M., Kalirai, J. S., Kallivayalil, N., Kalmbach, B., Kantor, J. P., Kasliwal, M. M., Kessler, R., Kirkby, D., Knox, L., Kotov, I., Krabbendam, V. L., Krughoff, S., Kubanek, P., Kuczewski, J., Kulkarni, S., Lambert, R., Le Guillou, L., Levine, D., Liang, M., Lim, K., Lintott, C., Lupton, R. H., Mahabal, A., Marshall, P., Marshall, S., May, M., McKercher, R., Migliore, M., Miller, M., Mills, D. J., Monet, D. G., Moniez, M., Neill, D. R., Nief, J., Nomerotski, A., Nordby, M.,

O'Connor, P., Oliver, J., Olivier, S. S., Olsen, K., Ortiz, S., Owen, R. E., Pain, R., Peterson, J. R., Petry, C. E., Pierfederici, F., Pietrowicz, S., Pike, R., Pinto, P. A., Plante, R., Plate, S., Price, P. A., Prouza, M., Radeka, V., Rajagopal, J., Rasmussen, A., Regnault, N., Ridgway, S. T., Ritz, S., Rosing, W., Roucelle, C., Rumore, M. R., Russo, S., Saha, A., Sassolas, B., Schalk, T. L., Schindler, R. H., Schneider, D. P., Schumacher, G., Sebag, J., Sembroski, G. H., Seppala, L. G., Shipsey, I., Silvestri, N., Smith, J. A., Smith, R. C., Strauss, M. A., Stubbs, C. W., Sweeney, D., Szalay, A., Takacs, P., Thaler, J. J., Van Berg, R., Vanden Berk, D., Vetter, K., Virieux, F., Xin, B., Walkowicz, L., Walter, C. W., Wang, D. L., Warner, M., Willman, B., Wittman, D., Wolff, S. C., Wood-Vasey, W. M., Yoachim, P., Zhan, H., and for the LSST Collaboration (2008). LSST: from Science Drivers to Reference Design and Anticipated Data Products. *ArXiv e-prints*.

Jain, B. and Taylor, A. (2003). Cross-Correlation Tomography: Measuring Dark Energy Evolution with Weak Lensing. *Physical Review Letters*, 91(14):141302.

Jauzac, M., Richard, J., Jullo, E., Clément, B., Limousin, M., Kneib, J.-P., Ebeling, H., Natarajan, P., Rodney, S., Atek, H., Massey, R., Eckert, D., Egami, E., and Rexroth, M. (2015). Hubble Frontier Fields: a high-precision strong-lensing analysis of the massive galaxy cluster Abell 2744 using 180 multiple images. *Mon. Not. R. Astron. Soc.*, 452:1437–1446.

Jullo, E., Natarajan, P., Kneib, J.-P., D'Aloisio, A., Limousin, M., Richard, J., and Schimd, C. (2010). Cosmological Constraints from Strong Gravitational Lensing in Clusters of Galaxies. *Science*, 329:924–927.

Kaiser, N. (1987). Clustering in real space and in redshift space. *Mon. Not. R. Astron. Soc.*, 227:1–21.

Kesden, M., Cooray, A., and Kamionkowski, M. (2003). Lensing reconstruction with CMB temperature and polarization. *Physical Review D.*, 67(12):123507.

Kneib, J.-P. and Natarajan, P. (2011). Cluster lenses. *Astron. Astrophys. Rev.*, 19:47.

Koopmans, L., Pritchard, J., Mellema, G., Aguirre, J., Ahn, K., Barkana, R., van Bemmel, I., Bernardi, G., Bonaldi, A., Briggs, F., de Bruyn, A. G., Chang, T. C., Chapman, E., Chen, X., Ciardi, B., Dayal, P., Ferrara, A., Fialkov, A., Fiore, F., Ichiki, K., Illiev, I. T., Inoue, S., Jelic, V., Jones, M., Lazio, J., Maio, U., Majumdar, S., Mack, K. J., Mesinger, A., Morales, M. F., Parsons, A., Pen, U. L., Santos, M., Schneider, R., Semelin, B., de Souza, R. S., Subrahmanyan, R., Takeuchi, T., Vedantham, H., Wagg, J., Webster, R., Wyithe, S., Datta, K. K., and Trott, C. (2015). The Cosmic Dawn and Epoch of Reionisation with SKA. *Advancing Astrophysics with the Square Kilometre Array (AASKA14)*, page 1.

Kuntz, A. (2015). Cross-correlation of CFHTLenS galaxy catalogue and Planck CMB lensing using the halo model prescription. *Astron. Astrophys.*, 584:A53.

Kurki-Suonio, H. (2011). Introduction to cosmological perturbation theory. http://theory.physics.helsinki.fi/ genrel/CosPerShort.pdf.

Laureijs, R., Amiaux, J., Arduini, S., Augueres, J. ., Brinchmann, J., Cole, R., Cropper, M., Dabin, C., Duvet, L., Ealet, A., and et al. (2011). Euclid Definition Study Report. *ArXiv e-prints*.

Lemaître, G. (1927). Un Univers homogène de masse constante et de rayon croissant rendant compte de la vitesse radiale des nébuleuses extra-galactiques. *Annales de la Société Scientifique de Bruxelles*, 47:49–59.

Lesgourgues, J., Perotto, L., Pastor, S., and Piat, M. (2006). Probing neutrino masses with CMB lensing extraction. *Physical Review D.*, 73(4):045021.

Lewis, A. and Challinor, A. (2006). Weak gravitational lensing of the CMB. *Physics Reports*, 429:1–65.

Lewis, A. and Challinor, A. (2011). CAMB: Code for Anisotropies in the Microwave Background. Astrophysics Source Code Library.

Liddle, A. (2003). *An Introduction to Modern Cosmology*. John Wiley and Sons, Chichester.

Liddle, A. and Lyth, D. (2000). *Cosmological Inflation and Large-Scale Structure*. Cambridge University Press, Cambridge.

Limber, D. N. (1953). The Analysis of Counts of the Extragalactic Nebulae in Terms of a Fluctuating Density Field. *Astrophys. J.*, 117:134.

Limousin, M., Richard, J., Jullo, E., Jauzac, M., Ebeling, H., Bonamigo, M., Alavi, A., Clement, B., Giocoli, C., Kneib, J. P., Verdugo, T., Natarajan, P., and Siana, B. (2015). Strong-Lensing Analysis of MACS,J0717.5+3745 from Hubble Frontier Fields observations: How well can the mass distribution be constrained? *ArXiv e-prints*.

Linder, E. V. (1990). Analysis of gravitationally lensed microwave background anisotropies. *Mon. Not. R. Astron. Soc.*, 243:353–361.

Liu, A., Tegmark, M., Bowman, J., Hewitt, J., and Zaldarriaga, M. (2009). An improved method for 21-cm foreground removal. *Mon. Not. R. Astron. Soc.*, 398:401–406.

Liu, J. and Hill, J. C. (2015). Cross-correlation of Planck CMB lensing and CFHTLenS galaxy weak lensing maps. *Physical Review D.*, 92(6):063517.

Loeb, A. and Wyithe, J. S. B. (2008). Possibility of Precise Measurement of the Cosmological Power Spectrum with a Dedicated Survey of 21cm Emission after Reionization. *Physical Review Letters*, 100(16):161301.

Loverde, M. and Afshordi, N. (2008). Extended Limber approximation. *Physical Review D.*, 78(12):123506.

Ma, C.-P. and Bertschinger, E. (1995). Cosmological Perturbation Theory in the Synchronous and Conformal Newtonian Gauges. *Astrophys. J.*, 455:7.

Maartens, R., Abdalla, F. B., Jarvis, M., Santos, M. G., and SKA Cosmology SWG, f. t. (2015). Cosmology with the SKA – overview. *ArXiv e-prints*.

Martin, A. M., Giovanelli, R., Haynes, M. P., and Guzzo, L. (2012). The Clustering Characteristics of H I-selected Galaxies from the 40% ALFALFA Survey. *Astrophys. J.*, 750:38.

Massey, R. (2010). Digging into Dark Matter with Weak Gravitational Lensing. In Kieda, D. B. and Gondolo, P., editors, *2009 Snowbird Particle Astrophysics and Cosmology Workshop (SNOWPAC 2009)*, volume 426 of *Astronomical Society of the Pacific Conference Series*, page 115.

Masui, K. W., Switzer, E. R., Banavar, N., Bandura, K., Blake, C., Calin, L.-M., Chang, T.-C., Chen, X., Li, Y.-C., Liao, Y.-W., Natarajan, A., Pen, U.-L., Peterson, J. B., Shaw, J. R., and Voytek, T. C. (2013). Measurement of 21 cm Brightness Fluctuations at z ˜ 0.8 in Cross-correlation. *Astrophys. J. Lett.*, 763:L20.

Mather, J. C., Hauser, M. G., Bennett, C. L., Boggess, N. W., Cheng, E. S., Eplee, Jr., R. E., Freudenreich, H. T., Isaacman, R. B., Kelsall, T., Lisse, C. M., Moseley, Jr., S. H., Shafer, R. A., Silverberg, R. F., Spiesman, W. J., Toller, G. N., Weiland, J. L., Gulkis, S., Jansssen, M., Lubin, P. M., Meyer, S. S., Weiss, R., Murdock, T. L., Smoot, G. F., Wilkinson, D. T., and Wright, E. L. (1992). Early results from the Cosmic Background Explorer (COBE). In Haubold, H. J. and Khanna, R. K., editors, *American Institute of Physics Conference Series*, volume 245 of *American Institute of Physics Conference Series*, pages 266–278.

McKee, C. F. and Ostriker, E. C. (2007). Theory of Star Formation. *Annu. Rev. Astron. Astrophys.*, 45:565–687.

McQuinn, M., Zahn, O., Zaldarriaga, M., Hernquist, L., and Furlanetto, S. R. (2006). Cosmological Parameter Estimation Using 21 cm Radiation from the Epoch of Reionization. *Astrophys. J.*, 653:815–834.

Misner, C. W. (1969). Mixmaster Universe. *Physical Review Letters*, 22:1071–1074.

Naess, S., Hasselfield, M., McMahon, J., Niemack, M. D., Addison, G. E., Ade, P. A. R., Allison, R., Amiri, M., Battaglia, N., Beall, J. A., de Bernardis, F., Bond, J. R., Britton, J., Calabrese, E., Cho, H.-m., Coughlin, K., Crichton, D., Das, S., Datta, R., Devlin, M. J., Dicker, S. R., Dunkley, J., Dünner, R., Fowler, J. W., Fox, A. E., Gallardo, P., Grace, E., Gralla, M., Hajian, A., Halpern, M., Henderson, S., Hill, J. C., Hilton, G. C., Hilton, M., Hincks, A. D., Hlozek,

R., Ho, P., Hubmayr, J., Huffenberger, K. M., Hughes, J. P., Infante, L., Irwin, K., Jackson, R., Muya Kasanda, S., Klein, J., Koopman, B., Kosowsky, A., Li, D., Louis, T., Lungu, M., Madhavacheril, M., Marriage, T. A., Maurin, L., Menanteau, F., Moodley, K., Munson, C., Newburgh, L., Nibarger, J., Nolta, M. R., Page, L. A., Pappas, C., Partridge, B., Rojas, F., Schmitt, B. L., Sehgal, N., Sherwin, B. D., Sievers, J., Simon, S., Spergel, D. N., Staggs, S. T., Switzer, E. R., Thornton, R., Trac, H., Tucker, C., Uehara, M., Van Engelen, A., Ward, J. T., and Wollack, E. J. (2014). The Atacama Cosmology Telescope: CMB polarization at $200 < l < 9000$. *Journal of Cosmology and Astroparticle Physics.*, 10:7.

Okamoto, T. and Hu, W. (2003). Cosmic microwave background lensing reconstruction on the full sky. *Physical Review D.*, 67(8):083002.

Ostriker, J. P. and Peebles, P. J. E. (1973). A Numerical Study of the Stability of Flattened Galaxies: or, can Cold Galaxies Survive? *Astrophys. J.*, 186:467–480.

Padmanabhan, H., Choudhury, T. R., and Refregier, A. (2015a). Modelling the cosmic neutral hydrogen from DLAs and 21 cm observations. *ArXiv e-prints*.

Padmanabhan, H., Choudhury, T. R., and Refregier, A. (2015b). Theoretical and observational constraints on the H I intensity power spectrum. *Mon. Not. R. Astron. Soc.*, 447:3745–3755.

Padmanabhan, T. (1993). *Structure Formation in the Universe*. Cambridge University Press.

Pearson, R. and Zahn, O. (2014). Cosmology from cross correlation of CMB lensing and galaxy surveys. *Physical Review D.*, 89(4):043516.

Peebles, P. J. E. (1968). Recombination of the Primeval Plasma. *Astrophys. J.*, 153:1.

Peebles, P. J. E. (1982). Large-scale background temperature and mass fluctuations due to scale-invariant primeval perturbations. *Astrophys. J. Lett.*, 263:L1–L5.

Peebles, P. J. E. and Yu, J. T. (1970). Primeval Adiabatic Perturbation in an Expanding Universe. *Astrophys. J.*, 162:815.

Perlmutter, S., Aldering, G., Goldhaber, G., Knop, R. A., Nugent, P., Castro, P. G., Deustua, S., Fabbro, S., Goobar, A., Groom, D. E., Hook, I. M., Kim, A. G., Kim, M. Y., Lee, J. C., Nunes, N. J., Pain, R., Pennypacker, C. R., Quimby, R., Lidman, C., Ellis, R. S., Irwin, M., McMahon, R. G., Ruiz-Lapuente, P., Walton, N., Schaefer, B., Boyle, B. J., Filippenko, A. V., Matheson, T., Fruchter, A. S., Panagia, N., Newberg, H. J. M., Couch, W. J., and Project, T. S. C. (1999). Measurements of $\Omega$ and $\Lambda$ from 42 High-Redshift Supernovae. *Astrophys. J.*, 517:565–586.

Péroux, C., McMahon, R. G., Storrie-Lombardi, L. J., and Irwin, M. J. (2003). The evolution of $\Omega_{HI}$ and the epoch of formation of damped Lyman $\alpha$ absorbers. *Mon. Not. R. Astron. Soc.*, 346:1103–1115.

Planck Collaboration, Adam, R., Ade, P. A. R., Aghanim, N., Alves, M. I. R., Arnaud, M., Ashdown, M., Aumont, J., Baccigalupi, C., Banday, A. J., and et al. (2015a). Planck 2015 results. X. Diffuse component separation: Foreground maps. *ArXiv e-prints*.

Planck Collaboration, Adam, R., Ade, P. A. R., Aghanim, N., Arnaud, M., Ashdown, M., Aumont, J., Baccigalupi, C., Banday, A. J., Barreiro, R. B., and et al. (2015b). Planck 2015 results. VIII. High Frequency Instrument data processing: Calibration and maps. *ArXiv e-prints*.

Planck Collaboration, Ade, P. A. R., Aghanim, N., Armitage-Caplan, C., Arnaud, M., Ashdown, M., Atrio-Barandela, F., Aumont, J., Baccigalupi, C., Banday, A. J., and et al. (2013). Planck 2013 results. XVI. Cosmological parameters. *Astron. Astrophys.*, 571:A16.

Planck Collaboration, Ade, P. A. R., Aghanim, N., Arnaud, M., Ashdown, M., Aumont, J., Baccigalupi, C., Banday, A. J., Barreiro, R. B., Bartlett, J. G., and et al. (2015c). Planck 2015 results. XIII. Cosmological parameters. *ArXiv e-prints*.

Planck Collaboration, Ade, P. A. R., Aghanim, N., Arnaud, M., Ashdown, M., Aumont, J., Baccigalupi, C., Banday, A. J., Barreiro, R. B., Bartlett, J. G., and et al. (2015d). Planck 2015 results. XV. Gravitational lensing. *ArXiv e-prints*.

Planck Collaboration, Ade, P. A. R., Aghanim, N., Arnaud, M., Ashdown, M., Aumont, J., Baccigalupi, C., Banday, A. J., Barreiro, R. B., Bartolo, N., and et al. (2015e). Planck 2015 results. XIV. Dark energy and modified gravity. *ArXiv e-prints*.

Planck Collaboration, Aghanim, N., Arnaud, M., Ashdown, M., Aumont, J., Baccigalupi, C., Banday, A. J., Barreiro, R. B., Bartlett, J. G., Bartolo, N., and et al. (2015f). Planck 2015 results. XI. CMB power spectra, likelihoods, and robustness of parameters. *ArXiv e-prints*.

Pourtsidou, A., Bacon, D., and Crittenden, R. (2015a). Cross-correlation cosmography with HI intensity mapping. *ArXiv e-prints*.

Pourtsidou, A., Bacon, D., Crittenden, R., and Metcalf, R. B. (2015b). Prospects for clustering and lensing measurements with forthcoming intensity mapping and optical surveys. *ArXiv e-prints*.

Prince, H., Moodley, K., Ridl, J., and Bucher, M. (2016a). Real space lensing reconstruction using cosmic microwave background polarization. in preparation.

Prince, H., Pénin, A., and Moodley, K. (2016b). Cross-correlation of CMB lensing with post-reionization HI intensity mapping surveys. in preparation.

Rees, M. J. and Sciama, D. W. (1968). Large-scale Density Inhomogeneities in the Universe. *Nature.*, 217:511–516.

Reid, B. A., Percival, W. J., Eisenstein, D. J., Verde, L., Spergel, D. N., Skibba, R. A., Bahcall, N. A., Budavari, T., Frieman, J. A., Fukugita, M., Gott, J. R., Gunn, J. E., Ivezić, Ž., Knapp, G. R., Kron, R. G., Lupton, R. H., McKay, T. A., Meiksin, A., Nichol, R. C., Pope, A. C., Schlegel, D. J., Schneider, D. P., Stoughton, C., Strauss, M. A., Szalay, A. S., Tegmark, M., Vogeley, M. S., Weinberg, D. H., York, D. G., and Zehavi, I. (2010). Cosmological constraints from the clustering of the Sloan Digital Sky Survey DR7 luminous red galaxies. *Mon. Not. R. Astron. Soc.*, 404:60–85.

Richard, J., Jauzac, M., Limousin, M., Jullo, E., Clément, B., Ebeling, H., Kneib, J.-P., Atek, H., Natarajan, P., Egami, E., Livermore, R., and Bower, R. (2014). Mass and magnification

maps for the Hubble Space Telescope Frontier Fields clusters: implications for high-redshift studies. *Mon. Not. R. Astron. Soc.*, 444:268–289.

Richard, J., Kneib, J.-P., Ebeling, H., Stark, D. P., Egami, E., and Fiedler, A. K. (2011). Discovery of a possibly old galaxy at z= 6.027, multiply imaged by the massive cluster Abell 383. *Mon. Not. R. Astron. Soc.*, 414:L31–L35.

Ridl, J. (2012). Weak gravitational lensing in the cosmic microwave background: Reconstructing the lensing convergence. Master's thesis, University of KwaZulu Natal.

Riess, A. G., Filippenko, A. V., Challis, P., Clocchiatti, A., Diercks, A., Garnavich, P. M., Gilliland, R. L., Hogan, C. J., Jha, S., Kirshner, R. P., Leibundgut, B., Phillips, M. M., Reiss, D., Schmidt, B. P., Schommer, R. A., Smith, R. C., Spyromilio, J., Stubbs, C., Suntzeff, N. B., and Tonry, J. (1998). Observational Evidence from Supernovae for an Accelerating Universe and a Cosmological Constant. *Astron. J.*, 116:1009–1038.

Riess, A. G., Strolger, L.-G., Casertano, S., Ferguson, H. C., Mobasher, B., Gold, B., Challis, P. J., Filippenko, A. V., Jha, S., Li, W., Tonry, J., Foley, R., Kirshner, R. P., Dickinson, M., MacDonald, E., Eisenstein, D., Livio, M., Younger, J., Xu, C., Dahlén, T., and Stern, D. (2007). New Hubble Space Telescope Discoveries of Type Ia Supernovae at z >= 1: Narrowing Constraints on the Early Behavior of Dark Energy. *Astrophys. J.*, 659:98–121.

Robertson, H. P. (1935). Kinematics and World-Structure. *Astrophys. J.*, 82:284.

Rozo, E., Wechsler, R. H., Rykoff, E. S., Annis, J. T., Becker, M. R., Evrard, A. E., Frieman, J. A., Hansen, S. M., Hao, J., Johnston, D. E., Koester, B. P., McKay, T. A., Sheldon, E. S., and Weinberg, D. H. (2010). Cosmological Constraints from the Sloan Digital Sky Survey maxBCG Cluster Catalog. *Astrophys. J.*, 708:645–660.

Rubin, V. C. and Ford, Jr., W. K. (1970). Rotation of the Andromeda Nebula from a Spectroscopic Survey of Emission Regions. *Astrophys. J.*, 159:379.

Santos, M. G., Bull, P., Alonso, D., Camera, S., Ferreira, P. G., Bernardi, G., Maartens, R., Viel, M., Villaescusa-Navarro, F., Abdalla, F. B., Jarvis, M., Metcalf, R. B., Pourtsidou, A., and Wolz, L. (2015). Cosmology with a SKA HI intensity mapping survey. *ArXiv e-prints*.

Santos, M. G., Cooray, A., and Knox, L. (2005). Multifrequency Analysis of 21 Centimeter Fluctuations from the Era of Reionization. *Astrophys. J.*, 625:575–587.

Seljak, U. (1996). Gravitational Lensing Effect on Cosmic Microwave Background Anisotropies: A Power Spectrum Approach. *Astrophys. J.*, 463:1.

Seljak, U. and Zaldarriaga, M. (1999). Measuring Dark Matter Power Spectrum from Cosmic Microwave Background. *Physical Review Letters*, 82:2636–2639.

Seljak, U. and Zaldarriaga, M. (2000). Lensing-induced Cluster Signatures in the Cosmic Microwave Background. *Astrophys. J.*, 538:57–64.

Seo, H.-J. and Eisenstein, D. J. (2003). Probing Dark Energy with Baryonic Acoustic Oscillations from Future Large Galaxy Redshift Surveys. *Astrophys. J.*, 598:720–740.

Shaw, J. R., Sigurdson, K., Sitwell, M., Stebbins, A., and Pen, U.-L. (2015). Coaxing cosmic 21 cm fluctuations from the polarized sky using m -mode analysis. *Physical Review D.*, 91(8):083514.

Sherwin, B. D., Das, S., Hajian, A., Addison, G., Bond, J. R., Crichton, D., Devlin, M. J., Dunkley, J., Gralla, M. B., Halpern, M., Hill, J. C., Hincks, A. D., Hughes, J. P., Huffenberger, K., Hlozek, R., Kosowsky, A., Louis, T., Marriage, T. A., Marsden, D., Menanteau, F., Moodley, K., Niemack, M. D., Page, L. A., Reese, E. D., Sehgal, N., Sievers, J., Sifón, C., Spergel, D. N., Staggs, S. T., Switzer, E. R., and Wollack, E. (2012). The Atacama Cosmology Telescope: Cross-correlation of cosmic microwave background lensing and quasars. *Physical Review D.*, 86(8):083006.

Sherwin, B. D., Dunkley, J., Das, S., Appel, J. W., Bond, J. R., Carvalho, C. S., Devlin, M. J., Dünner, R., Essinger-Hileman, T., Fowler, J. W., Hajian, A., Halpern, M., Hasselfield, M.,

Hincks, A. D., Hlozek, R., Hughes, J. P., Irwin, K. D., Klein, J., Kosowsky, A., Marriage, T. A., Marsden, D., Moodley, K., Menanteau, F., Niemack, M. D., Nolta, M. R., Page, L. A., Parker, L., Reese, E. D., Schmitt, B. L., Sehgal, N., Sievers, J., Spergel, D. N., Staggs, S. T., Swetz, D. S., Switzer, E. R., Thornton, R., Visnjic, K., and Wollack, E. (2011). Evidence for Dark Energy from the Cosmic Microwave Background Alone Using the Atacama Cosmology Telescope Lensing Measurements. *Physical Review Letters*, 107(2):021302.

Silk, J. (1968). Cosmic Black-Body Radiation and Galaxy Formation. *Astrophys. J.*, 151:459.

Smith, K. M., Zahn, O., and Doré, O. (2007). Detection of gravitational lensing in the cosmic microwave background. *Physical Review D.*, 76(4):043510.

Smoot, G. F., Bennett, C. L., Kogut, A., Wright, E. L., Aymon, J., Boggess, N. W., Cheng, E. S., de Amici, G., Gulkis, S., Hauser, M. G., Hinshaw, G., Jackson, P. D., Janssen, M., Kaita, E., Kelsall, T., Keegstra, P., Lineweaver, C., Loewenstein, K., Lubin, P., Mather, J., Meyer, S. S., Moseley, S. H., Murdock, T., Rokke, L., Silverberg, R. F., Tenorio, L., Weiss, R., and Wilkinson, D. T. (1992). Structure in the COBE differential microwave radiometer first-year maps. *Astrophys. J. Lett.*, 396:L1–L5.

Spergel, D. N., Verde, L., Peiris, H. V., Komatsu, E., Nolta, M. R., Bennett, C. L., Halpern, M., Hinshaw, G., Jarosik, N., Kogut, A., Limon, M., Meyer, S. S., Page, L., Tucker, G. S., Weiland, J. L., Wollack, E., and Wright, E. L. (2003). First-Year Wilkinson Microwave Anisotropy Probe (WMAP) Observations: Determination of Cosmological Parameters. *Astrophys. J. Supp.*, 148:175–194.

Stompor, R. and Efstathiou, G. (1999). Gravitational lensing of cosmic microwave background anisotropies and cosmological parameter estimation. *Mon. Not. R. Astron. Soc.*, 302:735–747.

Sunyaev, R. A. and Zeldovich, Y. B. (1970). Small-Scale Fluctuations of Relic Radiation. *Astrophys. Space Sci.*, 7:3–19.

Sunyaev, R. A. and Zeldovich, Y. B. (1972). The Observations of Relic Radiation as a Test of

the Nature of X-Ray Radiation from the Clusters of Galaxies. *Comments on Astrophysics and Space Physics*, 4:173.

Sunyaev, R. A. and Zeldovich, Y. B. (1975). The velocity of clusters of galaxies relative to the microwave background. The possibility of its measurement. *NASA STI/Recon Technical Report N*, 80.

Switzer, E. R., Masui, K. W., Bandura, K., Calin, L.-M., Chang, T.-C., Chen, X.-L., Li, Y.-C., Liao, Y.-W., Natarajan, A., Pen, U.-L., Peterson, J. B., Shaw, J. R., and Voytek, T. C. (2013). Determination of z = 0.8 neutral hydrogen fluctuations using the 21 cm intensity mapping autocorrelation. *Mon. Not. R. Astron. Soc.*, 434:L46–L50.

Thompson, A. R., Moran, J. M., and Swenson, G. W. (1986). *Interferometry and synthesis in radio astronomy*. Wiley.

Valageas, P., Clerc, N., Pacaud, F., and Pierre, M. (2011). Covariance matrices for halo number counts and correlation functions. *Astron. Astrophys.*, 536:A95.

van Engelen, A., Keisler, R., Zahn, O., Aird, K. A., Benson, B. A., Bleem, L. E., Carlstrom, J. E., Chang, C. L., Cho, H. M., Crawford, T. M., Crites, A. T., de Haan, T., Dobbs, M. A., Dudley, J., George, E. M., Halverson, N. W., Holder, G. P., Holzapfel, W. L., Hoover, S., Hou, Z., Hrubes, J. D., Joy, M., Knox, L., Lee, A. T., Leitch, E. M., Lueker, M., Luong-Van, D., McMahon, J. J., Mehl, J., Meyer, S. S., Millea, M., Mohr, J. J., Montroy, T. E., Natoli, T., Padin, S., Plagge, T., Pryke, C., Reichardt, C. L., Ruhl, J. E., Sayre, J. T., Schaffer, K. K., Shaw, L., Shirokoff, E., Spieler, H. G., Staniszewski, Z., Stark, A. A., Story, K., Vanderlinde, K., Vieira, J. D., and Williamson, R. (2012). A Measurement of Gravitational Lensing of the Microwave Background Using South Pole Telescope Data. *Astrophys. J.*, 756:142.

van Engelen, A., Sherwin, B. D., Sehgal, N., Addison, G. E., Allison, R., Battaglia, N., de Bernardis, F., Bond, J. R., Calabrese, E., Coughlin, K., Crichton, D., Datta, R., Devlin, M. J., Dunkley, J., Dünner, R., Gallardo, P., Grace, E., Gralla, M., Hajian, A., Hasselfield, M., Henderson, S., Hill, J. C., Hilton, M., Hincks, A. D., Hlozek, R., Huffenberger, K. M., Hughes,

J. P., Koopman, B., Kosowsky, A., Louis, T., Lungu, M., Madhavacheril, M., Maurin, L., McMahon, J., Moodley, K., Munson, C., Naess, S., Nati, F., Newburgh, L., Niemack, M. D., Nolta, M. R., Page, L. A., Pappas, C., Partridge, B., Schmitt, B. L., Sievers, J. L., Simon, S., Spergel, D. N., Staggs, S. T., Switzer, E. R., Ward, J. T., and Wollack, E. J. (2015). The Atacama Cosmology Telescope: Lensing of CMB Temperature and Polarization Derived from Cosmic Infrared Background Cross-correlation. *Astrophys. J.*, 808:7.

Vanderlinde, K. and Chime Collaboration (2014). The Canadian Hydrogen Intensity Mapping Experiment (CHIME). In *Exascale Radio Astronomy*, page 10102.

Villaescusa-Navarro, F., Viel, M., Alonso, D., Datta, K. K., Bull, P., and Santos, M. G. (2015). Cross-correlating 21cm intensity maps with Lyman Break Galaxies in the post-reionization era. *Journal of Cosmology and Astroparticle Physics.*, 3:034.

von Soldner, J. (1804). Ueber die Ablenkung eines Lichtstrals von seiner geradlinigen Bewegung (On the Deflection of a Light Ray from its Rectilinear Motion). *'Berliner Astronomisches Jahrbuch'*, 1:161–172.

Walsh, D., Carswell, R. F., and Weymann, R. J. (1979). 0957 + 561 A, B - Twin quasistellar objects or gravitational lens. *Nature.*, 279:381–384.

Wang, X., Tegmark, M., Santos, M. G., and Knox, L. (2006). 21 cm Tomography with Foregrounds. *Astrophys. J.*, 650:529–537.

Weinberg, D. H., Mortonson, M. J., Eisenstein, D. J., Hirata, C., Riess, A. G., and Rozo, E. (2013). Observational probes of cosmic acceleration. *Phys. Rep.*, 530:87–255.

Wilman, R. J., Miller, L., Jarvis, M. J., Mauch, T., Levrier, F., Abdalla, F. B., Rawlings, S., Klöckner, H.-R., Obreschkow, D., Olteanu, D., and Young, S. (2008). A semi-empirical simulation of the extragalactic radio continuum sky for next generation radio telescopes. *Mon. Not. R. Astron. Soc.*, 388:1335–1348.

Wu, K. K. S., Lahav, O., and Rees, M. J. (1999). The large-scale smoothness of the Universe. *Nature.*, 397:225–230.

Wyithe, J. S. B. and Loeb, A. (2008). Fluctuations in 21-cm emission after reionization. *Mon. Not. R. Astron. Soc.*, 383:606–614.

Zafar, T., Péroux, C., Popping, A., Milliard, B., Deharveng, J.-M., and Frank, S. (2013). The ESO UVES advanced data products quasar sample. II. Cosmological evolution of the neutral gas mass density. *Astron. Astrophys.*, 556:A141.

Zaldarriaga, M. (2000). Lensing of the CMB: Non-Gaussian aspects. *Physical Review D.*, 62(6):063510.

Zaldarriaga, M., Furlanetto, S. R., and Hernquist, L. (2004). 21 Centimeter Fluctuations from Cosmic Gas at High Redshifts. *Astrophys. J.*, 608:622–635.

Zaldarriaga, M. and Seljak, U. (1999). Reconstructing projected matter density power spectrum from cosmic microwave background. *Physical Review D.*, 59(12):123507.

Zeldovich, Y. B., Kurt, V. G., and Syunyaev, R. A. (1968). Recombination of Hydrogen in the Hot Model of the Universe. *Zhurnal Eksperimentalnoi i Teoreticheskoi Fiziki*, 55:278–286.

Zhang, J., Hui, L., and Stebbins, A. (2005). Isolating Geometry in Weak-Lensing Measurements. *Astrophys. J.*, 635:806–820.

Zhu, H.-M., Pen, U.-L., Yu, Y., Er, X., and Chen, X. (2015). Cosmic Tidal Reconstruction. *ArXiv e-prints*.

Zinnecker, H. and Yorke, H. W. (2007). Toward Understanding Massive Star Formation. *Annu. Rev. Astron. Astrophys.*, 45:481–563.

Zwicky, F. (1933). Die Rotverschiebung von extragalaktischen Nebeln. *Helvetica Physica Acta*, 6:110–127.

Zwicky, F. (1937). On the Masses of Nebulae and of Clusters of Nebulae. *Astrophys. J.*, 86:217.